Chapter 2
Advance Techniques for the Synthesis of Nanostructured Zirconia-Based Ceramics for Thermal Barrier Application

Reza Shoja Razavi and Mohammad Reza Loghman-Estarki

Abstract The aim of this chapter is the review of various synthesis methods for the preparation of zirconia-based nanostructure for thermal barrier coatings (TBCs) application. To this end, the main materials used in TBCs, including metal oxide (M) stabilized zirconia (M = MgO, CaO, Y_2O_3, CeO_2, Sc_2O_3), codoped-zirconia, rare earth-doped zirconiate (REZ) and zirconia–alumina nanocomposite, were reviewed and easy scales up route for the synthesis of them were studied.

2.1 Introduction

Zirconia (ZrO_2) as an oxide material is hard (Vickers hardness 13–24 GPa), tough (fracture toughness 8–13 MPa m ½, strong (compressive strength 1000–1800 MPa), thermally stable (m.p. 2680 °C), and chemically inert. Zirconia attracts attention due to its application as an engineering ceramic for mechanical, thermal, and electrical purposes.

To use zirconia to in thermal barrier application, stabilizing oxides (particularly MgO, CaO, CeO_2, Sc_2O_3, Al_2O_3, and Y_2O_3) are added in varying amounts to significantly modify its properties. When these stabilizers added in sufficient amounts, these oxides form a fully stabilized zirconia (FSZ) or partially stabilized zirconia (PSZ) that exhibit a cubic (FSZ) or tetragonal (PSZ) structure at room temperature, respectively. The PSZ powder (in form of flowable granules) was usually used in thermal barrier application. TBCs have been employed to protect the metallic components (e.g., combustion cans, blades, and vanes) of the hot sections of aerospace and land-based gas turbines against the high temperature environment. The state-of-the-art TBC system is currently formed by a metallic bond coat (typically PtAl or MCrAlY, M = Ni and Co) and a zirconia–yttria (ZrO_2–7–8 wt% Y_2O_3) (YSZ) top coat. The typical thicknesses of TBCs vary

R. Shoja Razavi (✉) · M.R. Loghman-Estarki
Department of Materials Engineering, Malek Ashtar University of Technology, Shahin Shahr, Iran
e-mail: Shoja_r@yahoo.com; Shoja_r@mut-es.ac.ir

A.K. Mishra (ed.), *Sol-gel Based Nanoceramic Materials: Preparation, Properties and Applications*, DOI 10.1007/978-3-319-49512-5_2

between 100 and 500 μm, and they can provide a major reduction in the surface temperature of the metallic components up to 300 °C, when combined with the use of internal air cooling of the underlying metallic component. Due to this characteristic, TBCs allow gas turbine engines to operate at temperatures higher than that of the melting point of the metallic components of turbines (superalloys), which is approximately 1300 °C. Therefore, TBCs enable an increase in the efficiency and performance, and a reduction in the pollution levels of these types of engines.

Design of microstructure of zirconia-based TBCs is possible by the control of composition, fabrication route, and thermal treatment of original feedstock. Furthermore, researches show that TBCs prepared from nanostructured feedstock exhibit interior mechanical properties, thermal shock resistance, hot corrosion resistance, lower thermal conductivity, and higher life time as compared as compared with conventional TBCs. Thus, the synthesis of nanostructured zirconia-based powder is important for controlling properties of TBCs. The wet chemical synthesis method of nanosized-REZ and nano-metal oxide stabilized zirconia, such as ZrO_2 stabilized with MgO, CaO, Y_2O_3, Al_2O_3, and CeO_2 and some codoped rare earth stabilized zirconia, especially ceria, yttria stabilized zirconia (CYSZ) and scandia, yttria stabilized zirconia (ScYSZ), and zirconia–alumina nanocomposite are discussed in this chapter.

2.2 Zirconia Structure and Its Applications

At atmospheric pressure, pure zirconia has three solid polymorphs which exhibit three well-defined polymorphs: monoclinic (m), tetragonal (t), and cubic (c) phases. The monoclinic crystalline phase is stable at room temperature and transforms to the tetragonal phase with lattice contraction at ~1170 °C. On further heating at ~2270 °C, the tetragonal phase transforms to cubic phase with lattice expansion [1–3]. On cooling, the reverse transformation occurs. Space group, lattice constants, Zr–O bond lengths, and point group symmetry around Zr sites are summarized in Table 2.1 [4].The structure of zirconia polymorph was shown in Fig. 2.1. However,

Table 2.1 Crystal structure of cubic-, tetragonal-, and monoclinic-ZrO_2 (Reprinted with permission from Ikeno et al. [4], Copyright © 2013, Institute of Physics [IOP])

Compounds	Space group	Lattice constants (Å, deg)	Point group symmetry	Zr–O bond length (Å)
c-ZrO_2	$Fm\bar{3}m$	a = 5.1291	O_h	2.2210 (×8)
t-ZrO_2	$P4_2/mnc$	a = 3.64 c = 5.27	D_{2d}	2.065 (×4) 2.463 (×4)
m-ZrO_2	$P2_1/c$	a = 5.145 b = 5.2075 c = 5.3107 β = 99.23	C_1	2.189 (×1) 2.285 (×l) 2.163 (×l) 2.220 (×l) 2.057 (×l) 2.151 (×l)

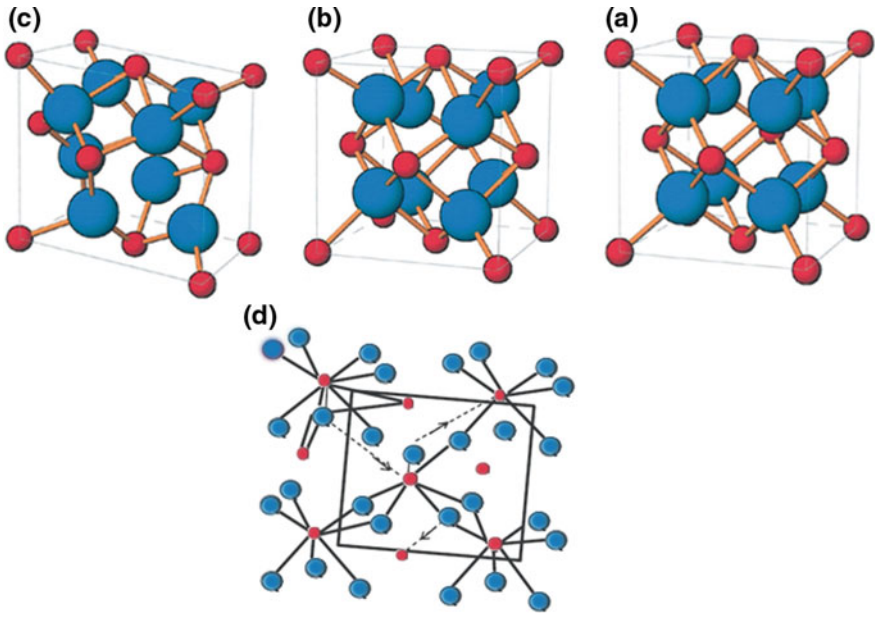

Fig. 2.1 Schematic representation of the three polymorphs of ZrO_2 and the corresponding space groups: **a** cubic, **b** tetragonal, and **c** monoclinic *red* and *blue spheres* indicate Zr and O ions respectively **d** changing in coordination of Zr atoms from seven to eight fold

transformation of t m phase was caused damage in TBC due to increasing 3–5% in volume of resulted m-phase. The tetragonal structure of zirconia is shown in Fig. 2.1b. The unusual volume change, i.e., contraction on heating and expansion on cooling, during t → m phase transformation leads to extensive cracking The transformation of the monoclinic to tetragonal form is not straight forward and has martensitic nature. The most significant event occurring during this transformation is the change in coordination of Zr atoms from seven to eightfold. The probable atomic route by which this increasing in coordination is achieved is indicated in Fig. 2.1d [5].

The applications of zirconia strongly depend on both crystal structure and phase transformations [6]. Fully stabilized zirconia (Cubic phase of zirconia) are found to be useful in high-temperature solid oxide fuel cells (SOFC), high-temperature pH sensors, oxygen sensors, water electrolyzers, oxygen sensors, electrochemical capacitor electrodes, and ferrules due to its ionic, electrical, and optical properties. Tetragonal zirconia can be used as an effective catalyst due to unique amphoteric characteristics and redox properties. The transformable tetragonal zirconia (called t-phase) used as engineering ceramic material (useful for refractory materials and as abrasives) it shows high values of strength and hardness. This hardening mechanism is due to the transformation of the tetragonal phase into the monoclinic phase which implies a volume change associated with pseudoplasticity. The 'non-transformable' metastable tetragonal phase (called t′) [7] is remarkably resistant and does not

Table 2.2 Applications of zirconia and related oxide materials (Reprinted with permission from Patil et al. [5], Copyright © 2008, World Scientific)

Materials	Applications
ZrO_2	Heat resistance lining in furnace, opacifier for organic glazes, glower in incandescent light, abrasives
ZrO_2/Cu–ZrO_2	Catalyst for methanol synthesis
CeO_2–ZrO_2	Oxygen storage capacitor (OSC)
ZrO_2–CaO–Ta_2O_5	Electrode in MHD channel
Stabilized ZrO_2–CaO, MgO, Y_2O_3 (YSZ)	Solid electrolyte in fuel cells, sensors, water electrolyzers, O_2 semipermeable membrane, high-temperature heating elements, cathode in plasma torch
Ni–YSZ	Anode material for SOFC
TiO_2–ZrO_2	Dielectric resonator for microwave applications
$ZrSiO_4$ (Zircon)	American diamond
Partially stabilized zirconia	Extrusion and wire drawing dies, hammers, knives, automotive parts, bearings, thermal barrier coatings
Rare earth dopped	Glazes, gemstones, enamels, and pigments for tiles, tableware, sanitaryware
ZrO_2–Al_2O_3	Heat engines, rocket nozzles, cutting tools, grinding wheels
Pb(Zr,Ti)O_3	Gas igniters, recording pick ups, ultrasonic transducers, echo sounders, microphones, and loud speakers
Pb,La(Zr,Ti)O_3	Optical shutter
$Ln_2Zr_2O_7$, $CaTi_2$–ZrO_7	Refractories, radio-active waste disposal, high-temperature heating elements, electrodes in MHD generators
Ln_2(Eu)Zr_2O_7	Host for fluorescent centers
NASICONs ($MZr_2P_3O_{12}$, M = Na, K, ½ Ca)	Solid electrolyte membranes for energy storage (batteries) energy conversion, electrochemical sensors, electrochromic displays, electrolysis of sodium chloride, immobilization of radioactive wastes, catalyst supports, spark plugs, heat exchangers, optical mirror substrates

undergo the transformation to the monoclinic phase under stresses. The t′ phase is widely used for thermal barrier applications due to the formation of a tweed microstructure which tends to increase the thermo mechanical performances [8]. This microstructure corresponds to a three-dimensional pseudoperiodic lattice of stabilizer or dopant agent (such as MgO, Y_2O_3, CeO_2, Sc_2O_3, etc. particles) with in all of the t′ grains [7]. In description of next section, we explain how one can determine t′ phase from t- and c-phase of zirconia. Some applications of zirconia and related oxide materials are summarized in Table 2.2 [5].

2.2.1 Types of Stabilized Zirconia

As mentioned at the beginning of the chapter, pure zirconia is transformed from tetragonal to monoclinic phase and thus volumetric changes are associated with this

transformation when temperature is changed. This transformation is not desirable in the application of thermal barrier coatings. Therefore, it can be stabilized with either CaO (5 wt%), MgO (15–24 wt%), or Y_2O_3 (6–12 wt%) [1]. These stabilizers allow the stabilization of both the metastable tetragonal phase and cubic phase of zirconia.

The selection of TBC materials is restricted by some basic requirements [9–11]: (1) high melting point, (2) no phase transformation between room temperature and operation temperature, (3) low thermal conductivity, (4) chemical inertness, (5) thermal expansion match with the metallic substrate, (6) good adherence to the metallic substrate, and (7) low sintering rate of the porous microstructure. The advantages and disadvantages of main TBC materials are compared with conventional YSZ and listed in Table 2.3.

Table 2.3 TBC materials and their characteristics (Reprinted with permission from Cao et al. [9], Copyright © 2004, Elsevier)

Materials	Advantages	Disadvantages
7–8 YSZ	(1) High thermal expansion coefficient (2) Low thermal conductivity (3) High thermal shock resistance	(1) Sintering above 1473 K (2) Phase transformation (144.1 K) (3) Corrosion (4) Oxygen-transparent
Mullite	(1) High corrosion resistance (2) Low thermal conductivity (3) Good thermal-shock resistance below 1273 K (4) Not oxygen-transparent	(1) Crystallization (1023–1273 K) (2) Very low thermal expansion coefficient
Alumina	(1) High corrosion resistance (2) High hardness (3) Not oxygen-transparent	(1) Phase transformation (1273 K) (2) High thermal conductivity (3) Very low thermal expansion coefficient
YSZ + CeO_2	(1) High thermal expansion coefficient (2) Low thermal conductivity (3) High corrosion resistance (4) Less phase transformation between m and 1 than YSZ (5) High thermal-shock resistance	(1) Increased sintering rate (2) CeO_2 precipitation (>1373 K) (3) CeO_2-loss during spraying
$La_2Zr_2O_7$	(1) Very high thermal stability (2) Low thermal conductivity (3) Low sintering (4) Not oxygen-transparent	(1) Relatively low thermal expansion coefficient
Silicates	(1) Cheap, readily available (2) High corrosion resistance	(1) Decomposition into ZrO_2 and SiO_2 during thermal spraying (2) Very low thermal expansion coefficient

Improvement of YSZ TBCs: (1) post-deposition of the coating with sealants [24, 25] or laser irradiation of the coating surface [26] for belter corrosion resistance; (2) gradient [6, 27, 28] or multilayered [6, 29–32] coatings with other materials; (3) thick TBC for better thermal insulation [33, 34]

Creation of nanostructure materials is a promising approach to yield modern TBCs. In recent years, nanostructured zirconia-based TBCs deposited by atmospheric plasma spraying have received considerable attention because of some astonishing properties (such as improving thermal shock and hot corrosion resistance, lower thermal conductivity, higher life time) not found in their conventional counterparts [12–14]. These nanostructured TBCs produced from nanopowder. Generally, first, zirconia-based nanopowders produced in at least 300–500 g with liquid phase techniques. Then, due to low density and poor flowability of nanoparticles, the as-obtained nanopowders were granulated with spray drying method. The preparation details of zirconia-based nanogranules were published in our recent literatures [15, 16]. Nanostructured partially stabilized zirconias can be prepared by solid or liquid or gas phase. The solid phase, such as ball-milling method is easy to handle but impurities was inserted in the sample. The gas phase route needs high cost equipment but have more ability to scale up. Liquid phase techniques (such as wet chemical synthesis) are easy to control more homogeneity, purity, and low cost as compared to solid or gas phase method. Thus, in continue, we discuss about the synthesis of some important nanostructured stabilized zirconia powders for TBCs application via three simple wet chemical synthesis including especially combustion, coprecipitation and sol–gel method. In some case, the spray pyrolysis, microwave-assisted and melting salt method were studied. It should be mentioned that the order of TBC material was introduced below is in accordance with history of using it as TBCs.

2.2.1.1 Magnesia-Stabilized Zirconia

Magnesia-stabilized zirconia (MSZ, 15–24 wt% MgO) ceramic powders have been extensively used for more than 30 years to protect sheet metal combustor, resist the effects of molten copper or aluminum on various types of molds and troughs, resist particle erosion at temperatures of about 845 °C (1550 °F) on missile nose cones, and serve as thermal barrier on brazing and heat treating, and coatings on tuyeres for iron forging or refining operations. However, Pratt and Whitney company used MgO-stabilized zirconia TBCs on burner cans in 1963 [17]. Among different materials, ZrO_2–MgO ceramic powder is relatively cheaper than ZrO_2–Y_2O_3. That is why, it is utilized in those regions where the temperature intensity is relatively low, e.g., in the exhaust of the jet engines. Further, a MgO-stabilized system can be used for the development of an intermediate coating in a three-part graded coating system with magnesium zirconate as a top coat [18]. Furthermore, on the basis of reaction, MgO-stabilized ZrO_2 would be expected to be more resistant to vanadium fuel impurities than YSZ; and this appears to have been found in marine engine service [19]. Disadvantage of 24% MgO $\pm$ ZrO_2 is most difficult to plasma spray because of its tendency to vaporize at elevated temperatures. Furthermore, MSZ is known to exhibit destabilization of c-ZrO_2 to m-ZrO_2 when exposed to temperatures above 950 °C [20]. This degradation reaction results in an increase in its thermal conductivity as well as structural disintegration.

Recently, a number of methods have been used to synthesize magnesia-stabilized zirconia nanoparticles, such as in situ peptization of coprecipitated oxalate gel, combustion method, alkoxide sol–gel processing and Pechini-type sol–gel method [21–26]. In continue, we review some of these synthesis methods.

Settu [27] was reported synthesis of MgO–ZrO_2 nanopowders by using three methods of chemical coprecipitation, peptization and alcohol washing methods. In a typical synthesis of MgO–ZrO_2 nanopowders by coprecipitation, the solutions of 0.7 M of $ZrOCl_2{\cdot}8H_2O$, $Mg(NO_3)_2{\cdot}6H_2O$ (corresponding to 7 mol% of MgO and 93 mol% of ZrO_2 in the final oxide powder) were intimately mixed in a glass beaker using a stirrer and paddle. Then, the $H_2C_2O_4{\cdot}2H_2O$ solution was added dropwise into the vigorously stirred mixed cation solutions, which yielded a white gelatinous precipitate and was allowed for 12 h to settle down. The resultant precipitate was filtered and divided into three batches, which were designated as P1, P2, and P3, respectively. The third batch of the precipitate was washed thoroughly with ethyl alcohol. All these powders were oven dried at 50 °C until water gets evaporated. The dried powders P1, P2, and P3 were all calcinated at 470–850 °C for 1 h to ascertain crystallization temperature using powder X-ray diffraction.

The steps of in situ peptization of MgO–ZrO_2 Powder were shown in Scheme 2.1. X-ray diffraction pattern for the calcinated powders reveal that all samples are in tetragonal phase (Fig. 2.2). The precipitated and peptized powders show almost same characteristics for TGA and DTA analysis where as the alcohol washed powder behaves differently. Surface area analysis shows the alcohol washed powder has more specific surface area than the other two powders which is due to the interaction of alcohol with inter particle surfaces of powder (Table 2.4).

The zirconia–magnesia (ZrO_2–x mol% MgO; x = 3–90) solid solutions were prepared by the citrate gel method [28]. The metastable tetragonal (t′) form was determined in MgO-doped ZrO_2 calcinated at 800 °C. Samples containing up to 50 mol% MgO were revealed to be monoclinic ZrO_2 solid solution and MgO when calcinated at 1000 °C. Moreover, ZrO_2–x mol% MgO (x = 60–90) solid solutions have metastable tetragonal t′ with MgO phase at 800 and 1000 °C, whereas no cubic phase was determined at any compositions of zirconia-based solid solutions. In this study, citric acid was completely dissolved in water. Then, $ZrOCl_2{\cdot}8H_2O$ (35.70% as ZrO_2) was added to aqueous solution before $MgCO_3$ (43.4% as MgO) stabilizer was introduced to the mixture at room temperature. When the clear solution was obtained, temperature on magnetic stirrer was adjusted to 200 °C. After couple hours, gelation initiated, which was confirmed by color and viscosity changes in the mixture. The gel was conveyed to a mantle heater where temperature was adjusted to 400 °C for 8 h to remove organic matters. Finally, browny black agglomerated powders or citrate gel precursor were obtained. Heat treatment was carried out to powders at various temperatures (from 400 to 1500 °C) for 2 h. In ZrO_2–(3–50) mol% MgO solid solutions, as calcination temperature increased, t′-ZrO_2 transformed to m-ZrO_2. This is attributed to enhancement of the crystallite size at higher temperature (Fig. 2.3). Gocmez [28] mentioned that the nucleation and propagation of microcracks were responsible for overcoming a high-energy barrier, ΔG^{*} t′ → m. The crystallite size effect governs both the statistic of

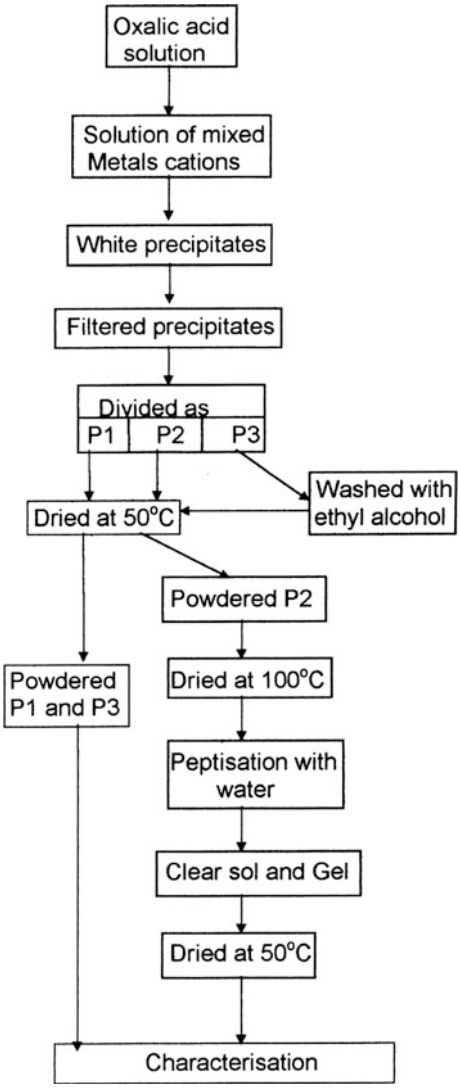

Scheme 2.1 Flow chart for preparation of different MSZ nanopowder (Reprinted with permission from Settu [27], Copyright © 2000, Elsevier)

martensitic nucleation and the propagation of the t′ → m transformation. On the other hand, in the ZrO_2–(60–90) mol% MgO sample, it was found that the t″ → t′ transformation is not related to the crystallite size (varied from 24 to 47 nm) in this study, reflecting the small energy barrier, ΔG^{*} t′ − t. TEM image (Fig. 2.4) showed that synthesized powders have equiaxed-rounded shape and crystallite size (40–50 nm) was in good agreement with XRD results (47 nm).

The cubic to tetragonal phase transition in doped zirconia occurs by an elongation of the crystallographic c axis and a concomitant displacement of the oxygen atoms from the ideal anion sites in the fluorite (cubic phase f zirconia) structure.

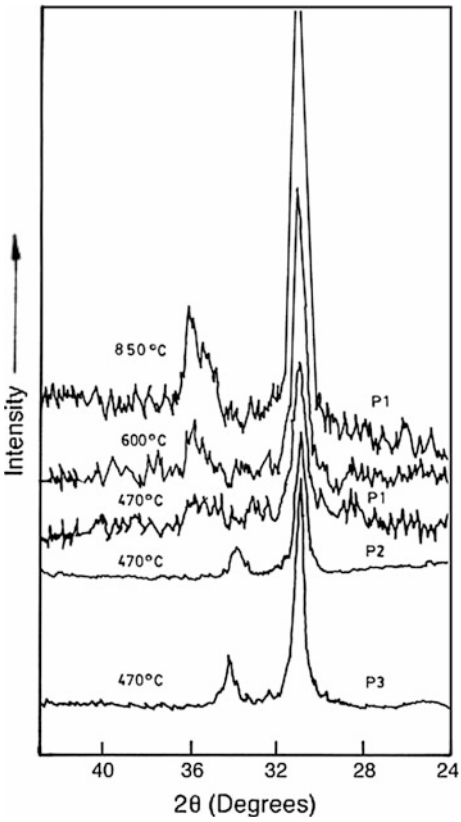

Fig. 2.2 X-ray diffraction pattern as a function of heat treatment for the different samples of MSZ: *P1* as-precipitated powder; *P2* peptized powder; *P3* alcohol washed powder (Reprinted with permission from Settu [27], Copyright © 2000, Elsevier)

Table 2.4 Variation of surface area and MSZ particle size as a function of temperature (Reprinted with permission from Settu [27], Copyright © 2000, Elsevier)

	PI			P2			P3		
Calcination temperature (°C)	470	600	850	470	600	850	470	600	850
Specific surface area (m^2 g^{-1})	48	22	6	55	28	8	68	37	11
Average crystallite size (nm)	27	58	192	25	49	165	22	37	159

Raman spectroscopy is sensitive to the polarizability of the oxygen ions and therefore, it can be used to determine the symmetry of a crystal system. Raman spectroscopy is a nondestructive experimental technique for probing the vibrational and structural properties of materials. It is also recognized as a powerful tool for identifying different polymorphs of metal oxides. Ruiz-Trejo [29] was reported that the other way to distinguish c-phase from t-phase of zirconia is that the c-phase

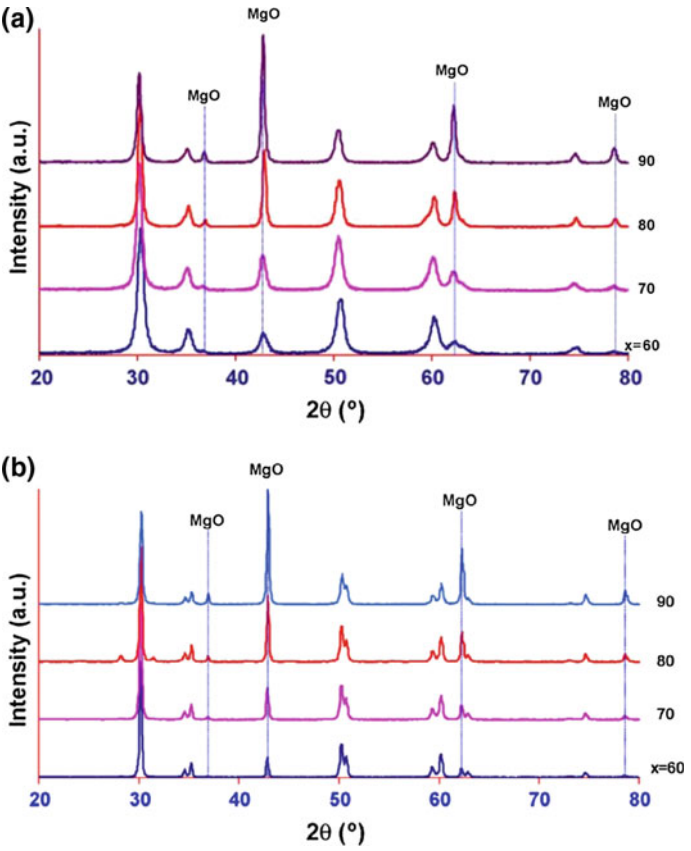

Fig. 2.3 The XRD patterns of ZrO_2 containing (60, 70, 80, and 90) mol% MgO At (**a**) 800 °C (**b**). 1000 °C (Reprinted with permission from Gocmez and Fujimori [28], Copyright © 2008, Elsevier)

show high intensity fluorescence (FL) between 1000 and 2000 cm^{-1} but t-phase of zirconia emitted very weak FL peak. Table 2.5 shows the activities of the allowed zone center mode in zirconia for several different structures [29–35]. According to group theory, monoclinic (m-ZrO_2), tetragonal (t-ZrO_2), and cubic zirconia (c-ZrO_2) are expected to have 18 (9Ag + 9Bg), 6 ($1A_{1g}$ + $2B_{1g}$ + $3E_g$) and 1 (F_2g) Raman active modes. It is worth noting that the six Raman frequencies of t-zirconia in different literatures are in the range of (i)131 (E_g mode)-155(B_{1g}), (ii) 240(E_g)-266 (A_{1g}), (iii) 290 (B_{1g})-330 (E_{1g}), (iv) 410 (E_{1g})-475 (E_g), (v) 550 (A_{1g})-615 (B_{1g}), (vi) 616 (E_g)-645 [29–35].

Raman spectroscopy was also used to distinguish between cubic and tetragonal structures. Six characteristic bands of the tetragonal zirconia were observed in the Raman spectrum (Fig. 2.5) of ZrO_{2-x} mol% MgO (x = 60–90). The peak around 470 cm^{-1} shows the tetragonal phase, which cannot be attributed as the cubic phase [36].

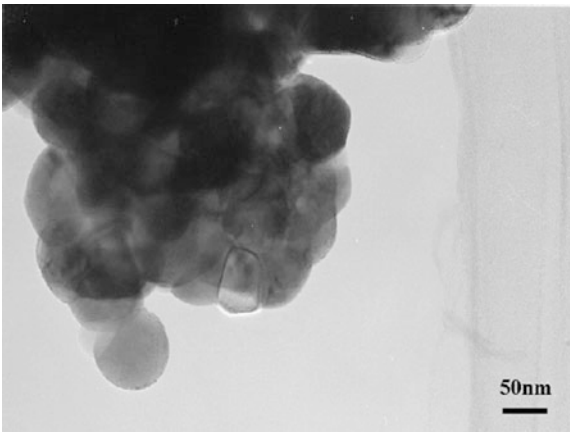

Fig. 2.4 TEM micrographs of the ZrO_2–60 mol% MgO solid solution prepared by the citrate gel method at 1000 °C (Reprinted with permission from Gocmez and Fujimori [28], Copyright © 2008, Elsevier)

Table 2.5 Allowed active mode for several different structure of zirconia (Reprinted with permission from Davar et al. [6], Copyright © 2013, Elsevier)

Method	Cubic	Tetragonal	Monoclinic
IR	F_{1u}	$A_{2u} + 2E_u$	$8A_u + 7B_u$
Raman	F_{2g}	$A_{1g} + 2B_{1g} + 3E_g$	$9A_g + 9B_g$

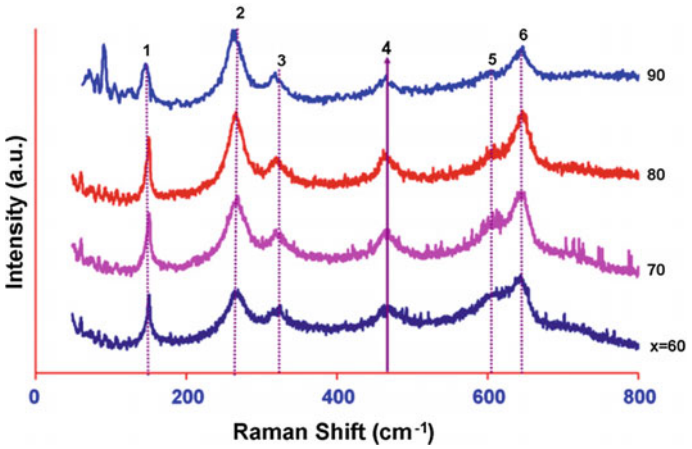

Fig. 2.5 Raman spectrum of ZrO_2–(60, 70, 80, and 90) mol% MgO at 800 °C (Reprinted with permission from Gocmez and Fujimori [28], Copyright © 2008, Elsevier)

Magnesia-stabilized zirconia powders (7 mol–14 mol% MgO) are prepared by the combustion of an aqueous solution containing stoichiometric amounts of zirconyl nitrate, magnesium nitrate, and carbohydrazine (CH) in a cylindrical Pyrex dish [37]. The solution when heated rapidly at 350 °C boils, foams, and ignites to burn with a flame yielding voluminous foamy zirconia powder in less than 5 min. During combustion, the magnesium nitrate added to the redox mixture decomposes to MgO and stabilizes the high-temperature ZrO_2 phase. The equivalence ratio for zirconium oxynitrate/magnesium nitrate and CH is 1:1.25. The combustion product shows the fully crystalline nature of zirconia powders (Fig. 2.6). The 7MSZ nanoparticle with average size of 60–70 nm was obtained by this method.

As the calcination temperature is increased, the concentration of monoclinic phase also increases. The t-phase disappears only after the specimen is heated to 1500 °C. The variation in the lattice parameters of ZrO_2–7 mol% MgO with calcination temperature are calculated and are shown in Table 2.6. The data reveal that the cell parameter values decrease as the calcination temperature of the combustion residue increases.

With an increase in the calcination temperature, the tetragonality (c/a) initially increases and then it decreases as the percentage of MgO content increases. The properties of ZrO_2–MgO powders are summarized in Table 2.7. The powder densities of ZrO_2 are in the range of 50–60% of theoretical density and the surface areas in the range of 8–14 m^2g^{-1}. As the MgO content increases there is a slight increase

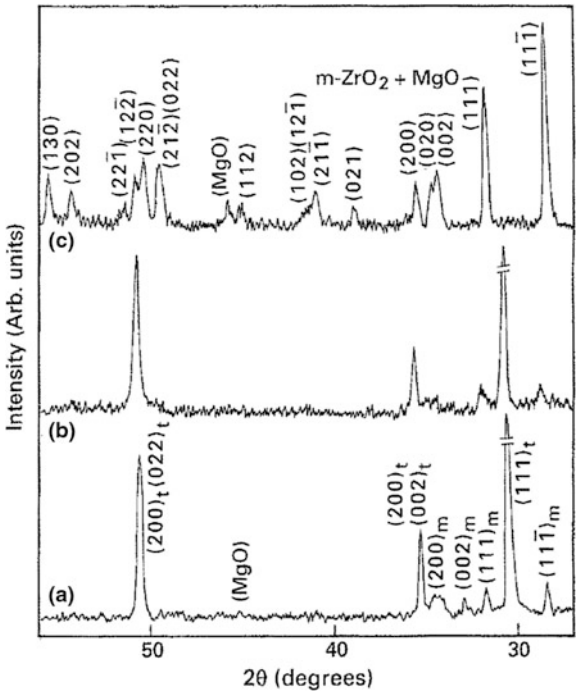

Fig. 2.6 XRD patterns of calcinated ZrO_2–7 mol% MgO: **a** 950 °C, **b** 1150 °C, and **c** 1500 °C (Reprinted with permission from Arul Dhas and Patil [37], Copyright © 1993, Springer)

Table 2.6 Variations of cell parameters of MSZ with temperature (Reprinted with permission from Arul Dhas and Patil [37], Copyright © 2008, Elsevier)

Temperature (°C)	Lattice parameter			Monoclinic phase (%)
	a (nm)	*c* (nm)	*c/a*	
As-formed	0.51331	0.51558	1.006	–
950	0.50974	0.51420	1.009	14
1150	0.50953	0.51350	1.007	15
1250	0.50935	0.51280	1.006	17

Table 2.7 Particulate properties of combustion-derived ZrO_2–MgO nanopowders (Reprinted with permission from Arul Dhas and Patil [37], Copyright © 1993, Springer)

Number	Material	Phases[a] by XRD	Crystallite size[b] (nm)	Powder density (kg m^{-3})	Surface area (m^2 g^{-1})	Average agglomerate size (μm)
1	ZrO_2–7 mol% MgO	t	29.0	3200	8	1.8
2	ZrO_2–9 mol% MgO	t + c	26.0	3300	10	2.3
3	ZrO_2–14 mol% MgO	c	24.0	3400	14	2.5

[a]*t* tetragonal; and *c* cubic
[b]From X-ray-line broadening

in the surface area while the crystallite size decrease. This occurs possibly due to the increase in the defect concentration indicating single-phase ($Zr_{1-x}Mg_xO_{2-x}$) formation of the combustion residue.

There are mainly five most popular procedures on the basis of sol preparation for the sol–gel derived powders by the thermal crystallization of gel pieces synthetic protocol. These include the use of (i) "all alkoxides" (as the source of cations), followed by hydrolysis–condensation, (ii) alkoxides and salts, (iii) "all salts," followed by processing to sol formation, (iv) "all salts," along with suitable polymers or other organics for gel formation, and (v) all or partial colloidal sols [38]. However, metal alkoxides are the most important precursors employed in sol–gel processing through the hydrolysis and polycondensation of metal alkoxides mechanism, ending up with the formation of metalloxane bonds. Sol represents "colloidal solutions," and polymerizable complex (PC) method seems to be the easiest and the most elegant variation of sol–gel methods. In this method, unlike metal alkoxides route, there is the conversion of "polymer solutions" and not "colloidal solutions" into the gels. It is also called "sol–gel transition." Actually,"polymer solutions" is not called a "sol." However, no other terms other than sol–gel transition can represent this kind of conversion, and it should be recognized that "sol–gel method" is a processing that passes through sol–gel transition regardless of the types of precursors [38].

Among wet chemical methods for synthesizing MSZ nanopowders, Pechini's method, which is the main kind of polymerizable complex method, was used because it made it relatively easy to produce nanoparticles. In Pechini sol–gel process, an alpha-hydroxycarboxylic acid such as citric acid is used to chelate with various cation precursors forming a polybasic acid. In the presence of a polyhydroxy alcohol, such as ethylene glycol, these chelates will react with the alcohol to form organic esters and water. By heating the mixture, polyesterification occurs, yielding a homogeneous sol; metal ions are found to be uniformly distributed throughout the organic matrix in that sol. The crystallization occurs simultaneously with the elimination of the organic matter in a subsequent thermal treatment, giving rise to a crystalline material with high chemical and structural homogeneity [39].

Recently, our groups [39] were synthesized MgO–ZrO_2 nanopowders by Pechini sol–gel method. Solutions of $ZrOCl_2$–$8H_2O$, $Mg(NO_3)_2 \cdot 6H_2O$ (corresponding to 24 wt% of MgO and 76 wt% of ZrO_2 in the final oxide powder) were prepared by slowly adding the respective salts in a constantly stirred water-containing glass beaker. The prepared solutions of $ZrOCl_2 \cdot 8H_2O$ and $Mg(NO_3)_2 \cdot 6H_2O$ were well mixed in a glass beaker using a magnetic stirrer and hot plate. Then, the citric acid solution and ethylene glycol were added into the stirred mixed cation solutions, thereby yielding a colorless solution that was allowed to settle down at the temperatures of 100, 200, and 300 °C, each for 2 h. All these precursors were oven dried at 250 °C until water and other organics were evaporated. The resultant burned gel was calcinated in a furnace at different temperatures and times according to M16 array of Taguchi experiment design. Table 2.8 was summarized experiment factors, levels and particle size of the as-synthesized MSZ nanopowders. Figure 2.7 illustrates the chemical reactions involved in this process and presents one feasible structure of the polymer.

Consequently, citric acid to ethylene glycol mole ratio (CA/EG) and citric acid to transition metal mole ratio (CA/TM) were found to be the main parameters having a significant effect on particle size and the size distribution of magnesia-stabilized zirconia nanoparticles, respectively. In optimal conditions of this method (sample 2, magnesia-stabilized zirconia nanoparticles (20–30 nm) with homogeneous particle size distribution were prepared and the results were in a good agreement with the predicted data as examined by Taguchi method (sample 2 in Table 2.8). Furthermore, in Pechini sol–gel process, for synthesizing MSZ nanoparticles, it was found out that the formation of the tetragonal and monoclinic ZrO_2 in some cases and, the cubic MgO phase in all samples indicated that the departure of the rapid solidification from equilibrium was more than that of the sol–gel process. Furthermore, the thermal conductivity and diffusivity of nano-MSZ are lower than that of traditional magnesia-stabilized zirconia. The grain size of optimal MSZ is 20–30 nm (Fig. 2.8), which is comparable to phonon mean free path owing to grain-boundary scattering. The small grain size leads in lower thermal conductivity owing boundary thermal resistance endorsed by phonon scattering at grain boundaries [40, 41].

The variation in thermal diffusivity and thermal conductivity values of conventional MSZ and nano-MSZ from room temperature to 1300 °C are presented in

Table 2.8 Experiment factors, levels and particle size of the synthesized MSZ powders (Reprinted with permission from Hajizadeh-Oghaz et al. [39], Copyright © 2015, Elsevier)

Experiment no.	CA/EG	CA/TM	Calcination temperature (°C, ±5)	Calcination time (h)	Average particle size (nm, ±1)
1	1	1	600	4	17
2	1	2	700	6	19
3	1	3	800	8	14
4	1	4	900	4	21
5	2	1	700	8	22
6	2	2	600	4	20
7	2	3	900	4	19
8	2	4	800	6	30
9	3	1	800	4	32
10	3	2	900	8	20
11	3	3	600	6	34
12	3	4	700	4	38
13	4	1	900	6	20
14	4	2	800	4	27
15	4	3	700	4	30
16	4	4	600	8	31
Total	40	40	40	28	

Fig. 2.9. In both MSZ significant increase of α(T) was observed at the temperature range of 800–1300 °C. This was predominantly caused by the precipitation of the MgO from the zirconia matrix leading to unstabilization of the cubic/tetragonal zirconia (c/t–ZrO_2 to m–ZrO_2). Furthermore, at high temperatures, radiative heat transfer through the material in the course of the thermal diffusivity measurement might lead to this apparent increase [40].

2.2.1.2 Calcia-Stabilized Zirconia (CaSZ)

CaO–ZrO_2 compositions show poor stability with respect to spraying parameters [42]. Moreover, this TBC material show low thermal shock resistance as compared with conventional YSZ TBC. Due to these disadvantages of 5CaSZ, to the best of our knowledge, there is not any report about synthesizing 5CaSZ nanopowders for TBC application. However, the calcia-stabilized zirconia with more than 5 wt% stabilizer (such as 10–15 CaSZ) have huge application in solid electrolyte fuel cell. It seems the general strategies for wet chemical synthesis of CaSZ were similar to that of MSZ nanopowders. However, in this section, potential scale-up method (spray pyrolysis method) for synthesizing of this nanopowder was studied.

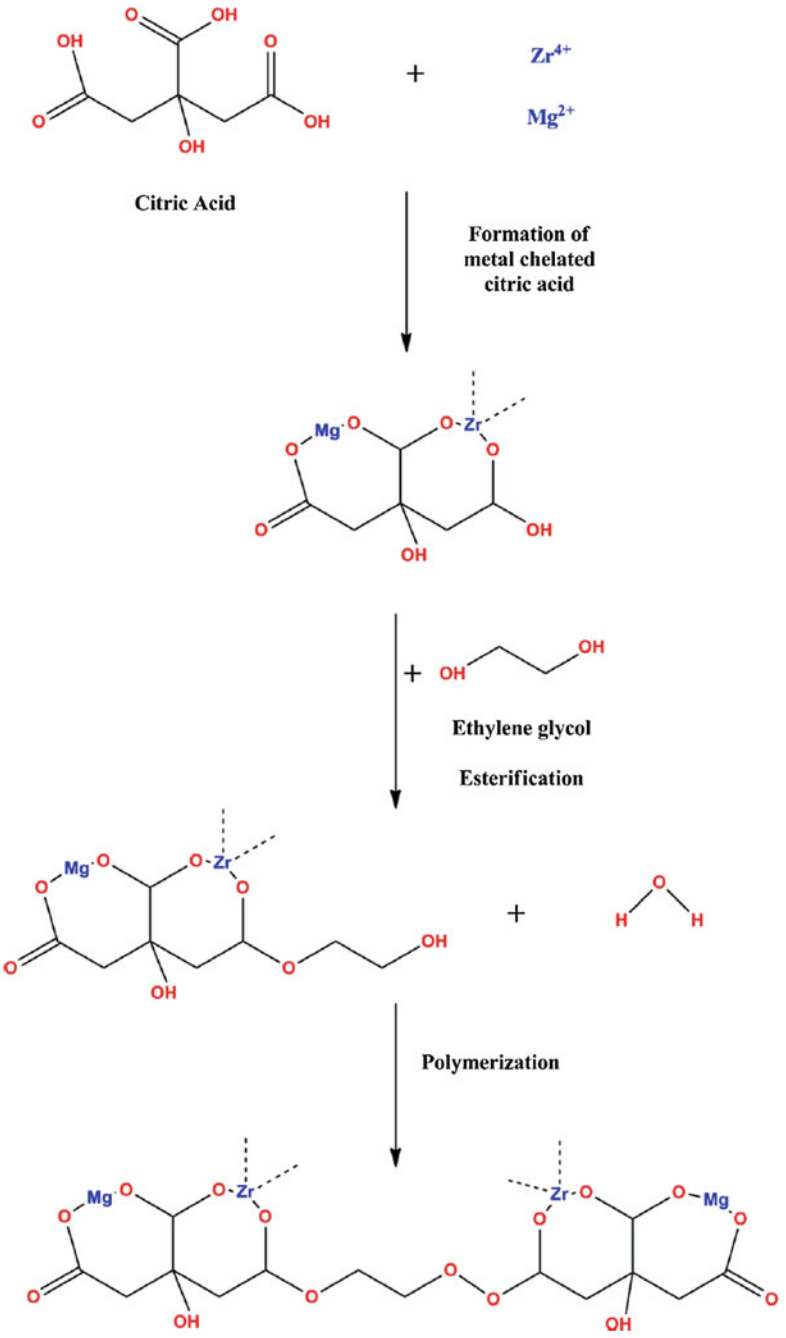

Fig. 2.7 Schematic illustration showing the solution chemistry and reactions involved in the Pechini process (Reprinted with permission from Hajizadeh-Oghaz et al. [39], Copyright © 2015, Springer)

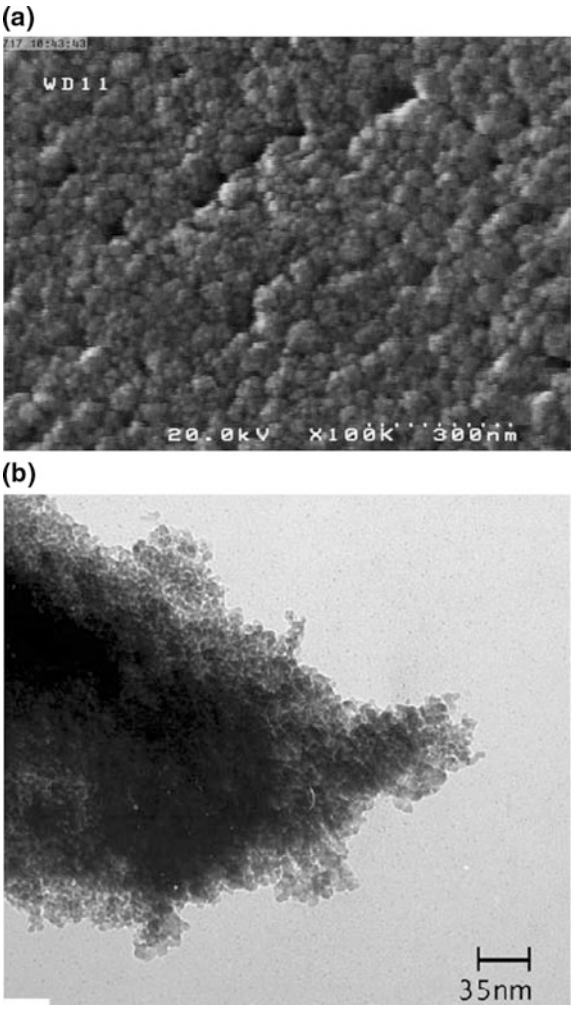

Fig. 2.8 **a** FESEM photograph **b** TEM of the optimal MSZ nanopowder prepared by Pechini method (Reprinted with permission from Hajizadeh-Oghaz et al. [39], Copyright © 2015, Springer)

Nanospherical $Ca_{0.15}Zr_{0.85}O_{1.85}$ (CaSZ, 15 mol% CaO) nanopowders were prepared by spray pyrolysis, starting from a mixed aqueous and ethylic solution of zirconium acetylacetonate and calcium acetate [43]. It has been demonstrated the feasibility to produce CaSZ nanopowders without post-heat treatment with the spray pyrolysis technique. Compared with the traditional method, the powders are obtained in one step, saving time and energy. The powders were synthesized without sintering, and for adequate preparation conditions, were mostly spherical, solid and narrowly size distributed. Average particle size ranges between 40 and 350 nm with controlling solution concentration, furnace temperature, mass flow of carrier gas and voltage of precipitator. Transmission electron micrographs (Fig. 2.10) showed that crystalline calcia-stabilized zirconia particles were constituted by small crystallites,

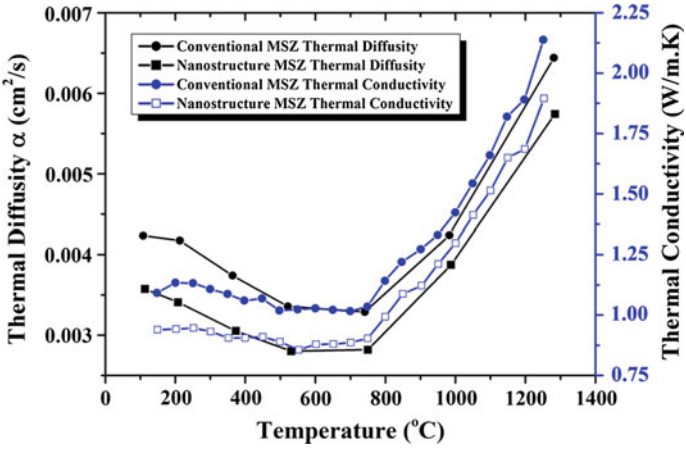

Fig. 2.9 Thermal diffusivity α(T) and thermal conductivity K(T) results of the Conventional [40] and nanostructured MSZ (Reprinted with permission from Rauf et al. [40], Copyright © 2012, Elsevier)

their size varying between 2 and 40 nm. X-ray diffraction analysis shows that powders obtained at low temperature (Below 650 °C) were amorphous; for higher temperatures (800 °C), it is found the presence of the tetragonal and cubic phases (Fig. 2.11).

2.2.1.3 Yttria Stabilized Zirconia (YSZ)

According to phase diagram of YSZ (Fig. 2.12) [5] and NASA research [44], it was shown the best life time of YSZ as a TBC was obtained with 7 wt% (~3.9 mol%) Y_2O_3 as stabilizing agent. The literature reviews show that the different wet chemical methods were used for synthesizing YSZ nanopowder. However, among these methods, for TBC application, the combustion, alkoxide sol–gel, and Pechini methods were the focuses of researchers attend.

Various phases of yttria stabilized zirconia with different mol% of yttria have been prepared as shown in Table 2.9. YSZ (3–10 mol%) nanopowder is prepared by combustion method using zirconyl nitrate, yttrium nitrate, and carbohydrazide as fuel [45]. According to the phase diagram, the tetragonal zirconia phase is stabilized by the addition of 2–3 mol% of yttria. The mixture of tetragonal-cubic phase exists between 3.5 and 6 mol% of yttria and the cubic zirconia phase is stabilized by adding more than 6 mol% of yttria. The yttria-doped zirconia samples show phase stabilization of cubic (fluorite structure) at above 8 mol% of yttria.

The various phases of YSZ nanopowders are identified by XRD patterns (Fig. 2.13). Formation of zirconia solid solution with the additive is confirmed by the change in lattice parameters of ZrO_2. The cell dimensions of stabilized zirconia are larger than pure zirconia (t–ZrO_2: a = 0.50821 nm, c = 0.51682 nm). The

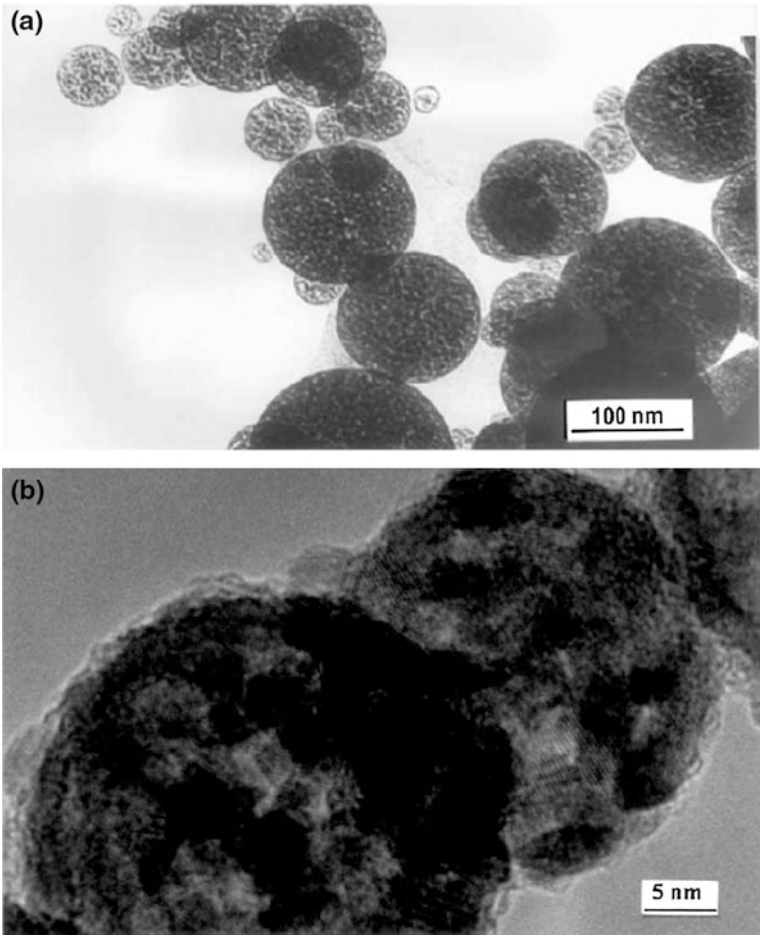

Fig. 2.10 **a** TEM **b** High-resolution TEM micrograph showing a lattice fringe image of CaSZ particles obtained at 900 °C (Reprinted with permission from Esparza-Ponce et al. [43], Copyright © 2003, Elsevier)

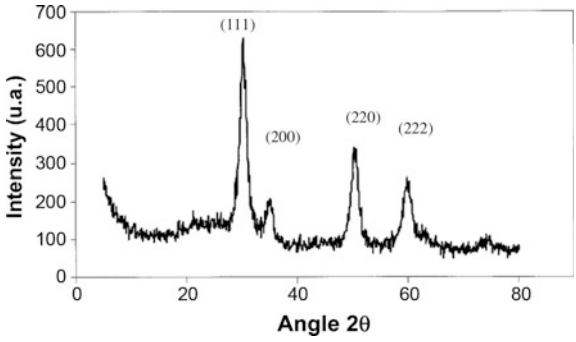

Fig. 2.11 Typical XRD spectra of CaSZ (Reprinted with permission from Esparza-Ponce et al. [43], Copyright © 2003, Elsevier)

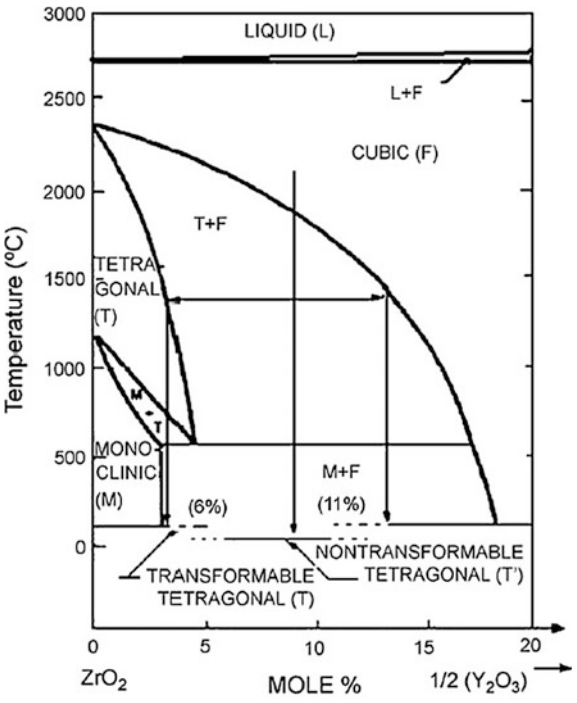

Fig. 2.12 Phase diagram of YSZ (Reprinted with permission from Viazzi et al. [7], Copyright © 2008, Elsevier)

Table 2.9 Particulate properties of YSZ sample synthesized with combustion method [45] (Reprinted with permission from Copyright © 2008, Springer)

Redox mixture	Phases byXRD	Powder density (g cm^{-3})	Surface area (m^2 g^{-1})	Particle size[a] (nm)
ZON/ZN + 3 mol% Y_2O_3 + CH	t(t)	3.4 (3.8)	8.4 (5.4)	210 (292)
ZON/ZN + 4 mol% Y_2O_3 + CH	t + c (m + c)	3.4 (3.6)	3.5 (8.7)	504 (191)
ZON/ZN + 6 mol% Y_2O_3 + CH	c (c)	3.4 (3.6)	3.4 (9.4)	519 (177)

m monoclinic, *t* tetragonal, *c* cubic. Values in parenthesis correspond to zirconia obtained by ZN and CH redox mixture

[a]From surface area

lattice expansion implies that the additive goes into the zirconia lattice forming solid solution of the type (Zr_{1-x} M_xO_{2-x}). The ratio of the cell parameters can be used to distinguish between the two tetragonal phases (t and t′). The ratio $c/a\sqrt{2}$ tends to 1.010 (1.00–1.01) for the t′ cell parameters while it is superior to 1.010 for the t phase (1.01–1.02) [5].

Viazzi and coworkers [5] was synthesized YSZ nanopowders via alkoxide sol–gel method. The starting precursors are the zirconium (IV) propoxide ($Zr(OPr)_4$),

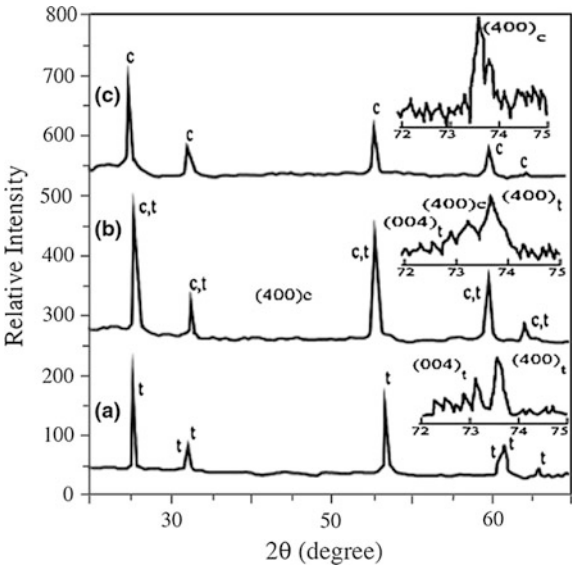

Fig. 2.13 XRD patterns of yttria stabilized zirconia **a** 3 mol% Y_2O_3, **b** 4 mol% Y_2O_3, and **c** 6 mol% Y_2O_3 (Reprinted with permission from Arul Dhas and Patil [46], Copyright © 1992, Springer)

yttrium (III) nitrates hexahydrate and the solvent is 1-propanol. The complexing agents, acetylacetone (AcAc) and acetic acid ($C_2H_4O_2$), have been used to reduce the zirconium alkoxide reactivity toward water and to avoid hydroxides formation. The two molar ratio AcAc/$Zr(OPr)_4$ and H2O/$Zr(OPr)_4$ have been kept constant between 0.8 and 9.5, respectively. A crystallographic study has shown that YSZ nanopowders obtained after calcination at 950 °C (heating rate: 100 °C/h) and it are crystallized in the tetragonal symmetry.

In fact, the acetic acid ($C_2H_4O_2$) is a catalyst towards the hydrolysis reaction as the hydrochloric acid. But $C_2H_4O_2$ is less strong than HCl, so the hydrolysis was not so favored. Consequently, the condensation, in this case, is more favorable because in less acid conditions, there is more free Zr–OH to do the nucleophilic attack. The $C_2H_4O_2$ can also form complexes with $Zr(OPr)_4$ as below:

$$Zr(OPr)_4 + x\text{AcAc} \rightarrow Zr(OPr)_{4-x}(\text{AcAc})_x + x\text{PrOH}. \quad (2.1)$$

These groups show that by using β-diketones (AcAc) as complexing agent, the crystallite size (31 nm) of YSZ was smaller than acetic acid (37 nm). Furthermore, from an experimental point of view, AcAc, i.e., acetyleacetanate, seem to be the easier modifiers to handle [5, 47].

Moreover, coating of YSZ on Ni-based alloys was done by these groups [48–50] through immersion of the substrates in the sols ($Zr(OPr)_4$, yttrium (III) nitrates hexahydrate,1-propanol. acetylacetone as a Zr^{4+}, Y^{3+}, solvent and complexing agent, respectively) and withdrawn at a controlled speed. Then, samples are dried at room temperature and then heat treated. Two heat treatments have been performed: (A) 2 h at 950 °C (heating rate: 100 °C/H) and (B) 30 min at 1150 °C followed by

a 4 h at 950 °C (heating rate: 100 °C/h). The higher temperature of the heat treatment B (1150 °C) corresponds to the maximum applicable temperature for the superalloy. To improve the behavior of the sol during the dip-coating, two binders were used: the dibutylphtalate (DBP) and an equimassic mixture of DBP and polyethyleneglycol (PEG). Results show that the samples obtained with a DBP content of 3 wt% and with a lower withdrawal speed (17 cm/min) are optimal (Fig. 2.14). No differences between both heat treatments (A and B) have been underlined.

The cracking phenomenon in Fig. 2.14 is partly due to the quick densification of the YSZ material during the thermal treatment. This calcination leads to the

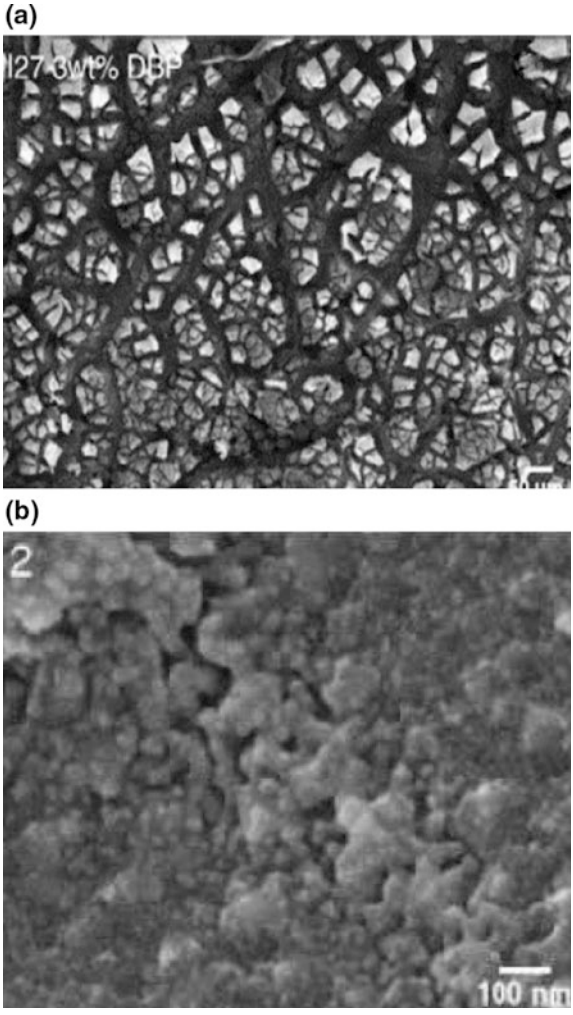

Fig. 2.14 SEM characterization of I-27 (Series I-b), viscosity of the sol: 100 mPa s, 3 wt% DBP, speed of withdrawal: 17 cm/min, heat treatment A (Reprinted with permission from Viazzi et al. [48], Copyright © 2006, Elsevier)

widening of the cracks after the removal of organic compounds but the main point is the important anfractuosities of the NiCrAlY substrate.

Moreover, Lours [51] and coworkers, developed new promising thermal barrier coatings (TBCs) processed by both dip-coating/spraying of sol route deposited onto NiPtAl bond coated superalloy substrates. The dip-coating technique was done similar to Viazzi work [48–50]. Subsequently, specimens with controlled cracks are reinforced using additional filling of YSZ (9.7 mol% $YO_{1.5}$ sol loaded with 10 or 20 wt% of a suspension of well-dispersed commercial YSZ powders in 1-propanol solvent) brought up within crack grooves using spray-coating technique. Between each pass, the coating is dried 5 min at 50 °C and finally the specimens are heat treated 2 h at 1100 °C, using heating and cooling rates of 50 °C/h. The most efficient TBC reinforcement is obtained using two successive passes using a sol loaded with 20 wt% (high viscosity) followed by four passes using a sol loaded with 10 wt% (low viscosity). Figure 2.15a, b show optical micrographs of the sol–gel TBC before and after the sintering heat treatment. Figure 2.15c shows a

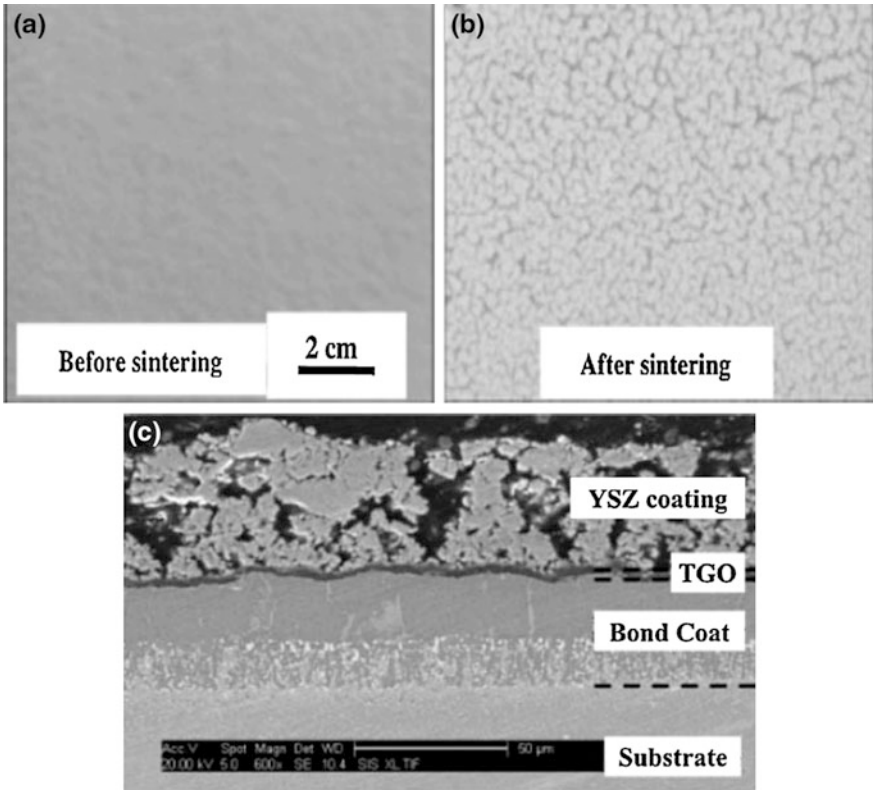

Fig. 2.15 **a**, **b** Optical micrographs of the sol–gel TBC before and after the sintering heat treatment. **c** Cross-section SEM micrograph of a sol–gel TBC (Reprinted with permission from Pin et al. [51], Copyright © 2014, Elsevier)

cross-section micrograph of such an optimized reinforced sol–gel TBC. According to Fig. 2.15c, it was clearly seen clearly three layer of TBC including top coat (YSZ), bondcoat (MCrAlY) and substrate. During postprocessing heat treatment such as cyclic oxidation, an adherent and protective TGO—consisting in a dense α-alumina layer acting as a diffusion barrier—forms and grows at the bond coat/TBC inter-face.

Christel Laberty-Robert and Florence Ansart and coworker [52, 53] were synthesized YSZ nanopowder via Pechini method using zirconium chloride $ZrCl_4$ and and $Y(NO_3)_3{\cdot}6H_2O$, ethylene glycol (EG) and citric acid (CA). These salts were dissolved in distilled water. Since the cation concentration in the polymer influences the morphology and the nature of the phase of YSZ powders, several molar concentrations were investigated. Then, the cation solutions, CA and EG were mixed in a 200 mL beaker, heated at 80 °C and stirred during ~4 h. Complexation and esterification reactions occur and a viscous polymeric product is formed though any visible phase separation. The polymeric solution was then heat treated at 80–100 °C in air during 24 h. The solid black resin thus obtained was calcinated at 400 °C in air for 2 h before final sintering at 1000 °C for 2 h. Raissi group was also used the same method for synthesizing 8YSZ nanopowders by these polymeric complex method. The main difference between Christel Laberty-Robert's work and Raissi's work [54] was to CA/Zr^{4+} mole ratio ($CA/Zr^{4+} = 4$).

According to Laberty-Robert's result, when the CA/Zr^{4+} ratio increase from 0.4 to 5.0, the hydroxycarboxylic acid quantity which can react with polyhydroxyalcohol is more important. Then, in the solution, the polymeric chains are more ramified or more length. This induces a decrease in the mobility of the polymeric chains which conduces to an increase in the viscosity. However, this factor does not influence the morphology of the nanopowder. Considering to these groups results, the following optimal conditions: CA/ $CA/Zr^{4+} = 4.77$ and CA/EG = 1 have been determined and used for the preparation of the YSZ nanopowder. In low CA/ $CA/Zr^{4+} = 0.4$, aggregated particles with surface area of 4 ± 1 m^2 g, while with high CA/ $CA/Zr^{4+} = 4.7–5$, aggregated porous nanoparticles with surface area of 13 ± 1 m^2 g were obtained. This group was also survey the effect of surfactant on agglomeration and morphology of the product. Various commercial surfactants including Igepal CA 630, Igepal NP6, and Triton have been studied. They show that the best result was obtained for Igepal CA 630 [53].

Petrova [55] and coworkers was developed the synthesis of YSZ nanopowders by modified Pechini method by using zirconium–yttrium citric complexes prepared in ethylene glycol and water media. The YSZ nanopowders were obtained by thermal decomposition of the Y–Zr complexes, and isolated from EG medium, instead of decomposing the polyester resin produced following the common Pechini's method. Such an approach shortens the time taken to obtain the final products and decreases the relative content of organic components (relatively to the metal(s) content) preserving the main advantages of the Pechini's method. In this method, the molar ratio of Y^{3+}:Zr^{4+}:CA:EG were 0.08 (or 0.15):0.92 (or 0.85):5:50. The temperature was sharply increased up to 120 °C. The salts completely dissolve in few minutes so a clear solution was obtained. Even a slight opalescence of the solution evidences a

hydrolysis of the Zr-salt, which runs a risk of metals segregation and disruption of the desired Zr/Y mole ratio in the final product. In such a case, the solution has to be discarded. The so-prepared solution was agitated under stirring at the same (120 °C) temperature for 30 min. The processes of complexation (between metal ions and CA) and esterification (between CA and EG) take place in the solution along with an oligomerization leading to a slight increase of the solution viscosity. After cooling of the solution to room temperature, acetone was added to it in large excess which leads to precipitation of the complexes formed. They contain partially esterified CA-ligands and EG, bonded as adduct. The precipitate formed was separated after 24 h, soaked in fresh acetone for 24 h, filtered, dried in a dessicator over silica gel and stored in tightly closed bottle. The individual Zr complex was prepared in analogous way; the molar ratio Zr^{4+}:CA:EG in the initial solution was set to 1:5:50. The molar ratio Y^{3+}:Zr^{4+}:CA:H_2O in the initial solution was set to 0.08:0.92:17.5:300. YSZ nanopowders were prepared from the Y–Zr complexes isolated from the EG medium. They were heated at 450 °C for 2 h and afterwards at 750–1000 °C for 4 h. Spherical YSZ nanopowder with desired diameter was obtained and compared with conventional Pechini method (Table 2.10).

However, above method contain several steps of precipitation of Zr-CA complex, drying and thermal decomposition of complex and calcination. Recently, our groups [56–58] developed modified Pechini method with using water-EG-CA-transition metal (TM) medium. First, Zr^{4+} and Y^{3+} salt were dissolved in enough water. Then, 4 mol CA to TM was added to solution and heated in 80 °C for 1 h. During this time, Zr^{4+} and Y^{3+} formed a complex with CA molecules. Then, the solution was heated up to 120–150 °C to form polyester. Due to the presence of water, polyester formation partly converted to initial precursors and

Table 2.10 Size of crystallites and specific surface area of YSZ, obtained from YZr citrates synthesized in EG medium and by the citric acid-based "gel" method (Reprinted with permission from Petrova and Todorovsky [55], Copyright © 2006, Elsevier)

Preparation method	Temperature of heating (°C) and in parenthesis time of hearing (h)	Size of crystallites (nm)	Specific surface area (m^2/g)
Heating of 8YZrCit/EG	450 (1), 750 (4)	25	36
	450 (1), 1000 (4)	60	6
Citric acid-"gel" method (8 mol% Y)	200 (3), 450 (5)	11	64
	200 (3), 750 (5)	24	45
Heating of 15YZrCit/EG[b]	450 (1), 750 (4)	21	–
Pechini (CA/EG = 0.4, 8 mol % Y_2O_3 [7])	400, 700 (6)	6 ± 2	26 ± 3[a]
	400, 1000 (6)	26 ± 5	10 ± 1[a]
Pechini (15 mol% $YO_{1.5}$, [8])	800 (10)	13.5	15.5[a]

[a]Specific surface area determined by BET

[b]15YZrCit/EG-YZr-citrate prepared with 15 mol% Y and isolated from EG medium

oligomers. So, the chain mobility of this polyester was higher as compared with conventional Pechini method. Finally, the solution was heated at 250 °C for 1 h to obtain brownish powder (combusted gel). Finally, the gel analyzed with TG-DTA or TGA-DSC to determine the temperature of organic removal (Fig. 2.16, ordinary calcination temperature was between 550 and 700 °C, 2 h). According to TGA of YSZ gel (Fig. 2.16), there is not any weight loss after 550 °C. So, the gel first, calcinated at this temperature. But, the as-obtained product have mall carbon residue. Thus, the calcination temperature between 600 and 700 °C was selected for obtaining pure YSZ nanopowders. According to SEM images (Fig. 2.17), semi spherical YSZ nanoparticles with average size of 40–60 nm were obtained by

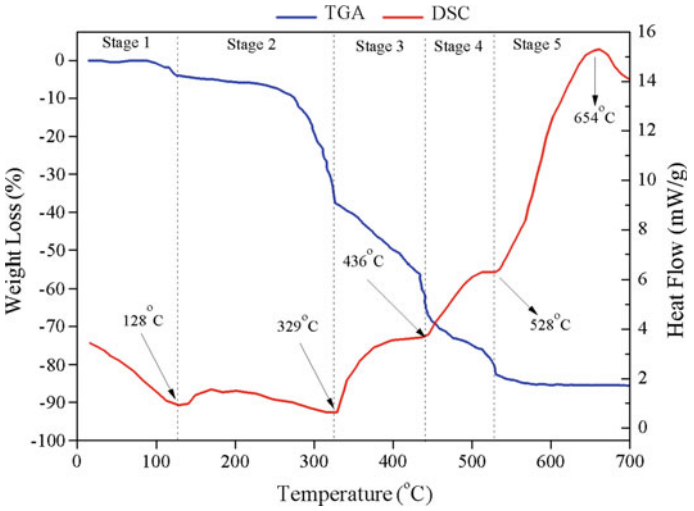

Fig. 2.16 TGA of YSZ precursor produced by modified Pechini method (Reprinted with permission from Hajizadeh-Oghaz et al. [56], Copyright © 2014, Springer)

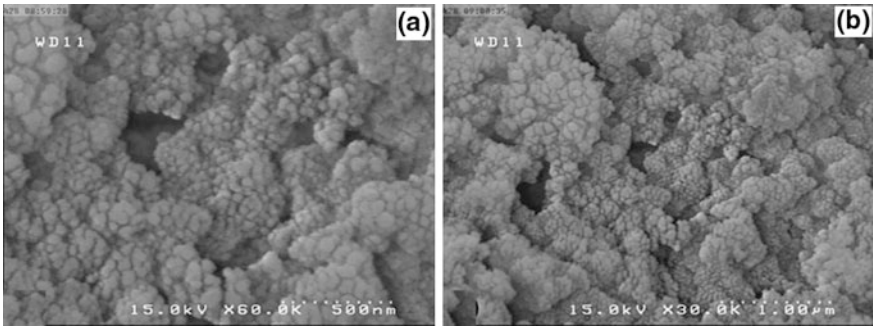

Fig. 2.17 Scanning electron micrograph of large-scale synthesis of 7 YSZ powder at different magnifications: **a** ×60 and **b** ×30 (Reprinted with permission from Hajizadeh-Oghaz et al. [57], Copyright © 2014, Springer)

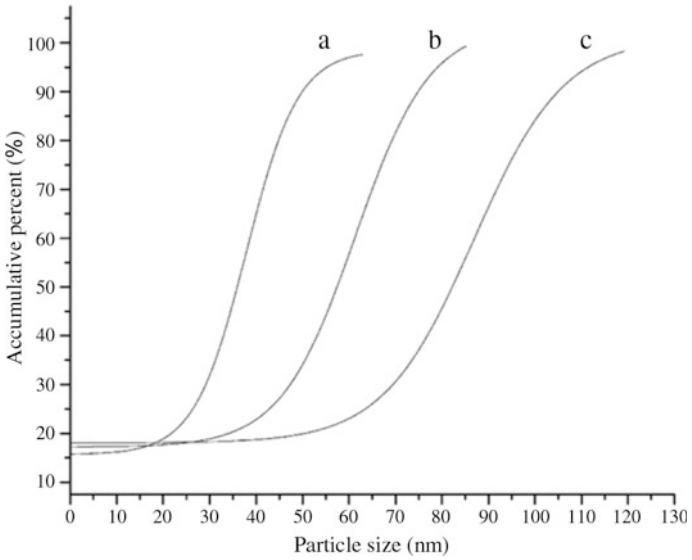

Fig. 2.18 Particle size distribution by accumulative percent diagram at different calcination temperatures: **a** 600 (D50 = 36 nm, D90 = 50 nm), **b** 800 (D50 = 57 nm, D90 = 74 nm) and **c** 1000 °C (D50 = 82 nm, D90 = 104 nm) (Reprinted with permission from Hajizadeh-Oghaz et al. [57], Copyright © 2014, Springer)

modified Pechini method. The Particle size distribution of YSZ nanopowders at different calcination temperatures was illustrated in Fig. 2.18. According to this figure, the D50 was increased from 36 to 82 nm by increasing calcination temperature from 600 to 1000 °C.

In recent years, the green syntheses of some zirconia-based nanoceramic were also investigated using sucrose as polymerization/complexation agent [59, 60]. In a typical, synthesis, 1 mol of $ZrOCl_2 \cdot 8H_2O$ was dissolved in 500 ml (approximately 8 mol) of concentrated nitric acid and the solution was heated on a hot plate to eliminate chloride [60]. About 0.087 mol of yttria was dissolved in the solution to get 8 mol% YSZ composition. Total concentration of zirconium and yttrium in the final Zr–Y composite nitrate solution was 0.75 mol/l. Three moles of sucrose per mole of zirconium and yttrium ion was dissolved in the Zr–Y composite nitrate solution and then heated on a hot plate till a vigorous evolution of gas bubbles were observed due to oxidation reactions. As soon as the oxidation reaction initiate the solution was removed from the hot plate and left to stand for half an hour to ensure completion of the reaction resulting in the formation of a white sol. The sol was dried in an oven at 120 °C to form a black precursor mass. The precursor mass was heated at 600 °C in a muffle furnace to remove the organic material. Calcinated powder was deagglomerated by attrition milling in isopropanol medium for 24 h. Deagglomerated YSZ contain submicron particles with D50 value of 0.5 mm and the particles are aggregates of nanocrystallites of nearly 10 nm size (Fig. 2.19b).

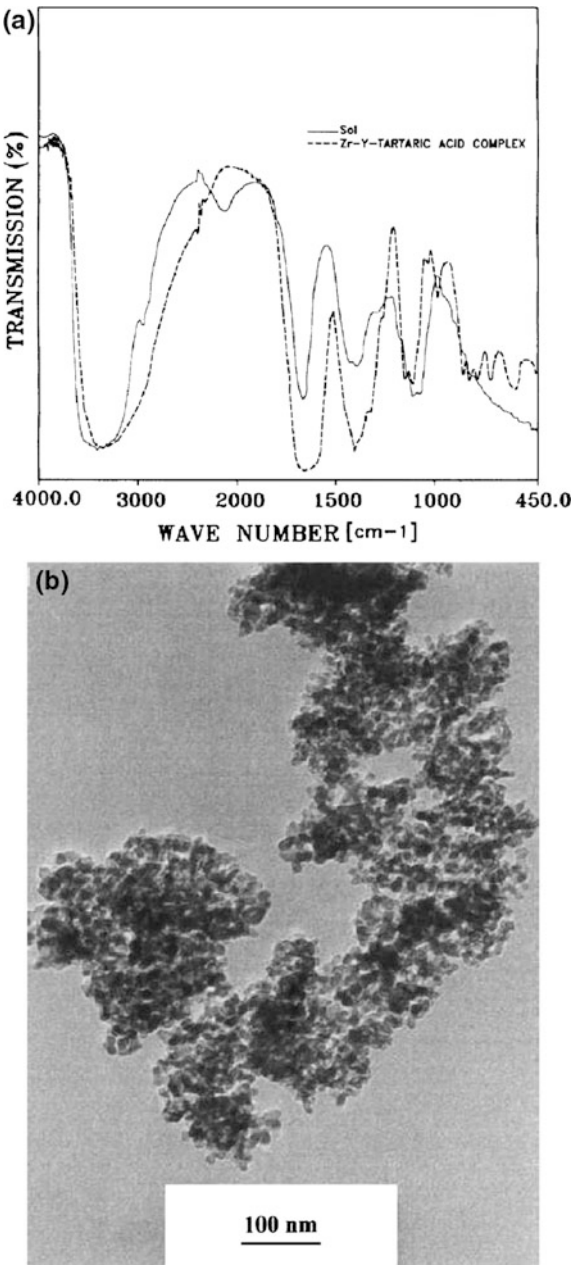

Fig. 2.19 **a** IR spectrum of the sol showing formation of Zr–Y hydroxy carboxylic acid complex. **b** TEM photomicrograph of the YSZ nanopowder (Reprinted with permission from Prabhakaran et al. [60], Copyright © 2007, Elsevier)

It is well known that sucrose undergoes hydrolysis in aqueous acidic medium into glucose and fructose [61]. Nitric acid oxidizes the glucose thus formed into saccharic acid and a small amount of oxalic acid. The fructose produced from sucrose is oxidized to a mixture of trihydroxy glutaric acid, tartaric acid, and

glycolic acid [61]. These hydroxy carboxylic acids forms complex with zirconium and yttrium ions resulted in a white sol. IR spectrum of the sol is shown in Fig. 2.19a. Peak observed at wave numbers 1640 and 1363 cm^{-1} in the IR spectrum are attributed to carboxyl group complexed with the Zr and Y ions. Formation of Zr–Y hydroxyl complexes was further confirmed by synthesizing an analogous complex from Zr–Y composite nitrate solution and analytical reagent grade tartaric acid. A white precipitate obtained by mixing Zr–Y composite nitrate solution and tartaric acid solution showed similar peaks in the IR spectrum as the white sol.

2.2.1.4 Ceria Stabilized Zirconia (ZrO_2–CeO_2 Solid Solution)

Various attempts have been made to improve the TBC properties. As a new candidate TBC material, ceria stabilized zirconia (CSZ) currently looks to be promising. Some investigators have reported that the CSZ coatings have good corrosion resistance and high fracture toughness but also lower thermal conductivity and higher thermal expansion coefficient than YSZ coatings [62, 63]. However, published reports dealing with the nanostructured CSZ TBC systems are very limited and microstructure and properties of plasma-sprayed nanostructured CSZ coating have not been fully understood. The $Ce_{1-x}Zr_xO_2$ phase diagram may be summarized as follows: when $x < 0.15$ $Ce_{1-x}Zr_xO_2$ exhibits cubic, fluorite-type phase; while $x > 0.85$, monoclinic phase. At intermediate compositions, various phases (t, t′, t″, κ, and t^*) have been identified [64].

As previously mentioned, most studies about CSZ nanopowders were focused in cubic phase of CSZ and their applications are in SOFC and three way catalysts (TWCs). Ceria incorporated with zirconia is well known to distinctly enhance oxygen storage capacity (OSC) [64] and improve the thermal stability, surface area, and reducibility of the red-ox or oxygen storage promoters in the TWCs and catalysts properties for H_2 production from fuels and solid state conductors for fuel cells [64]. Figure 2.20 illustrates the recorded heating temperature curves of the electric furnace (coating surface, T0), the TBCs specimen backside (T1) and the substrate specimen backside (T2). As can be seen, ΔT values depend on the ceramic top coating thickness and materials. The ΔT values increased with increasing the coating thickness from 200 to 400 μm. The nanostructured CSZ coatings exhibited higher ΔT values than the conventional YSZ coatings. For 400 μm thick coatings, the ΔT value at 1350 °C of the nanostructured CSZ coating increased by 56.6% compared with that of the conventional YSZ coating. It means that the nanostructured CSZ coating has higher thermal insulation capability than the conventional YSZ coating [63, 64]. In continue, we review the synthesis of CSZ nanopowder with Pechini, coprecipitation and microwave-assisted combustion methods.

Nanocrystalline ceria–zirconia was synthesized using the Pechini process [65]. Zirconium nitrate, $Zr(NO_3)_4{\cdot}2H_2O$, and cerium nitrate $Ce(NO_3)_3{\cdot}6H_2O$ were used as Zr^{4+} and Ce^{3+} sources. Ethylene glycol and citric acid were used as polymerization/complexation agents for the process. Citric acid to transition metal was kept constant

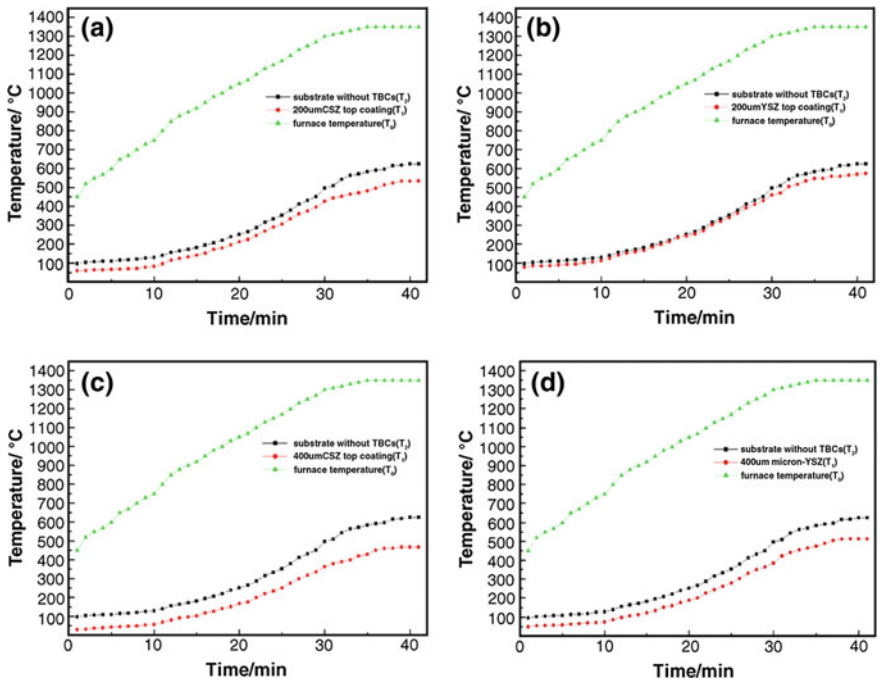

Fig. 2.20 Heating temperature curves of furnace (T0), TBCs specimen backside (T1) and substrate specimen backside (T2). **a** 200 μm thick CSZ coating, **b** 200 μm thick YSZ coating, **c** 400 μm thick CSZ coating and **d** 400 μm thick YSZ coating (Reprinted with permission from Gong et al. [62], Copyright © 2006, Elsevier)

at 1.8 mol. After homogenization of the solution containing cations, ethylene glycol was added in CA/EG ratios of 10, 5, and 2 to promote mixed citrate polymerization by polyesterification reaction. The procedure for the preparation of ceria stabilized zirconia is shown in Fig. 2.21. This gel was then dried at 200 °C in air during a night to remove volatile components and then calcinated at 500–700 °C for 5 h (Heating rate: 5 °C/min) in a static air atmosphere.

XRD result show that by increasing the temperature up to 700 °C a small part of tetragonal phase for the sample by CA/EG = 2 transformed to the monoclinic phase. For the other samples, no such phase transformation appeared. Results showed that with increasing the calcination temperature, the particle size gradually increases and the specific surface area regularly decreases. Simultaneously, the agglomeration of crystallites increases with decreasing the CA/EG ratio (Table 2.11).

The CeO_2 content affected both crystallite size and surface area of the powders, as reported in Table 2.12. As it can be seen, the crystallite size decreases with the increase of the CeO_2 content, i.e., crystallite growth of zirconia is inhibited by the ceria doping in zirconia. Surface areas decreased with a decrease of the CeO_2 content because of the crystallite coarsening. Under the experimental conditions, zirconia doped with 1% of ceria, shows the largest mean crystallite size of 13.1 nm

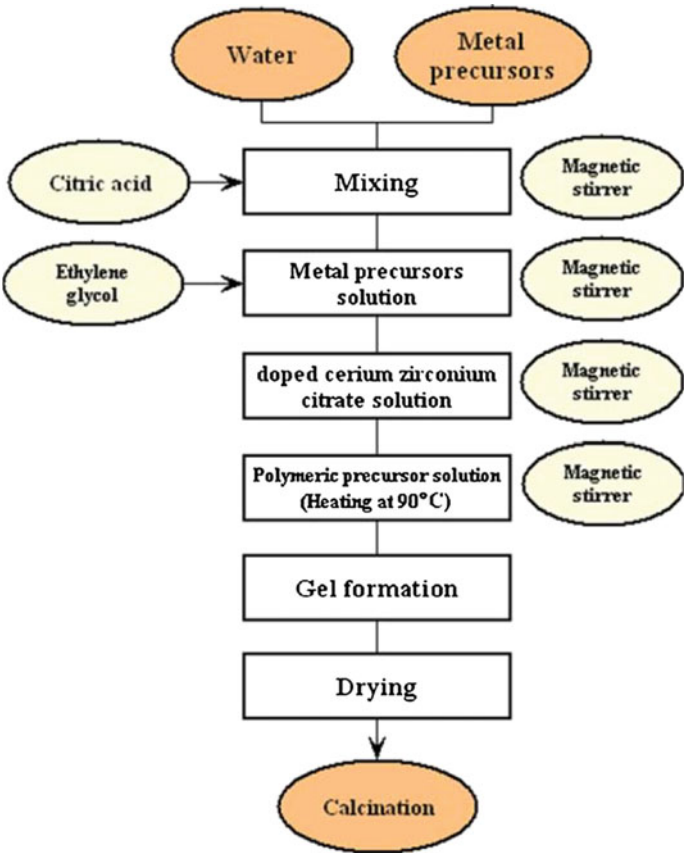

Fig. 2.21 The Pechini diagram for the synthesis of the CYSZ nanopowders (Reprinted with permission from Rezaei [65], Copyright © 2009, Springer)

Table 2.11 Crystallite sizes and specific surface areas of CSZ samples (Reprinted with permission from Rezaei et al. [65], Copyright © 2009, Springer)

Calcination temperature (° C)	Total pore volume ($cm^3\ g^{-1}$)			Average pore size (nm)		
	CA/EG: 10	CA/EG: 5	CA/EG: 2	CA/EG: 10	CA/EG: 5	CA/EG: 2
500	0.0261	0.0266	0.036	4.38	4.56	3.91
600	0.0212	0.0253	0.030	5.45	6.02	6.40
700	0.0145	0.0170	0.0278	9.81	9.03	11.55

and the size is reduced to about 8.1 and 10.3 nm when 5 and 3 mol% CeO_2 are used, respectively. The monoclinic phase occurred only in ZrO_2–1 mol%CeO_2 powder, which presented 16% of the m-phase and 84% of the t-phase. For the other powders, a well-crystallized tetragonal zirconia single phase was obtained.

Table 2.12 Structural properties of the samples with different Ce Contents (Reprinted with permission from Rezaei et al. [65], Copyright © 2009, Springer)

Sample	Crystallite size (nm)	Specilie surface area (m^2 g^{-1})	Tetragonal phase (wt%)
ZrO_2–5% CeO_2	8.1	29.97	100
ZrO_2–3% CeO_2	10.3	25	100
ZrO_2–l% CeO_2	13.1	22.5	84

The TEM analysis (Fig. 2.22) also showed that the calcinated samples containing different content of CeO_2 have similar morphology. As it can be seen, particles are sintered together and most of the particles have a slightly irregular. As mentioned before, the particle sizes in zirconia doped with 5% of ceria are from 7 to 12 nm in

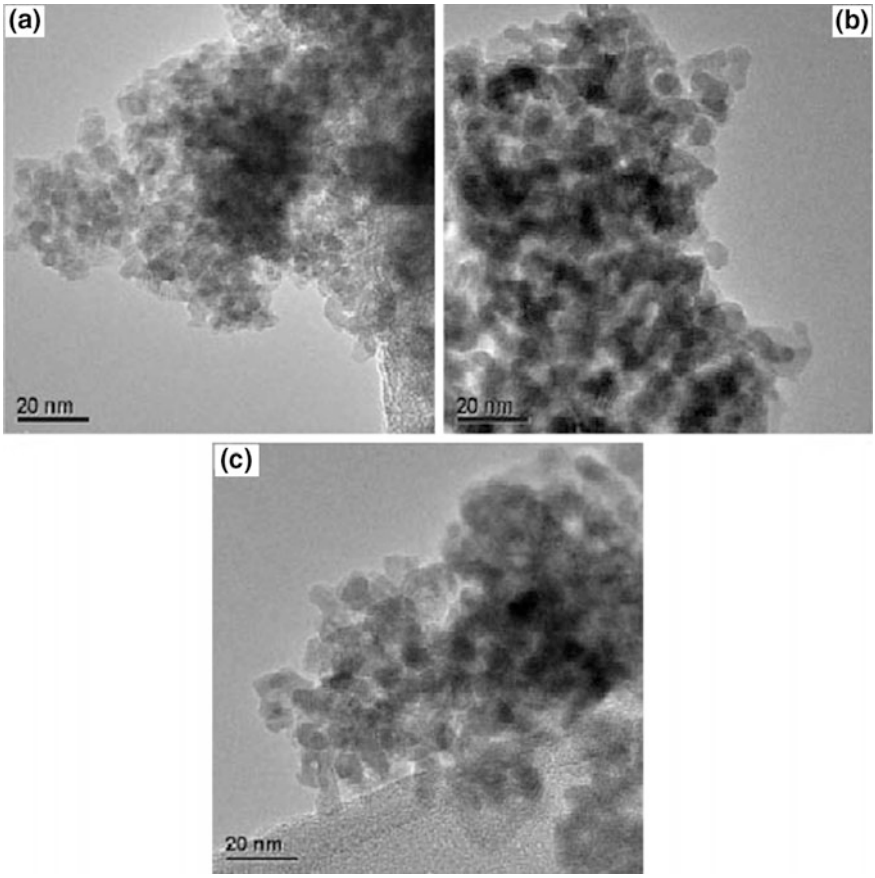

Fig. 2.22 TEM pictures of the zirconia doped with different contents of ceria **a** 5%, **b** 3%, **c** 1% (Reprinted with permission from Rezaei et al. [65], Copyright © 2009, Springer)

diameter, while the particle sizes in zirconia doped with 3 and 1% of ceria are from 8 to 16 nm and 10 to 20 nm, respectively. This suggests that increasing ceria content reduces the surface free energy of zirconia particles and so decreases the crystallite size, which is accompanied by more effective tetragonal phase stabilization.

Nanosized ceria–zirconia solid solution has been synthesized by a microwave-assisted solution combustion synthesis method and compared with that of the ceria–zirconia with the same composition but prepared by a coprecipitation method and calcinated at 773 K [66]. In a typical combustion synthesis of CSZ nanopowders, the required quantities of cerium (III) nitrate and zirconyl (IV) nitrate were dissolved separately in deionized water and mixed together in a Pyrex glass dish. A stoichiometric quantity of solid urea was added to the aforementioned mixture solution and stirred rigorously to obtain a clear solution. The dish containing the reaction mixture was introduced into a modified domestic microwave oven (2.54 GHz, 700 W). Initially, the solution boils and undergoes dehydration followed by decomposition and spontaneous combustion with the evolution of large amounts of gases, including N_2, CO_2, and H_2O along with some traces of NH_3 and NO_2 followed by a spontaneous flame resulting in a light yellow residual mass. The entire process of liquid evaporation, thickening of the solution and combustion in the microwave oven took around 40 min to produce highly voluminous ceria–zirconia powders.

Ceria–zirconia (1:1 mol ratio) solid solution was also prepared by a coprecipitation (CP) method with dilute ammonium hydroxide (0.1 M) [67]. In a typical synthesis, the requisite quantities of ammonium cerium (IV) nitrate and zirconium (IV) nitrate were dissolved separately in deionized water and mixed together. Dilute liquid ammonia solution was added dropwise with vigorous stirring until the precipitation was complete. The obtained precipitate was heated at 333 K for 6 h to facilitate aging. The resulting precipitate was filtered off, washed with deionized water, oven dried at 383 K for 16 h, and calcinated at 773 K for 5 h in air atmosphere.

XRD studies (Fig. 2.23) revealed formation of monophasic $Ce_{0.5}Zr_{0.5}O_2$ solid solution in the MW sample and $Ce_{0.75}Zr_{0.25}O_2$ solid solution in the CP sample. The

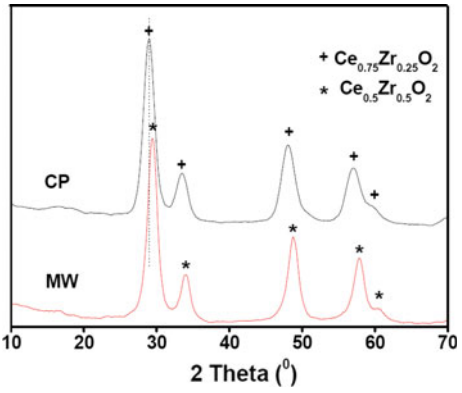

Fig. 2.23 X-ray powder diffraction patterns of ceria–zirconia solid solutions (*MW* prepared by microwave method; *CP* prepared by coprecipitation method) (Reprinted with permission from Reddy et al. [66], Copyright © 2009, Bentham)

observed more zirconium incorporation in the MW sample is primarily due to progressive increase of Zr^{4+} content into the ceria unit cell at higher preparation temperatures. Within the detection limits of XRD technique there was no evidence about the presence of t-ZrO_2 or m-ZrO_2 phase. Figure 2.24 shows the Raman spectra of the two samples investigated in the present study. As shown in Fig. 2.24, both samples show a strong band at 470 or 468 cm^{-1} and a less prominent broad band at 600 cm^{-1}. The band at 468 cm^{-1} is due to the F_{2g} vibration of the fluorite-type lattice [68]. It can be viewed as a symmetric breathing mode of the oxygen atoms around the cerium ions [69]. The slight shift in the Raman frequency to higher wave numbers in case of MW sample could be due to incorporation of more zirconium into the ceria lattice when compared to the CP sample as evidenced by XRD results. As presented in Fig. 2.24, the Raman band at 470 cm^{-1} is intense in the case of MW sample. It is known from the literature that the intensity of Raman band depends on several factors including the grain size and morphology [69]. Therefore, it is quite obvious that sintering of samples at higher preparation temperatures increases the intensity of the F_{2g} band. It is also known that sintering of samples under high-temperature conditions can lead to the formation of oxygen vacancies, which perturb the local M–O bond symmetry leading to the relaxation of symmetry selection rules. The presence of a weak and less prominent broad band near 600 cm^{-1} can be attributed to a nondegenerate longitudinal optical (LO) mode of ceria which arises due to relaxation of symmetry rules, which in turn linked to oxygen vacancies in the ceria lattice [68, 69]. In particular, the substitution of zirconium into the ceria lattice with an increase in temperature gives rise to oxygen vacancies, which are responsible for the emergence of this band [69]. This band is

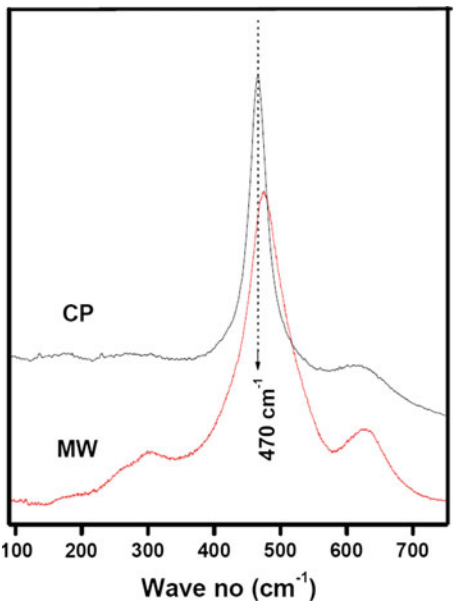

Fig. 2.24 Raman spectra of ceria–zirconia solid solutions (*MW* prepared by microwave method; *CP* prepared by coprecipitation method) (Reprinted with permission from Reddy et al. [66], Copyright © 2009, Bentham)

Table 2.13 Crystallite Size, Cell Parameter, BET Surface Area and Oxygen Storage Capacity Values of Ceria–Zirconia Solid Solutions Synthesized by Microwave Combustion (MW) and Coprecipitation (CP) Method (Reprinted with permission from Reddy et al. [66], Copyright © 2009, Bentham)

Sample	Crystallite size (nm)	Cell parameter (Å)	Surface area (m^2/g)	OSC μ moles O_2/g simple
MW	12.7	5.30	56	278
CP	4.7	5.35	84	211

more intense in the case of MW sample, which indicates incorporation of more zirconium into the ceria lattice and formation of more oxygen vacancies in MW sample. There is also another band at 305 cm^{-1} in MW sample. This can be attributed to displacement of oxygen atoms from their ideal fluorite lattice positions [68]. As per the literature reports, this band further reveals the presence of t′ phase, which could not be identified by XRD. The presence of this band and more intense band at 605 cm^{-1} has also clearly reflected in its enhanced oxygen vacancy concentration as determined by the oxygen storage/release capacity (OSC) measurements (Table 2.13).

The TEM image revealed nanometer sized particles with broad particle size distribution (10–40 nm). The broad particle size distribution could be due to the preparation method adopted. During the preparation, the precursors were exposed to higher temperatures for a short period of time, which obviously leads to particles with different sizes. The digital diffraction pattern (DDP) corresponding to an individual particle of the image is shown in inset of Fig. 2.25. The inter planar spacing values of 3.0, 2.6, and 3.0 Å were measured from the DDP and could be respectively assigned to (111), (200), and (1-1-1) family planes of the cubic structure In summary, it can be concluded that synthesis of nanosized ceria–zirconia solid solutions by microwave-assisted method is a cost effective technique in comparison to the conventional coprecipitation route for making ceria stabilized zirconia nanopowders.

2.2.1.5 Ceria, Yttria Co-stabilized Zirconia (CYSZ)

As mentioned before, considerable interest has turned to replacing yttria with ceria as the stabilizing oxide added to zirconia ceramics and coatings. It has been shown that ceria stabilized zirconia (CSZ) ceramics can attain significantly greater toughness and superior thermal shock resistance to those based on the YSZ counterpart.

Despite these advantages there is also a weakness for CSZ material as a thermal barrier coating. Independent erosion tests have been indicated that erosion resistance of CSZ coatings was significantly lower to that of the YSZ systems. In order to solve this problem, use a mixture of ceria–yttria stabilizers could be a compromise solution that would promise good properties of both stabilizers to provide

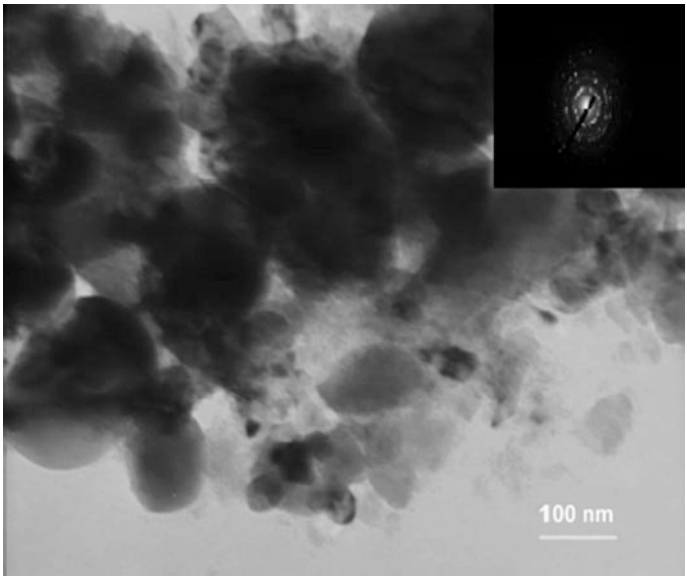

Fig. 2.25 TEM image of ceria–zirconia solid solution prepared by microwave-assisted combustion synthesis method (Reprinted with permission from Reddy et al. [66], Copyright © 2009, Bentham)

possible shared advantages. It has been indicated that the CYSZ coating was superior to the YSZ coating due to its phase stability at high temperature, improved thermal insulation, higher CTE, good corrosion, and thermal shock resistance.

Tetragonal CYSZ nanocrystals with a size range from 10 to 100 nm have been synthesized by various methods: Coprecipitation, Hydrothermal, spray drying, and sol–gel [38, 72–74]. However, to the best of our knowledge, very few studies have dealt with the synthesizing CYSZ nanoparticles for thermal barrier coating applications by Pechini sol–gel route [70, 71]. Our groups, was synthesized CYSZ nanoparticles for TBC applications by Pechini method [75, 76].

In a typical synthesis of ZrO_2–25 wt% CeO_2–2.5 wt% Y_2O_3 nanoparticles, 9.80 g$ZrOCl_2{\cdot}8H_2O$, 3.02 g$Ce(NO_3)_3{\cdot}6H_2O$,0.42g$Y(NO_3)_3{\cdot}6H_2O$, and 7.27 g anhydrous citric acid were dissolved into 100 ml of double distilled water, respectively. The prepared solutions were well mixed in a glass beaker using a magnetic stirrer and hot plate followed by the addition of 2.13ml ethylene glycol (CA:EG:1 mol ratio) with continuous stirring to convert them to stable complexes that was allowed to settle down at the temperatures of 100, 200, and 300 °C, each for 2 h which yielded a transparent gel. Finally, the gel was calcinated at higher temperatures (400–1100 °C) to obtain Nanocrystalline CYSZ with different particle sizes.

X-ray diffraction pattern of the precursor gel shows that the precursors are amorphous (Fig. 2.26).The precursor gel was calcinated at various temperatures to produce CYSZ powders. At 400 °C, the strongest characteristic peaks of ZrO_2 tetragonal phase appear with weak intensity. XRD analysis shows that the precursor

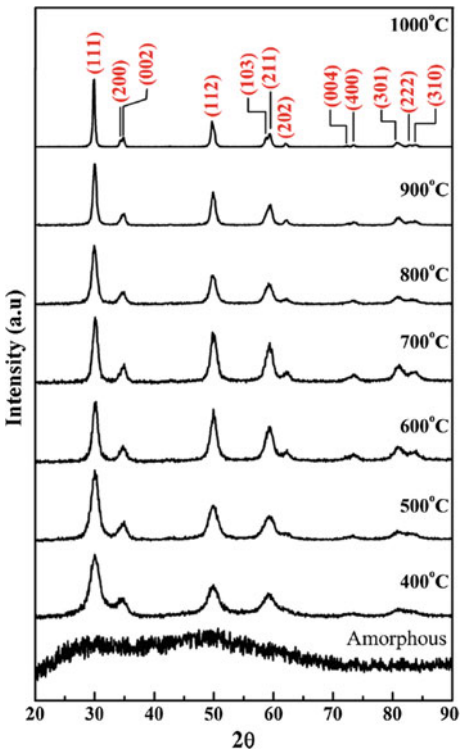

Fig. 2.26 XRD patterns of the CYSZ powders calcinated at different temperatures for 2 h (Reprinted with permission from Hajizadeh-Oghaz et al. [76], Copyright © 2015, Springer)

transforms completely to the tetragonal zirconia at around 600 °C, and no other phases can be detected (Fig. 2.26). By increasing the calcination temperature, the peaks became more intense and sharper and the full width at half maximum (FWHM) of diffraction pattern became narrower; indicate the improved crystallinity and crystallite growth of the CYSZ nanopowders, respectively.

Our groups show that [75] the degree of the chelation of metallic ions by carboxylic groups is an important factor informing nanosize CYSZ particles and it can be controlled by adjusting the pH alue of the starting solution. Decreasing pH value can increase the degree of the chelation of metallic ions in the solution. The higher degree of the chelation of metallic ions by –COOH results in the higher uniformity of Zr^{4+}, Ce^{3+}, and Y^{3+} distributed in the obtained esters and more completion of reactions to form CYSZ nanoparticles.

Furthermore, a representative TEM image of CYSZ powders synthesized at different pH values are shown in Fig. 2.27, where the well-dispersive semispherical CYSZ nanoparticles can be observed at acidic pH. Most of the CYSZ nanoparticles had quasi-spherical morphologies and no highly aggregated particles could be observed. The diameter of spherical nanocrystals was observed to be about 41.5 nm.

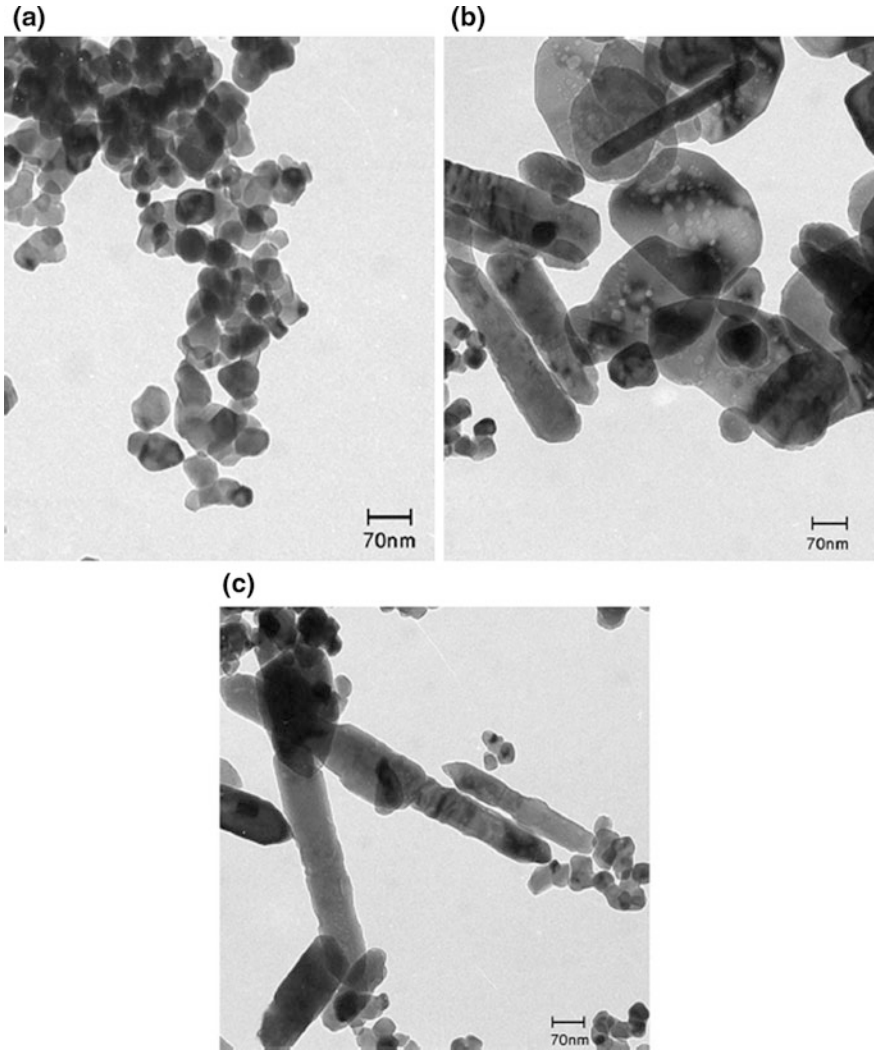

Fig. 2.27 TEM photograph of the CYSZ powder prepared by Pechini route at different pH values **a** pH = 1, **b** pH = 7, and **c** pH = 12 (Reprinted with permission from Hajizadeh-Oghaz et al. [75], Copyright © 2015, Springer)

In alkali pH, the presence of ammonia barricades the formation of bridged bonds with the citric acid, as reflected in the morphologic characteristics of the powders. Furthermore, higher pH possibly could favor $Zr(NH_3)_n^{2+}$, $Ce(NH_3)_n^{2+}$, and $Y(NH_3)_n^{2+}$complex formation; therefore zirconium, cerium, and yttrium ions would not be trapped in the polymer at high pH values [77]. On the other hand, the interaction of citric acid and ethylene glycol, being an esterification reaction, could be considerably slowed down without acidic catalysis at high pH values. The major

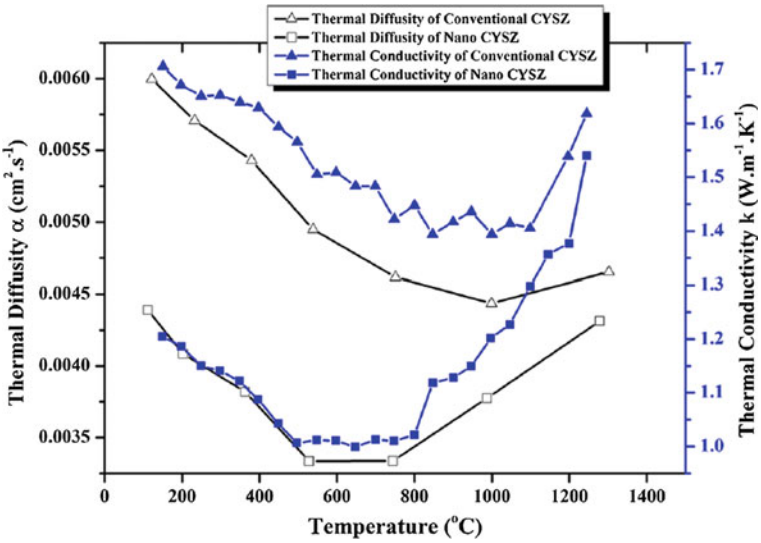

Fig. 2.28 Thermal diffusivity a(T) and thermal conductivity k(T) results of the conventional [77] and nanostructured CYSZ [76] (Reprinted with permission from Mazaki et al. [77], Copyright © 1995, Elsevier)

effect of pH value on the Pechini method is that it can destroy esterification between citric acid and ethylene glycol, thereby affecting Zr, Ce, and Y species and the formation of the mixed-metal CA complex [72–74, 78, 79].

Figure 2.28 shows the variation in thermal diffusivity and thermal conductivity values of conventional CYSZ [77] and nano-CYSZ from ambient temperature to 1300 °C of the fully dense CYSZ ceramic material. For both specimens the thermal diffusivity and conductivity particularly that measured at low temperatures, decreases with temperature increasing, while the measured high-temperature conductivity is practically increased by temperature increasing (Fig. 2.28).

In most ceramic materials, the scattering of lattice vibrations becomes more pronounced with rising temperature; hence, the thermal conductivity of CYSZ normally reduces with increasing temperature, at least at relatively low temperatures. As Fig. 2.28 indicates, the conductivity begins to increase at higher temperatures; this can be explained by two different heat transfer mechanisms that dominate at deferent temperatures. At low temperatures the heat transfer is mainly based on the phonon conductivity which is affected strongly by the microstructural features like porosity and microcracks. At high temperatures above 1200 °C, in addition to phonon conductivity, the photon (radiation) conductivity takes place. Furthermore, at high temperatures, radiative heat transfer through the material in the course of the thermal diffusivity measurement might lead to this apparent increase [80].

It can be seen that both thermal diffusivity and thermal conductivity of nanostructured CYSZ is lower than conventional CYSZ reported in the literature [81].

The phonons mean path can be given by.

$$\frac{1}{l} = \frac{1}{l_i} + \frac{1}{l_p} + \frac{1}{l_b}, \tag{2.2}$$

where phonon mean path due to inherent conductivity, point defect scattering, and grain-boundary scattering are l_i, l_p, and l_b, respectively. In nanostructured CYSZ, grain-boundary scattering also has a significant effect on phonon mean path, which can be described by [82, 83].

$$\frac{1}{l_b} = \frac{T\gamma^2}{20T_m\alpha} \tag{2.3}$$

where T_m is the absolute melting temperature, α is the lattice constant, and γ is the Gruneisen constant. Using the Eq. 2.3, grain-boundary scattering calculated for single crystal of CYSZ as 23 nm.

The grain size of CYSZ is 20–30 nm, which is comparable to phonon mean free path owing to grain-boundary scattering. The small grain size leads in lower thermal conductivity owing boundary thermal resistance endorsed by phonon scattering at grain boundaries [84, 85].

Furthermore, the as-synthesized CYSZ nanopowders were granulated with spray dryer and plasma sprayed on Ni-based supperalloy. The fractured cross-section of the as-sprayed coating is illustrated in Fig. 2.29. It showed a usual splat-like microstructure composed of almost parallel overlapping lamellae, divided by splat boundaries and surrounded by a network of voids and microcracks. The width of the lamellae was approximately between 1 and 5 μm. The vertical microcracks improved high-temperature strain tolerance, whereas the splat boundaries usually affected thermal conductivity and heat transfer. The former was initiated from the splat boundaries as a result of stress relaxation throughout rapid cooling to ambient temperature, while the latter originated throughout coating build-up, as a result of the weak bonding between the deposited splats, depending on the speed of the impact of the molten droplets and their solidification rate. Inadequate filling throughout coating build-up meant that the emerging globular voids played a substantial role in determining the final mechanical and thermal properties [86–88].

The hot corrosion resistance of this nanostructured TBC was also investigated in the presence of 45 wt% Na_2SO_4 + 55 wt% V_2O_5 as the corrosive molten salts. Previous research show that more degradation-resistant of micro-sized CYSZ TBC as compared with YSZ coating was due to more acidic nature of CeO_2 than Y_2O_3 in order to resist reaction with acidic $NaVO_3$ and V_2O_5 molten salt [90–95]. However, our result show nanostructured CYSZ coating show interior hot corrosion resistance than micro-sized CYSZ and YSZ TBCs [89]. The nanolocal in nanostructured CYSZ coating, with considerably inferior pinholes and microcracks, prohibited the further diffusion of molten salts into the deeper layers of the CYSZ coating through diffusional resistance in a nonporous media mechanism; therefore, the quantity of hot corrosion products, including monoclinic ZrO_2, YVO_4, $CeVO_4$, and

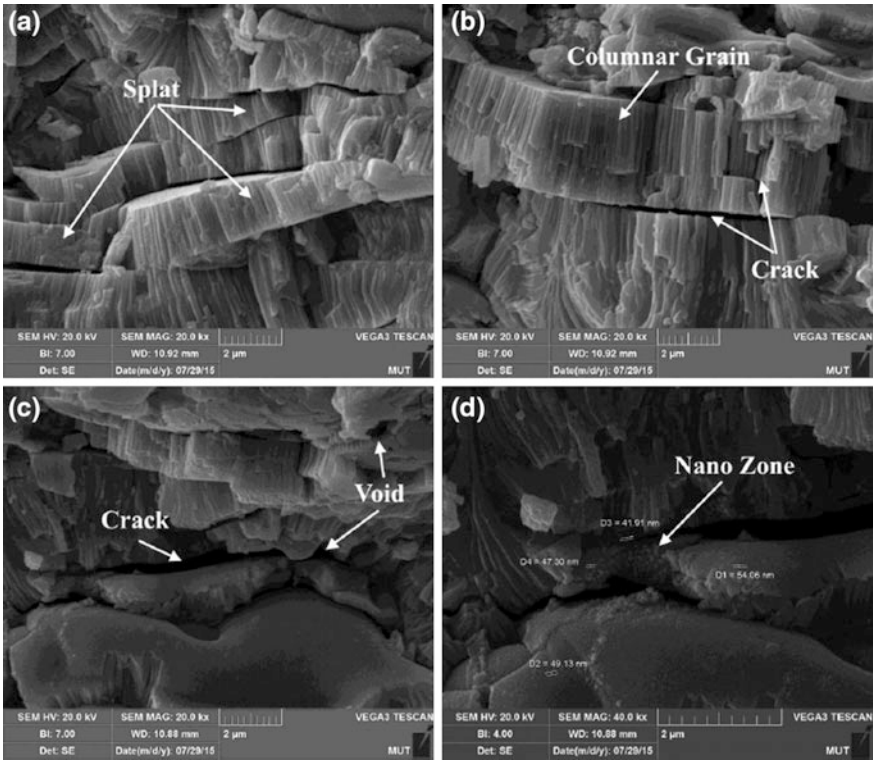

Fig. 2.29 Scanning electron microscopy micrographs of the fractured cross-section of the plasma-sprayed nanostructured coating, showing splat columnar grains (**a**, **b**) and non-molten nanoparticles in the interior of the coating at different magnifications (**c**, **d**) (Reprinted with permission from Hajizadeh-Oghaz et al. [89], Copyright © 2016, Elsevier)

$Ce_{0.75}O_2Zr_{0.25}$ crystals, was probably negligible at the interior depth of the topcoat, even after hot corrosion for 300 h [89]. Moreover, the other reason for interior hot corrosion resistance of nano-CYSZ coating is due to more adaptive strain ability of nanostructured TBCs as compared with microstructured one [86].

Furthermore, our group evaluated thermal insulation capacity of nanostructured CYSZ and conventional YSZ TBCs with the thickness of 300 µm. The first value was to be 150 °C and the latter was to be 130 °C (110 °C) [96]. This result confirms the interior insulation properties of nano-CYSZ as compared with conventional YSZ TBCs.

2.2.1.6 Scandia, Yttria Co-stabilized Zirconia (ScYSZ)

Recently, codoping zirconia with Al_2O_3, Sc_2O_3, Y_2O_3, Bi_2O_3, Sm_2O_3, Yb_2O_3, CeO_2, etc., has attracted researchers to improve thermal and electrical properties of this ceramic.

Yttria stabilized zirconia (YSZ) had a phase stability up to 1200 °C, but upon doping YSZ with scandium oxide (scandia, at specific content), the thermal stability of this ceramic was improved up to 1400 °C. Increasing the thermal stability of zirconia ceramics can have high potential applications in improving the efficiency and performance of engine [90–95]. The Y_2O_3–Sc_2O_3–ZrO_2 system with 8–12 mol % stabilizing content has been studied by J.T.S. Irvine groups [97]. They showed that a higher conductivity could be obtained with ScYSZ than YSZ and ScSZ (scandia stabilized zirconia). Furthermore, alternative materials to YSZ for improving TBCs life time are being sought. One approach was taken by Jones [98] who sought to combine the stabilizing efficiency of Y_2O_3 with the vanadate-corrosion resistance of Sc_2O_3. R. L Jones showed that the most effective stabilizer composition for ultra high-temperature TBCs was probably near 90–95% Sc_2O_3 and 10–5% Y_2O_3 [90–95]. Jang [99] reported that the amount of tetragonal phase was increased by codoping with scandia and yttria. This was due to the lower stabilization of zirconia by scandia [99, 100]. The strength of the codoped material was about 10% higher than that of the reference materials (YSZ and ScSZ). It was also reported that a higher fracture toughness of the codoped material was obtained, as compared to the reference material, in accordance with the higher tetragonal phase content and the resulting enhanced transformation toughening [90–95].

The rare earth stabilized zirconia (RESZ) nanostructures have received an increasing interest in recent years. The traditional method in preparing multicomponent zirconium oxides involves initial mechanical mixing of oxide powders and then high-temperature calcination to homogenize the metal oxide–zirconia composition via solid-state reactions. Serious problems in processing zirconia-based solid solutions resulted from these high-temperature techniques, including uncontrolled grain growth, deep segregation of dopant, and possible loss of stoichiometry due to the volatilization of a reactant at high temperatures. For this reason, based on wet chemical routes, several increasingly important alternatives make the synthesis of zirconia-based solid solutions at mild temperatures possible. In order to prepare multidopant zirconia nanocrystals such as ScSZ (Sc_2O_3 doped ZrO_2), YSZ (Y_2O_3 doped ZrO_2), and ScYSZ, several methods, such as coprecipitation, alkoxide, and the acetic acid-based gel, hydrothermal process and gel combustion process (such as citrate–nitrate and glycine–nitrate route) are well-known [100–106]. Of all the above processes, modified sol–gel preparation method (i.e., Pechini method) shows some advantages due to its relatively low cost compared to alkoxide-based sol–gel methods, and better control of stoichiometry [38, 106–114].

The ScYSZ nanoparticles were prepared by new modified Pechini method [115–117]. In this approach, $ZrO(NO_3)_2{\cdot}H_2O$, $Sc(NO_3)_3{\cdot}H_2O$, $Y(NO_3)_3{\cdot}6H_2O$, citric acid mono hydrate, and ethylene glycol mono butyl ether were used as the source of Zr^{4+}, Sc^{3+}, Y^{3+}, the chelating and solvent agent, respectively. To the best of our knowledge, this is the first report of synthesizing the ScYSZ nanoparticles using modified Pechini method. In this new approach, for controlling agglomeration degree of nanoparticles, the solvent agent (EG) was replaced with ethylene glycol mono butyl ether (EGM).

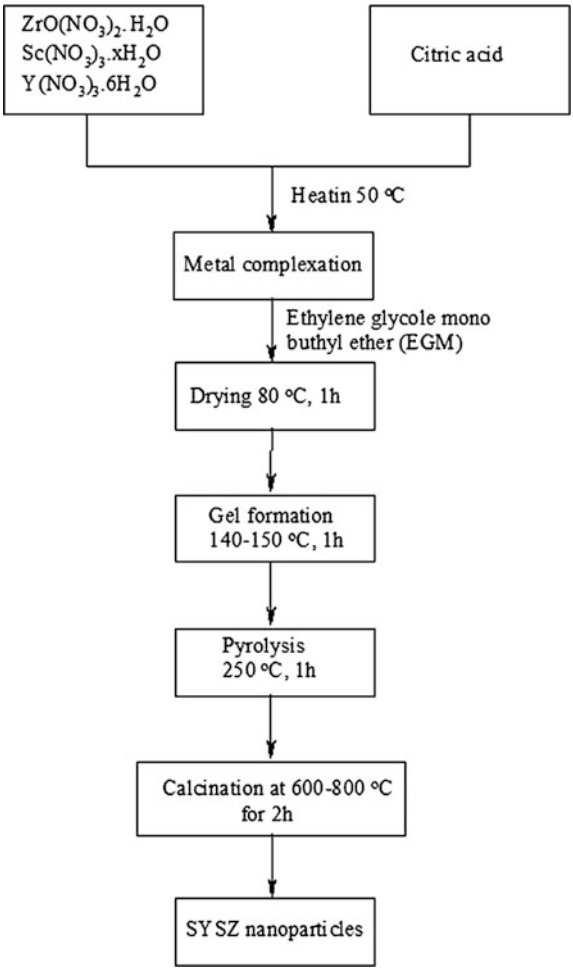

Fig. 2.30 Schematic of production of ScYSZ nanoparticles via modified Pechini method [116]

In a typical experiment [116], 93 mmol $ZrO(NO_3)_2{\cdot}H_2O$, 3.5 mmol $Sc(NO_3)_3{\cdot}H_2O$, 0.5 mmol $Y(NO_3)_3{\cdot}6H_2O$, and citric acid were dissolved in deionized water, and appropriated (EGM: CA: Zr = 4:1:1) amounts of EGM were then added to form a sol at 50 °C for 1 h. A white solution was obtained and further heated at 80 °C for 1 h to remove excess water. During continued heating at 140–150 °C for 1 h, the solution became more and more viscous and finally became a xerogel. To complete drying, xerogel was placed at 250 °C for 1 h. The result powder is a precursor. The precursor was heat treated at 600–800 °C, in the furnace and then cooled it to reach room temperature. The whole process is summarized in Fig. 2.30.

Figure 2.31 shows the results of thermogravimetric (TGA) and differential thermal analysis (DTA) of ScYSZ precursor (the dark gel). Figure 2.31a shows

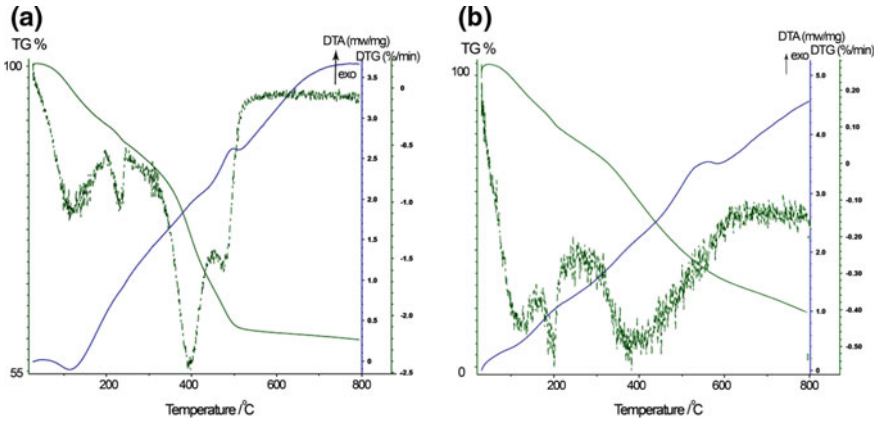

Fig. 2.31 TG/DTA curve of ScYSZ gel precursor at different EGM:CA ratios **a** 1.2:1 and **b** 4:1 (Reprinted with permission from Loghman-Estarki et al. [116], Copyright © 2013, Elsevier)

thermal behavior of the gel prepared with EGM:CA mole ratio = 1.2:1. The total weight loss was about 48% of the total precursor mass and occurred in four steps. The first weight loss occurs at about 115 °C, corresponding to the first endothermic peak shown by DTA curve, is due to the dehydration of the precursor. The second small weight loss shown by TGA curve around 200 °C can be ascribed to the evaporation of any excess ethylene glycol mono butyl ether (b.p. 199 °C) in the gel [107, 108]. The third weight loss step occurs at the temperature range 300–481 °C. The weight loss at 300–481 °C was attributed to the carbonization or bond breaking of organic moieties in precursors together with the evolution of great amounts of gases such as CO_2. The exothermic peak around 591 °C in the DTA curve can be primarily associated with the crystallization of amorphous gel and this reaction led to the occurrence of the fourth weight loss found in the TGA curve. Upon increasing EGM:CA mole ratio to 4:1, the total weight loss was about 70% of the total precursor mass (Fig. 2.31b) which in good agreement with the calculated amount of water, EGM and CA molecules (calc. 73%). According to the DTA curve (Fig. 2.31b), with increasing EGM:CA mole ratio, the released heat increased from 2.5 to 3.3 mw/mg, resulting more weight loss in TGA curve (Fig. 2.31b) in comparison to Fig. 2.31a. The strong exothermic peak around 591 °C in the DTA curve (Fig. 2.31b) can be attributed to decomposition into oxides and this reaction occurred between 500 and 600 °C [107, 108]. This is confirmed by calcination experiments because the powder calcinated at temperature greater than 600 °C became white in color. Based on TGA analysis (Fig. 2.31), initial calcination temperature was selected at 600 °C, but when the sample was calcinated at 600 °C; the resulting coaly powder showing there still remained small carbon on the sample (Fig. 2.31b). So, according the TGA, the optimized temperature was selected to be 700 °C for 2 h.

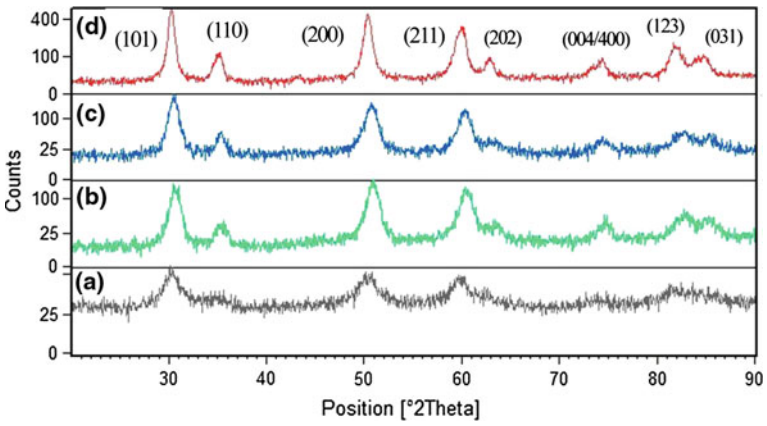

Fig. 2.32 XRD patterns of ScYSZ nanocrystals synthesized at different condition **a** EGM: Zr^{4+} = CA:Zr^{4+} = 4:1, 600 °C/2 h. **b** EGM:Zr^{4+} = CA:Zr^{4+} = 1.2:1, 700 °C/2 h, **c** EGM: Zr^{4+} = CA:Zr^{4+} = 1.2:1, 700 °C/2 h. **d** YSZ, EG:Zr^{4+} = CA:Zr^{4+} = 4:1, 800 °C/2 h, prepared by conventional Pechni method (Reprinted with permission from Loghman-Estarki et al. [117], Copyright © 2013, Royal Sociey of Chemistry)

Figure 2.32 shows XRD patterns of the products at different conditions. Ac can be seen in Fig. 2.32a, when the sample was calcinated at 600 °C/2 h, the crystallinity of the products was not completed. Upon increasing the calcination temperatures to 700 °C/2 h, the crystallinity of the products was improved (Fig. 2.32b–d). The XRD patterns is very close to the values in powder diffraction card (JSPDS No. 01-071-1284, space group P 4_2/nmc) and no impurity, such as Y_2O_3, Sc_2O_3, etc., was found in X-ray diffraction pattern. These results show that Y_2O_3 and Sc_2O_3 were successfully doped in zirconia lattice by present modified Pechini method and formed solid solution. The calculated value of a and c parameter was equal to 0.35984 nm and 0.50105 nm, respectively. From $c/a\sqrt{2}$ calculation, it was found t′ phase of ScYSZ was obtained. The distinguishing peak for t phase occurred at $2\theta = 30.5°$ for (101) reflection, and the respective peaks for monoclinic (m-phase) occurred at $2\theta = 28.4°$ and $2\theta = 31.6°$ for (111) and (−111) reflections. So, the presence of m-phase of zirconia can be ruled out based on the absence of characteristic peaks of m-phase in all XRD patterns of as-prepared sample. Srinivasan et al. [118] reported that the tetragonal structure can be distinguished from the cubic structure in the presence the characteristic splitting of the tetragonal phase, such as (002)/(200), (113)/(311), (004)/(400), and (006)/(600), whereas the cubic phase exhibits only single peaks at all of these positions. For all samples calcinated at 700 °C/2 h, splitting has been relatively seen in the 2θ region of 70–78° for (004)/(400) planes.

It should be noted that all of above samples was prepared at Sc_2O_3:Y_2O_3 mol ratios equals to 3.5:0.5 percent. As mentioned before, the t′ phase for ScYSZ was obtained at a specific amount of stabilizer agent. To this end, the amount of Sc_2O_3: Y_2O_3 mol ratios were changed and the ScYSZ nanopowders were sintered at 1400 °

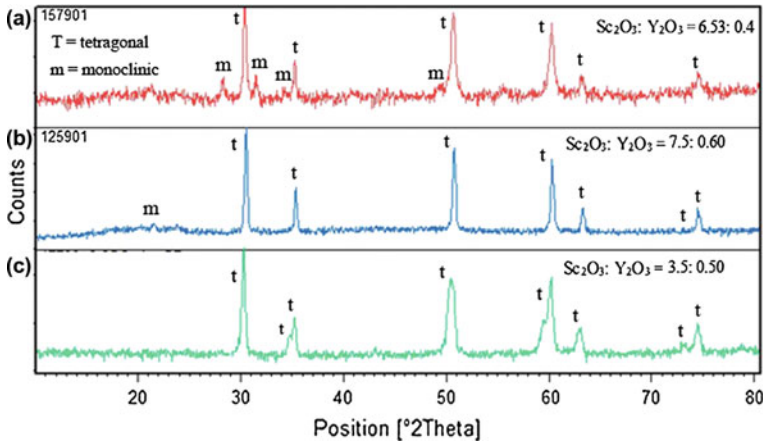

Fig. 2.33 XRD patterns of sintered ScYSZ nanocrystals synthesized at different Sc_2O_3:Y_2O_3 mol ratio percent **a** 6.53:0.40 **b** 7.5:0.6 **c** 3.5:0.50 (Reprinted with permission from Loghman-Estarki et al. [117], Copyright © 2013, Royal Sociey of Chemistry)

C. The selection temperature reason was due to this fact that in order to clearly observe the tetragonal splitting in the entire 2θ region in yttria-containing zirconia ceramics, the material must be sintered above 1100 °C. Below 1100 °C, the 2θ angle, at which tetragonal reflections occur, becomes a function of a number of parameters, such as the change in composition, different thermal treatments, and variation of lattice parameters with a change in composition, etc. Figure 2.33 show XRD patterns of sintered ScYSZ samples at 1400 °C with different Sc_2O_3:Y_2O_3 mol ratios. As can be seen, only at Sc_2O_3:Y_2O_3 = 3.5:0.5 mol%, t′ phase was obtained. This tetragonality is within the range of c/a $\sqrt{2}$ = 1.0025–1.0075 as cited by other researchers [7, 93, 94]. Thus, the phase stability of ScYSZ samples up to 1400 °C and splitting of (002)/(200) at 2theta = 35–36° confirms that a non-transformable tetragonal phase is produced by 4 mol% Sc_2O_3,Y_2O_3 doped ZrO_2.

TEM and selected area electron diffraction (SAED) characterization confirmed that the Sc_2O_3:Y_2O_3 = 6.53:0.4 sample have mixture of monoclinic (m-ZrO_2) and tetragonal phase (t-ZrO_2) of zirconia (Fig. 2.34a). The HRTEM images show well resolved lattice fringes indicating the single crystalline nature and high crystallinity of the synthesized product. The lattice fringes are of equidistance, without any lattice mismatch. These fringes are separated by 0.315 nm, which agrees well with the interplanar spacing corresponding to the (−111) plane of m-ZrO_2 [117]. The clear spots in the SAED pattern (Fig. 2.34b) are indexed to (−111) and (111) planes, which can be attributed to the m-ZrO_2. In comparison to this sample, the ScYSZ nanocrystals, synthesized with Sc_2O_3:Y_2O_3 mol ratio equal to 3.5:0.5, show dissimilar HRTEM images and SAED patterns. The reflections in the SAED pattern and lattice fringes correspond to the lattice planes of bulk t-ScYSZ, hence suggesting the high purity and crystallinity of as-synthesized product. The HRTEM

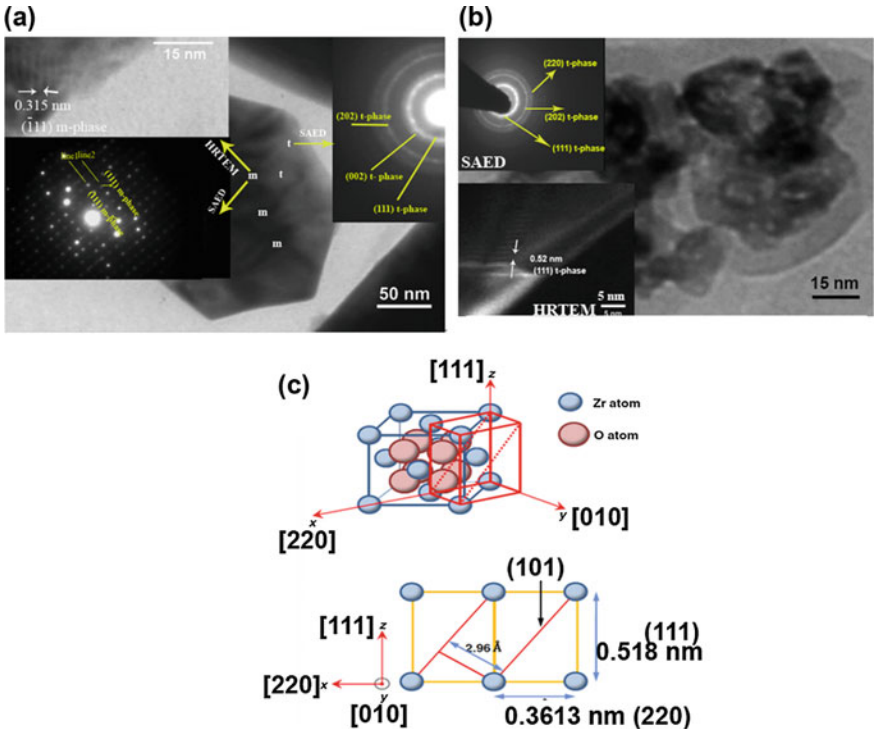

Fig. 2.34 **a**, **b** HRTEM and corresponding SAED analysis of SCYSZ prepared at different Sc_2O_3: Y_2O_3 mol ratio percent **a** 6.53:0.40 **b** 3.5:0.50, sintered at 1400 °C/24 h **c** a schematic illustration of the tetragonal structure and atom configuration (*inset* m = monoclinic and t = tetragonal phase) (Reprinted with permission from Loghman-Estarki et al. [117], Copyright © 2013, Royal Sociey of Chemistry)

of pure t-ScYSZ image show clear lattice fringes as shown in of Fig. 2.34b. A tetragonal atomic arrangement is regularly observed with the incident electron beam aligned along the [111] zone axis of ScYSZ. The crystallographic array shows an interplanar distance of 0.520 nm as (111) planes of t-ScYSZ [117]. Figure 2.34c is a schematic illustration representing the lattice constant of the tetragonal structure is very similar to that estimated by analysis of the HRTEM image.

It should be also noted that the assignment of cubic and tetragonal structures, based solely on the X-ray diffraction analysis, can be difficult because the cubic and tetragonal structures ($a = 0.5124$ nm for cubic, and $a = 0.5094$ nm and $c = 0.5177$ nm for tetragonal structures) are very similar [118, 119]. Figure 2.35a is the Raman spectra of 8ScYSZ obtained, using the laser with 532 nm, where the cubic phase or high-temperature phase has characteristic peak at 284 cm^{-1} corresponding to F_{2g} mode. The peak before 200 cm^{-1}, is common in three phase of zirconia [120–124]. However, the six characteristic peaks of tetragonal phase was

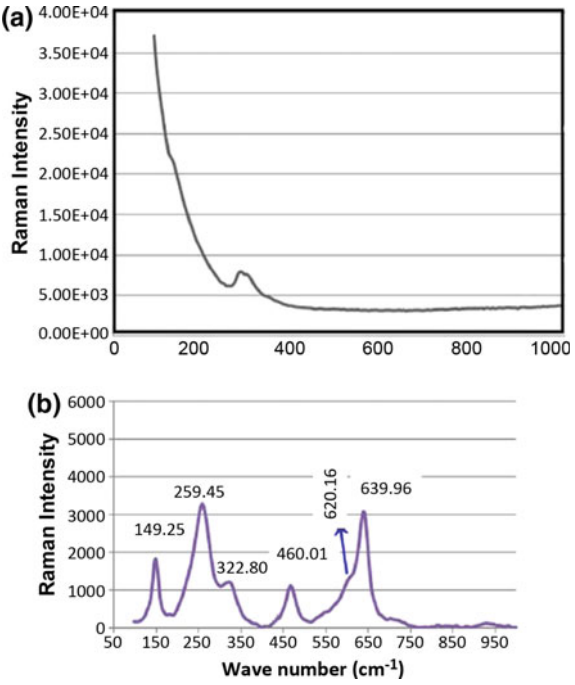

Fig. 2.35 Raman **a** cubic ScYSZ **b** Tetragonal phase of ScYSZ nanoparticles prepared at 700 °C for 2 h (Reprinted with permission from Loghman-Estarki et al. [115], Copyright © 2013, Elsevier)

observed at Raman spectra of 4ScYSZ (Fig. 2.35b). The peaks centered at 149.25 (corresponding to Eg mode), 259.45 (Eg mode), 322.80 (Bg mode), 460.01 (Eg mode), 620.16 (Bg mode) and 639.96 cm^{-1} (A_g mode), confirming that the tetragonal phase of as-obtained ScYSZ was obtained (Fig. 2.35b). The presence of m-ZrO_2 can be ruled out based on the absence of peaks at 102, 179, and 381 cm^{-1}, which are supposed to be the strong peaks for m-ZrO_2 [120–124].

The effects of the mole ratio ethylene glycol monobutyl ether (EGM) to citric acid (CA) in the starting solution on the morphology and particle size of the samples are shown in Fig. 2.36.

When EGM:CA mole ratio was 0.5:1 (Fig. 2.36a), highly packed nanoparticles with diameter between 22 and 28 nm were obtained. A close look at Fig. 2.36a, it was seen that agglomerated particles with 60–70 nm diameters were exist in this sample. When EGM:CA mole ratio was 1.2:1 and 2.4:1, dense agglomerated particles (Fig. 2.36b) with no special shape were obtained. High magnification of the agglomerates in inset of Fig. 2.36b (EGM:CA = 1.2:1) and Fig. 2.36c (EGM:CA = 2.4:1) revealed that the as-formed products consisted of submicrometer grains ($\sim$140 nm diameter, Fig. 2.36b) and submicro- and nanometer grains (80–110 nm diameter, Fig. 2.36c). Upon increasing the EGM:CA mole ratio to 4:1, agglomerated particles with 30–40 nm diameters were obtained (Fig. 2.36d), while in EGM:CA mole ratio to 8:1 (inset Fig. 2.36e), the size of particles decreased to 15–20 nm. By changing the EGM:CA mole ratios to 20:1 (Fig. 2.36f), the

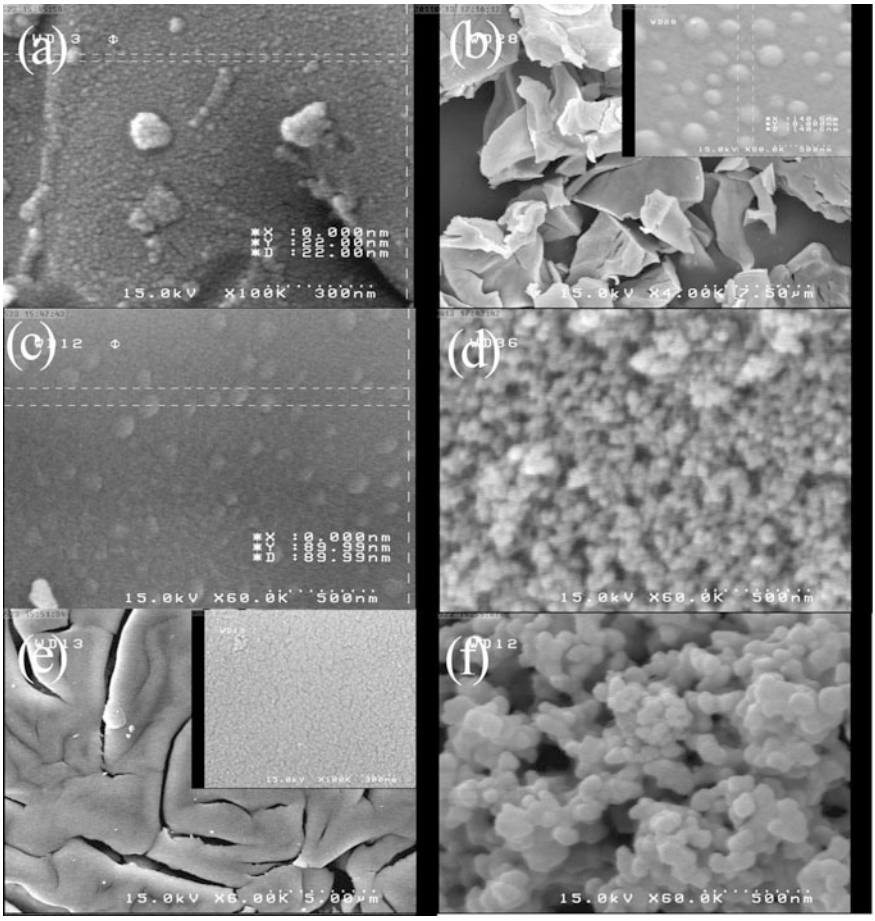

Fig. 2.36 SEM photomicrographs of SYSZ nanoparticles at different EGM:CA ratios: **a** 0.5:1, **b** 1.2:1, **c** 2.4:1, **d** 4:1, **e** 8:1, and **f** 20:1. *Inset* is high magnification of corresponding image (Reprinted with permission from Loghman-Estarki et al. [115], Copyright © 2013, Elsevier)

aggregates with 60–70 nm diameters were produced. These results show that how EGM:CA mole ratios can affect on the morphology and shape of as-obtained products.

For rare earth stabilized zirconia, similar works were done by Ch. Laberty Roberts' groups [52, 53]. In their works, CA:EG (ethylene glycol) mole ratios varied from 0.6 to 2.4 to obtain nanopowders with less porosity and agglomerates. The optimized CA:EG mole ratio was 2.4 ($CA:Zr^{4+}$ = $EG:Zr^{4+}$ = 4.77) and the particle size of the obtained powders was 10-20 nm, as calcinated at 325–400 °C for 6 h. Furthermore, in other similar works by Raissi groups [54], the agglomerated size of YSZ powder was 90 nm with $EG:Zr^{4+}$ = $CA:Zr^{4+}$, which was equal to 4:1, as calcinated at 650 °C/2 h. Another work on ceria stabilized zirconia (CSZ),

using conventional Pechni method (CA:Zr^{4+} = 1.8), was done by Rezaei groups [65]. The crystallite size of CSZ varied from 15.8 to 16.7 nm with increasing CA: EG from 2:1 to 10:1 at the calcination temperature of 700 °C/2 h. Furthermore, Costa [125] also obtained scandia-stabilized zirconia (ScSZ), which mainly consisted of hard agglomerates exhibiting irregular shapes with faceted borders that had an average size of around 20 μm. However, these hard agglomerates consist of sintered nanoparticles resulting from the high-energy environment during thermal decomposition of the large amount of organic compounds used in the synthesis of the polymeric precursors. They used conventional Pechini method with $1Zr^{4+}$:4CA:16EG at 500–650 °C/ 4 h. However, in the present work, the average agglomerated size was 30–40 nm and it consisted of primary particles with ~15 nm diameters, as obtained by EGM:Zr^{4+} = 4:1 at the calcination temperature of 700 °C for 2 h. So, in our case, the average size of agglomerate was less than conventional Pechini method [52–54, 65, 125].

CA molecules can form very stable chelating complexes with many metal ions, and these formed metal–CA complexes can be further stabilized in EG as it possesses two alcoholic hydroxyl functional groups (–OH) with strong complexation affinities to metal ions. Furthermore, two hydroxyl functional groups in one EG molecule can react with three carboxylic acid groups (–COOH) in one CA molecule to form a polyester resin (see reported mechanism in Refs. [38, 126]). In this research, ethylene glycol monobutyl ether (EGM) was applied instead of EG. EGM possesses one alcoholic hydroxyl functional group (–OH) that can react with (–COOH) groups in one CA molecule to form an ester resin. It is clear that ethylene glycol, combined with ether, alcohol, and hydrocarbon chain in one molecule, provides versatile solvency characteristics with both polar and nonpolar properties. However, the effect of EGM and CA molecules on the particle size of products could be due to the steric hindrance [38].

The presence of excess EGM:CA mole ratio plays the role of a space-filling template and the ScYSZ particles embedded in gel matrix became crystalline without interacting with other ScYSZ particles. This increase in the diffusion distance seems to be the actual reason for the decrease in the crystallite size upon further increase in EGM:CA mole ratio from 4:1 to 1.2:1 (see Fig. 2.36) [104].

The effects of pH on the morphologies and particle size of samples in the starting solution was also investigated. The result shows that submicron or large agglomerated ScYSZ nanoparticles (above 80 nm) were obtained at alkali pH. Thus, our groups show that ScYSZ nanoparticles with small size distribution were obtained at acidic pH by modified Pechini method [116, 117] (Fig. 2.37).

The effect of pH on the formation of product can be described in terms of different stability constant of M–CA complex (M = metal) under different pH values. The citric acid is a tri basic acid that can be dissociated in aqueous solution to $C_6H_7O_7^-$, $C_6H_6O_7^{2-}$, and $C_6H_5O_7^{3-}$ based on the pH of solution. In the present work, at low pH (pH = ~1.0), $C_6H_7O_7^-$ is the prevailing species which can interact with M^{n+} ($M = Zr^{4+}$, Sc^{3+}, Y^{3+}) to form complex $M(C_6H_7O_7)^{n-1}$ [116, 117]. At high pH (pH = ~6.0), $C_6H_5O_7^{3-}$ becomes the predominant species which can interact more strongly with M^{n+} to form stable complex $M(C_6H_7O_7)^{n-3}$.

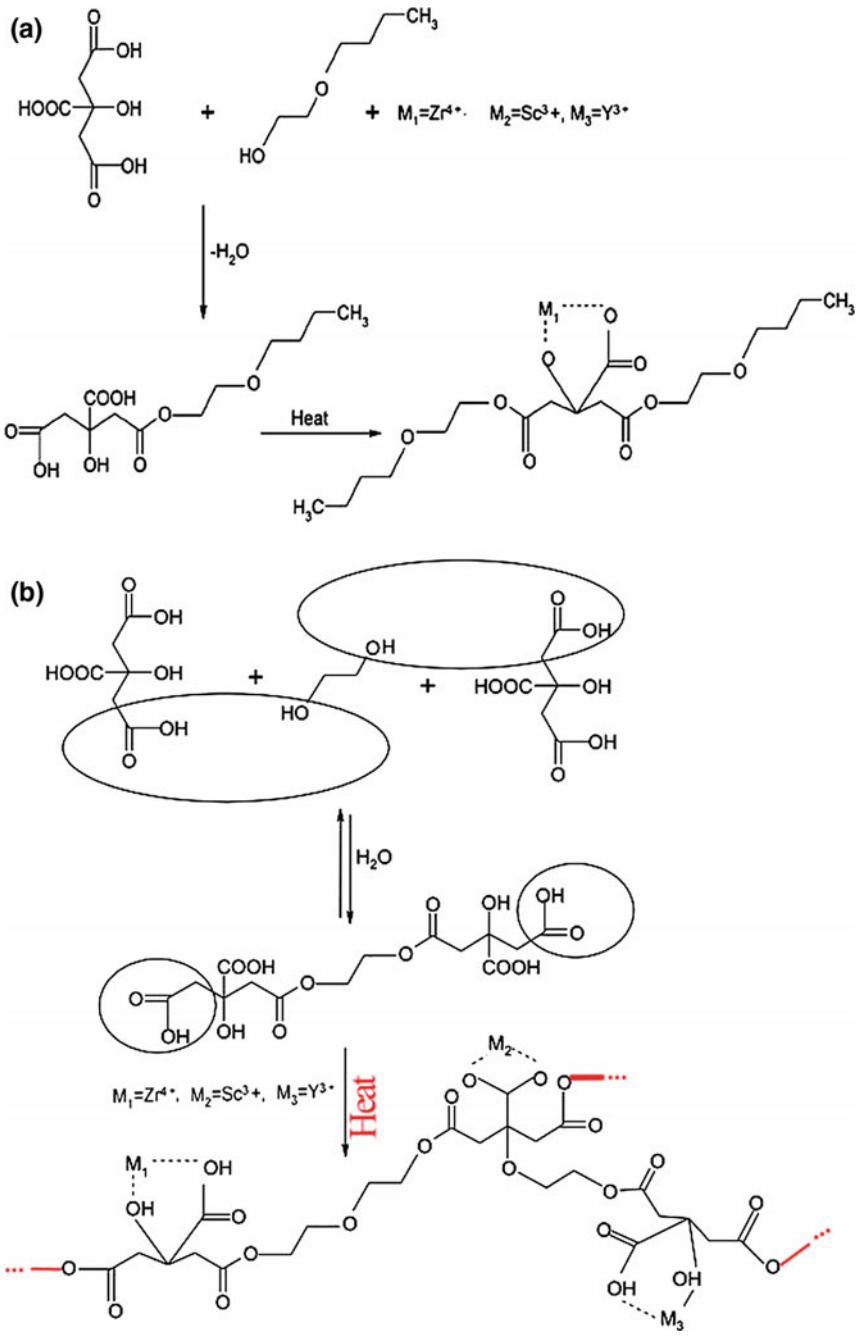

Fig. 2.37 Schematic diagram of probable mechanism of modified Pechini method (**a**) and conventional Pechni method (**b**) (Reprinted with permission from Loghman-Estarki et al. [115], Copyright © 2013, Elsevier)

According to the stability constant for the above reaction, it seems that calcinations temperature ranges of 700–800 °C were not sufficient for breaking the complex $M(C_6H_7O_7)^{n-3}$ formed at pH 9. Upon increasing calcination temperature to 1000 °C, the aforementioned complex was broken and nanoparticles with 90 nm diameter were obtained. At acidic pH, low calcinations temperature was required for the formation of ScYSZ nanoparticles in comparison to the basic pH. It was due to the low stability constant of $M(C_6H_7O_7)^{n-1}$ formed at pH $\sim$ 1. It should also be noted that some researchers have also used an acidic environment (low pH medium) for synthesizing nanocrystals via pechini method. The advantage of using lower ratio of citric acid to metal ions was that the acidic pH was enough to ionize the total amount of $[COOH]^-$ for chelation [127–130].

Before thermal spraying nanoparticles, the nanosized ScYSZ particles should be agglomerated via spray-drying (and then sintered) into microscopic particles. Then, these agglomerated nanoparticles were deposited on the Ni-based super alloy via plasma spraying method. The bond coat powders were sprayed based on the standard parameters recommended by the Sulzer Metco company (Ar flow = 65 slpm, H_2 flow = 14 slpm, arc intensity = 600 A, spraying distance = 120 mm, spraying velocity = 1000 mm/min, anode nozzle internal diameter = 6 mm, and feedstock feed rate = 40 g/min). The parameters used to spray the nanostructured ScYSZ coating were developed internally (Ar flow = 35 slpm, H_2 flow = 10 slpm, arc intensity = 600 A, spraying distance = 120 mm, spraying velocity = 1000 mm/min, anode nozzle internal diameter = 6 mm, and feedstock feed rate = 18 g/min).

The coatings displayed the typical microstructure of APS coatings deposited from nanostructured powders as used here [131, 132]. The literature indicates that such coating microstructures basically comprise two clearly differentiated zones, yielding a two-scale structure [133, 134]. One coating region, which was completely melted (marked M in Fig. 2.38b), consisted mainly of submicrometer-size grains of ScYSZ. The other coating region, which was only partly melted (marked PM), largely retained the microstructure of the starting ScYSZ nanopowder, thus principally making up nanometre-sized grains of ScYSZ (nanozone). The particle size of this splat-quenched ScYSZ is extremely small (20–70 nm, Fig. 2.38d). Moreover, fractured cross-section of both coatings showed that splats had micro-columnar grain structure. This columnar structure was formed by directional solidification at rapid cooling [133].

Moreover, thermal diffusivities of APS nanocoating produced from commercial 7YSZ (Nanox-S4007 powder, spherical granules), and scandia, yttria stabilized zirconia (ScYSZ, synthesized by sol–gel method, nonspherical granules) were obtained 0.0157 cm^2/s and 0.0193 cm^2/s, respectively [15, 16]. It means that thermal insulation of ScYSZ nanocoating was higher than micro-YSZ and lower than nano-YSZ TBCs. It should be noted that the thermal conductivity decreases with an increase in ionic radius of dopants, caused by the reduction in the mean free path of phonons and the presence of excess grain boundaries [133, 134]. Thus, another reason for the lower value of ScYSZ thermal insulation capability is that the ionic radius of Sc^{3+} (0.081 nm) was less than radius of Y^{3+} cations (0.093 nm).

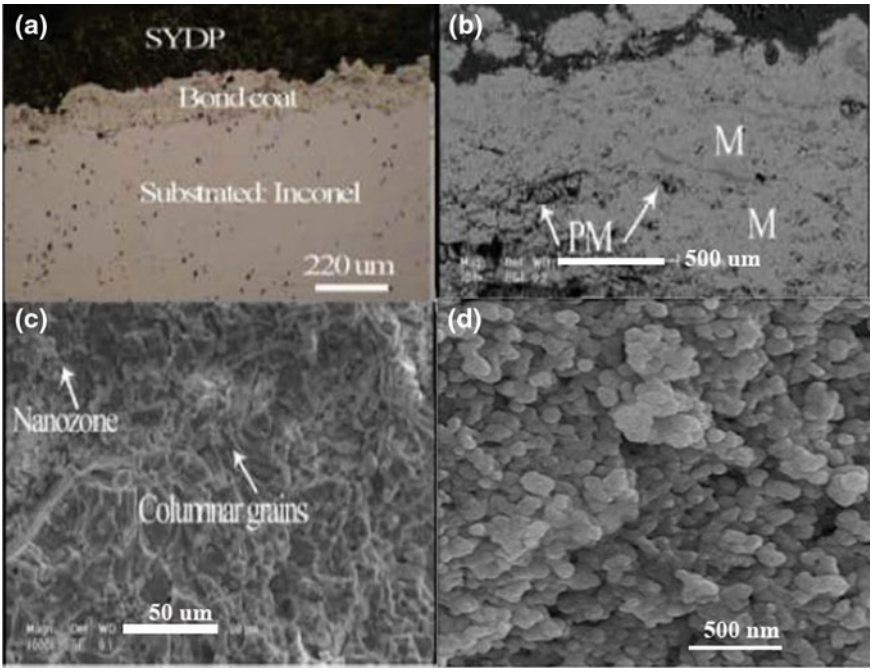

Fig. 2.38 Optical image (**a**) and SEM image of polished (**b**) and fractured (**c**, **d**) cross section of APS coating (Reprinted with permission from Loghman-Estarki et al. [115], Copyright © 2013, Elsevier)

Furthermore, nanostructured ceria stabilized zirconia (CSZ), with 200 and 400 μm thickness, show thermal insulation value of 92 °C and 155 °C, respectively [133, 134]. For further reading about TBC improvement one can read other new articles about this area were cited in Refs. [131–148].

2.2.1.7 Rare Earth Zirconates

Rare earth zirconates have been identified as a class of low thermal conductivity ceramics for possible use in gas-turbine engine applications. Zirconates, such as $SrZrO_3$ (perovskite type), $BaZrO_3$ (perovskite type), and $La_2Zr_2O_7$ with high melting points were investigated for application as materials for thermal barrier coatings at operating temperatures >1300 °C. Thermal expansion coefficients of zirconates were slightly lower than those of YSZ; thermal conductivities of $SrZrO_3$ and $BaZrO_3$ were comparable or slightly higher than those of YSZ. $SrZrO_3$ was not suitable for application as a TBC because of a phase transition at temperatures between 700 and 800 °C. Moreover, $BaZrO_3$ coating was show lower thermal shock resistance (with a gas burner at 1200 °C) with loss of BaO as compared with YSZ coating. On the other hand, among zirconate compound, the $La_2Zr_2O_7$ coating

showed excellent thermal stability and thermal shock behavior. Wu et al. [149] show that all of the rare earth zirconates ($RE_2Zr_2O_7$) including $Gd_2Zr_2O_7$ (pyrochlore phase), (ii) $Gd_2Zr_2O_7$ (fluorite phase), (iii) $Gd_{2.58}Zr_{1.57}O_7$ (fluorite phase), (iv) $Nd_2Zr_2O_7$ (pyrochlore phase), and (v) $Sm_2Zr_2O_7$ (pyrochlore phase) had nearly the same thermal conductivities, all of which were 30% lower than that of 7YSZ. Mechanical properties (hardness, fracture toughness, and Young's modulus) of $BaZrO_3$ and $La_2Zr_2O_7$ samples were determined by indentation techniques and showed lower hardness and Young's modulus as compared to YSZ.

$RE_2Zr_2O_7$ micropowder was usually prepared by coprecipitation of an aqueous solution of $RE(NO_3)_3{\cdot}6H_2O$ and $ZrOCl_2{\cdot}8H_2O$ with a diluted NH_3 solution (NH_4OH; pH = 12.5). In typical synthesis, $RE_2Zr_2O_7$, RE = La, Gd, Pr, Sm, Dy, are prepared by rapidly heating (350 °C) an aqueous solution containing calculated amounts of zirconium nitrate, rare earth-metal nitrate, and carbohydrazide/urea

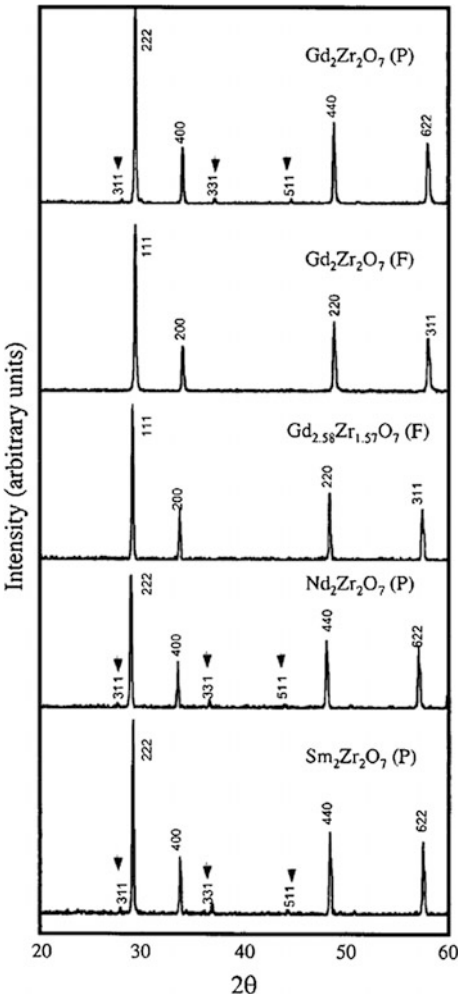

Fig. 2.39 XRD (Cu*K*_ radiation) patterns obtained from hot-pressed and annealed rare earth zirconate specimens. *Arrows* indicate pyrochlore "superlattice" peaks (Reprinted with permission from Jinet et al. [151], Copyright © 2015, Elsevier)

Table 2.14 Particulate properties of rare earth zirconates (Reprinted with permission from AruláDhas [150], Copyright © 1993, Royal Society of Chemistry [RSC])

Compound	Lattice parameter '*a*' (nm)	Powder density (g cm^{-3})	Surface area (m^2 g^{-1})	Particle size[a] (nm)
$La_2Zr_2O_7$	1.0774	4.1 (4.4)	14 (6)	100 (220)
$Ce_2Zr_2O_7$	1.0701	4.3 (4.5)	18 (8)	70 (160)
$Pr_2Zr_2O_7$	1.0658	4.4 (4.8)	20 (10)	60 (120)
$Nd_2Zr_2O_7$	1.0623	4.5 (4.9)	19 (10)	60 (120)
$Sm_2Zr_2O_7$	1.0575	5.0 (5.1)	20 (9)	60 (130)
$Gd_2Zr_2O_7$	1.0503	5.2 (5.5)	16 (9)	70 (120)
$Dy_2Zr_2O_7$	1.0437	5.2 (5.6)	17 (10)	60 (100)

[a]From surface area; value in the parenthesis correspond to rare earth-metal zirconate obtained by urea process

[150, 151]. The formation of $RE_2Zr_2O_7$with the pyrochlore structure was confirmed by XRD (Fig. 2.39). Often it is difficult to distinguish the pyrochlore and fluorite structures by XRD, because of the low intensity of pyrochlore (111), (331), and (511) reflections. The particulate properties of combustion-derived rare earth zirconates are summarized in Table 2.14.

Recently, Pyrochlore $La_2Zr_2O_7$ nanopowders with cubic structure have been first prepared by molten salts method using $La(NO_3)_3{\cdot}6H_2O$ and $ZrOCl_2{\cdot}8H_2O$ as raw materials, as well as K_2SO_4 (anhydrous) and Na_2SO_4 (anhydrous) as molten salts and dispersant agent [152]. Mao et al. [153] have prepared $La_2Zr_2O_7$ nanocrystals by molten salts method using $NaNO_3$ and KNO_3 as molten salts, but they have only prepared the fluorite-type $La_2Zr_2O_7$. In a typical synthesis of pyrochlore $La_2Zr_2O_7$, $La(NO_3)_3{\cdot}6H_2O$) and $ZrOCl_2{\cdot}8H_2O$ were dissolved into the deionized water (solution A), and stirred for 30 min. Then, the dilute ammonia (5 wt%) was added to solution "A" till pH 10–11 with continuous stirring. Dried samples of potassium sulfate anhydrous (K_2SO_4) and sodium sulfate anhydrous (Na_2SO_4) (K_2SO_4: Na_2SO_4 = 1:1 [molar ratio]) were thoroughly mixed in a clean mortar. The mixture of K_2SO_4 and Na_2SO_4 was dissolved into the deionized water (solution B), then poured solution A into solution B with vigorous stirring at 80 °C. Then, slurry was dried at 180 °C for 12 h in a oven. Herein, the molar ratio of the salts to the raw materials was selected as 1:1. The remaining solid was transferred into a covered corundum crucible and heated to 800–900 °C at a rate of 8 °C/min with a box furnace in air and then isothermally annealed at 800 °C for 0.5–2 h. After being cooled to room temperature, the resulting product was washed by a large number of deionized water and ethanol for subsequent separation and purification.

Figure 2.40 shows the XRD patterns of the samples prepared at 800 and 900 °C for 0.5, 1 and 2 h, respectively. It is reported in literature [154] that the binary oxides of rare earths with zirconia have two types of structures, i.e. pyrochlore (La_2O_3, Pr_6O_7–Gd_2O_3) and fluorite (Y_2O_3, Tb_2O_3–Lu_2O_3). The fully crystallized LZ has a pyrochlore structure which is very similar to that of the fluorite structure and the two weak peaks of 2 h between 35° (peak [3 3 1]) and 45° (peak [5 1 1]) are

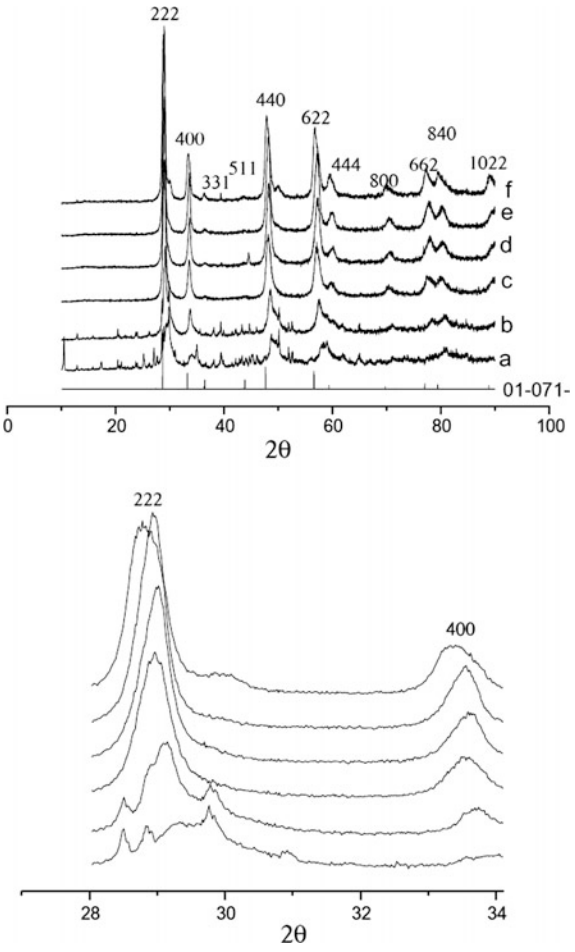

Fig. 2.40 XRD patterns of $La_2Zr_2O_7$ nanocrystals prepared at: **a** 800 °C, 0.5 h **b** 800 °C, 1 h **c** 800 °C, 2 h **d** 900 °C, 0.5 h **e** 900 °C, 1 h and **f** 900 °C, 2 h (Reprinted with permission from Wang et al. [152], Copyright © 2010, Elsevier)

the indication of pyrochlore structure [5, 6, 13]. Pattern (a) shows that the crystallinity is quite low and the main peaks are close to ZrO_2 and La_2O_3. Patterns (b and c) do not have these two peaks too. The peak [3 3 1] and peak [5 1 1] appeared when the temperature increased to 900 °C, as shown in pattern (d), pattern (e) and pattern (f), which implied that LZ powders had a phase transition when the temperature reached to 900 °C. The diffraction peaks can be readily indexed to the pyrochlore crystal system $La_2Zr_2O_7$ (JCPDS:01-071-2363). Compared with traditional solid state reaction, the synthesis temperature and time are lower and shorter. This is because the salts can become to ionic liquid at some temperature which has good heat transfer property and could enhance the fluidity and the proliferation speed of the reactants. As shown in the magnified peak of [2 2 2] and [4 0 0], the peaks of LZ powders shift to the low degree side with the increase of temperature,

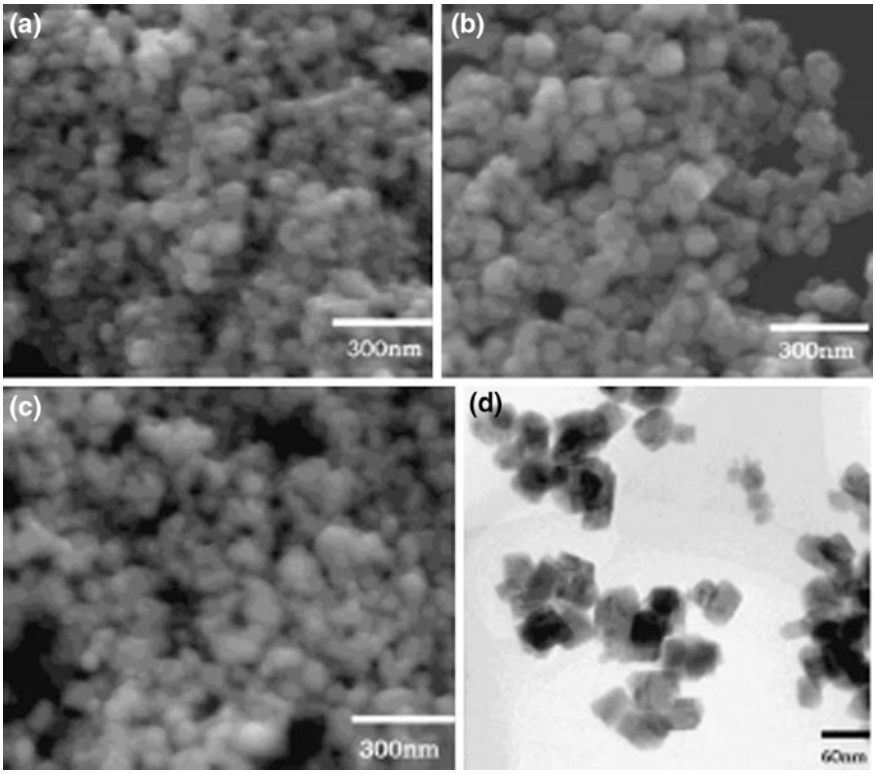

Fig. 2.41 SEM images of $La_2Zr_2O_7$ nano particles. **a** 900 °C, 0.5 h **b** 900 °C, 1 h **c** 900 °C, 2 h and **d** 900 °C, 1 h (TEM images) (Reprinted with permission from Wang et al. [152], Copyright © 2010, Elsevier)

implying that the lattice parameter increases with the increase of the nano-grain size.

SEM and TEM were employed to obtain direct information about the size and morphologies of the produced nanopowders. The typical SEM images (Fig. 2.41a) show that the as-obtained nanopowders are all composed of cuboid-like particles which are also very symmetrical. This is due to the ionic liquid penetrated in entire reaction process and prevented the particles to reunite effectively. The average size of $La_2Zr_2O_7$ particles observed ranges from 60 to 90 nm and becomes a little larger with the reactive time and temperature increases.

2.2.1.8 Zirconia—Alumina Nanocomposite

Different methods have been proposed to improve the hot corrosion resistance of the coating as follows [86, 135, 136, 146, 155–160]:

(1) Use of more resistant stabilizers, such as In_2O_3, Sc_2O_3, and CeO_2 (2) Laser glazing and remelting of coating provided a dense and pore-free layer to prevent salt penetration into the coating (3) Deposition of a dense alumina overlay on the surface of YSZ coating by EB-PVD technique that reduced salt infiltration (4) Deposition of Al_2O_3–YSZ composite or nanocomposite on bond coating of TBC system.

Due to brittleness problem of monolithic YSZ ceramics, nanocomposites have received significant scientific and technological attention over the past several decades. Zirconia toughened alumina (ZTA), a crucial example of such composites, has been used for broad industrial applications especially in the field of structural ceramics (such as in heat engines, rocket nozzles, and cutting tools) and TBCs. ZTA composites exhibit excellent mechanical properties including high strength, high toughness, good wear resistance as well as better thermal and chemical stability. The properties of ZTA were belonged to (i) uniformity of the t-ZrO_2 particle distribution, (ii) A small and narrow size distribution of ZrO_2 particles, (iii) Absence of coarsening of t-ZrO_2 particles during heat treatments. This composite can be synthesized mainly by mechanical mixing, wet and high-energy milling, liquid phase precursor methods (e.g., sol–gel), combustion, citrate–nitrate, emulsion precursor, coprecipitation, and hydrothermal methods. Deb et al. [159] was synthesized 20 vol.% ZrO_2 (20 vol.% Y_2O_3)–Al_2O_3 nanocomposite by three different gel agent (tartaric, glycolic, and citric acids). The advantages of this method include that (i) it is moderately a much faster and easier process, (ii) it can be performed at relatively lower temperature, and (iii) homogenous composites powders with high purity can be obtained. Experiments were carried out as follows: First, the starting solution was prepared by dissolving $Al(NO_3)_3{\cdot}9H_2O$ into distilled water. The concentration of aluminum nitrate was 0.5 M. The required amount of $ZrOCl_2{\cdot}8H_2O$ was added into aluminum nitrate solution to reach the final composition containing 20 vol.% zirconia. The acid was completely dissolved into deionized water to a molar concentration of 0.5 M. Then, the acid was added to mixed solution to assure equal ratio of acid to metal nitrate. YCl_3 was introduced to mixture at room temperature. The solution was continuously magnetically stirred for several hours and kept at the temperature of 80 °C until the clear solution was obtained. Then, temperature on magnetic stirrer was adjusted to 200 °C. The viscosity of mixed solution increased and its color became yellowish in a couple of hours. The gelation of mixture was observed after indication of the changes in color and viscosity in the mixture. The gel was conveyed to a mantle heater where temperature was adjusted to 400 °C for 8 h to remove organic matters in air. Finally, powders or gel precursor were obtained. This precursor was ground with mortar and pestle for just 5 min to avoid any possible phase transformation from tetragonal to monoclinic. Heat treatment was carried out on the powders at various temperatures (from 400 to 1500 °C) for 2 h.

Figure 2.42 exhibits the XRD patterns of ZTA gelled in tartaric acid at various calcination temperatures. Nanocrystalline metastable t-ZrO_2 and the partial phase transformation from γ-Al_2O_3 to α-Al_2O_3 were obtained near 1000 °C, subsequently only the mixture of α-Al_2O_3 and t-ZrO_2 were determined up to 1500 °C. The

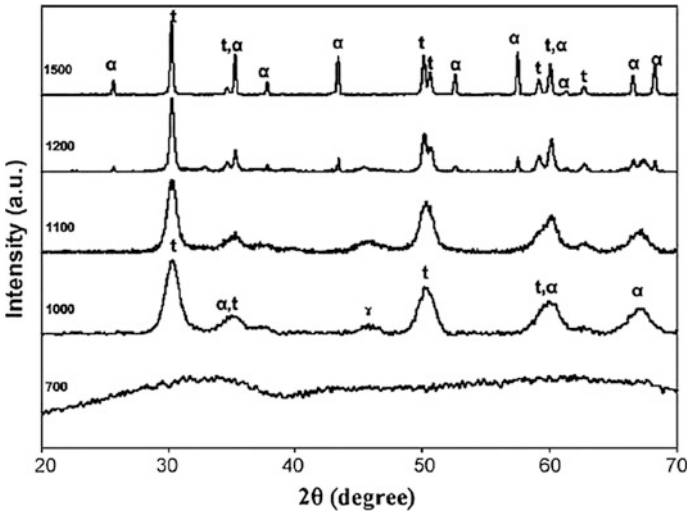

Fig. 2.42 XRD patterns of ZTA gelled in tartaric acid at various calcination temperatures (t: tetragonal zirconia, _: alpha alumina) [160] (Reprinted with permission from Copyright © 2008, Elsevier)

monoclinic phase of zirconia was not detected at significant amount although the crystallite size of tetragonal zirconia was changed from 6 to 9 nm and 42–49 nm at 1000 and 1500 °C, respectively. Although the low temperature stabilization of the tetragonal instead of monoclinic phase depends on the amount of stabilizer with its distribution, synthesis route, intrinsic defects and water vapor in crystallite growth, it is typically associated with the crystal size of the tetragonal structure [156, 157]. This might be attributed to the inhibition of coarsening of the t-ZrO_2 grains by the alumina particles. It was also observed that no significant changes in the XRD patterns occurred in the nanocomposites even though the acids having various functional groups were used for gelation. In summary, the average crystallite size of nanocomposite heat treated at 1000 °C was less than 10 nm and tetragonal zirconia phase without transformation to monoclinic phase, which remained in the alumina matrix close to 1500 °C. However, monoclinic phase was observed from Raman spectra of samples heated at 1500 °C.

It is assumed that acids with various functional groups, such as carboxyl and hydroxyl unit influence gelation characteristics of mixture. Furthermore, it was observed the surface areas of the samples were changed with varying gel agent (58 m^2/g (glycolic), 168.6 m^2/g (tartaric acid) to 278 m^2/g [citric acids]). The uniqueness of tartaric and citric acids derives from the presence of 2 carboxylate–2 hydroxylate and 3 carboxylate–1 hydroxylate groups in the molecular structure, respectively, whereas glycolic acid has only 1 carboxylate–1 hydroxylate groups which can act as donors and build a complex with a central metal atom. These molecules can operate as bidentate ligands and establish chelate complex with metals It has also been calculated that the interaction energy between powders and

organic compound rises with increasing functional groups, such as carboxyl (–COOH) and hydroxyl (–OH) in the molecular structure [158]. Therefore, tartaric and citric acids might exhibit better performance during the building of chelate complex and gelation due to having more functional groups than glycolic acid has. Thus, powders synthesized by using tartaric and citric acids revealed higher surface area than that by glycolic acid.

TEM data in Fig. 2.43 showed that synthesized powders have equiaxed-rounded shape and the crystallite size was in good agreement with XRD results. The contrasted bright and dark areas within the images on the nanocomposite correspond to

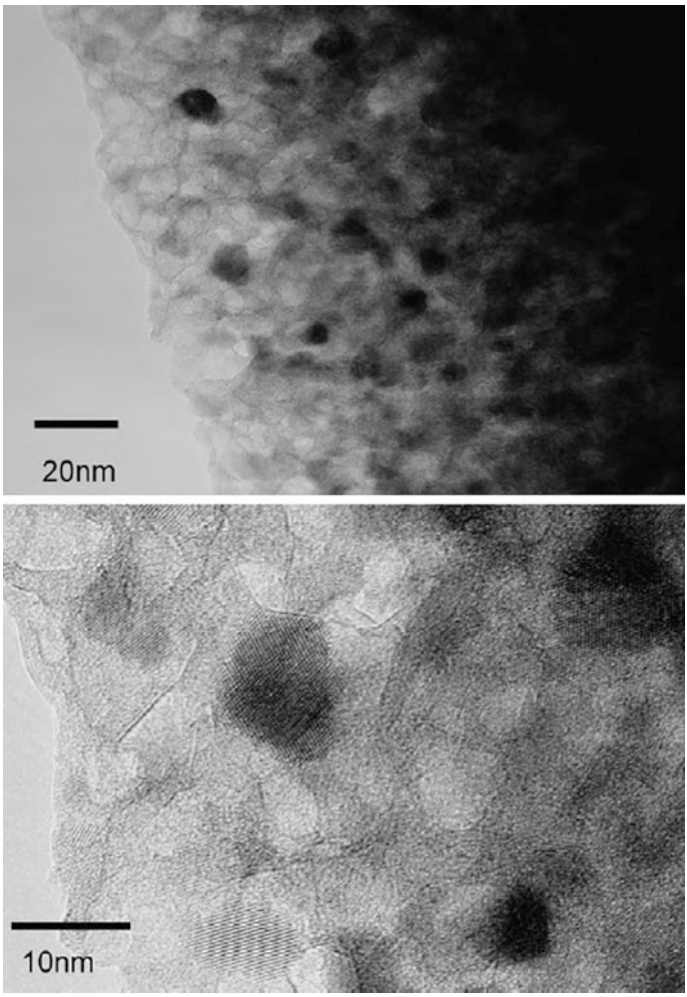

Fig. 2.43 TEM micrographs ZTA with citric acid at 1000 °C for 2 h. Zirconia appeared as dark regions, while alumina appeared as bright region (Reprinted with permission from Gocmez et al. [160], Copyright © 2010, Elsevier)

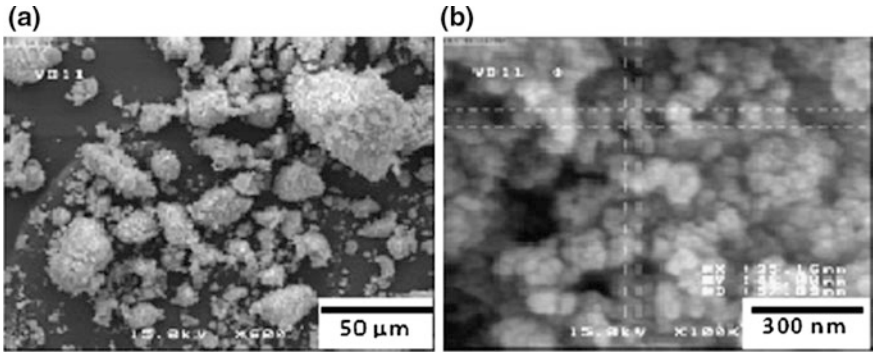

Fig. 2.44 SEM images of nanoagglomerated powders: **a** YSZ **b** YSZ–15 wt% Alumina [161]

the Al_2O_3 and ZrO_2, respectively. According to literature, the ZrO_2 is stabilized in tetragonal phase due to encapsulation in the porosity of the α-Al_2O_3 grains. The boundaries of the alumina pores prevent the growth of ZrO_2 and consequently stabilize the ZrO_2 in the tetragonal phase [159, 160].

Recently, Z. valefi was reported simple route for preparation of plasma sprayable alumina-YSZ nanocomposite [161]. To produce the spray feedstock, nanopowders of ZrO_2–8 wt% Y_2O_3 (nanostructured and amorphous materials Inc.; product name: Zirconia Yttria nanopowder; 5933ZS; particle size 20–30 nm) and Al_2O_3 were mixed according to final composition of YSZ with 5, 10 and 15 wt% of Alumina (nanostructured and amorphous materials Inc.; product name: α-Alumina powder 1005MR; particle size $\sim$150 nm) and then suspended in water. The suspensions were heated to result a solid mass after evaporation of water. During the heating process the suspensions were stirred by a magnetic stirrer until the viscosity of suspension was high enough to minimize phase separation. After complete evaporation the stirrer was separated from the resulted mass and the powder suitable for spraying was produced by grinding and sieving of the solid mass in the range of 45–90 µm (Fig. 2.44).

After plasma spraying this feedstock on substrate, as we can see (Fig. 2.45) the splat formation for YSZ–15 wt% Alumina coating is higher. Considering the phase diagram of YSZ–Al_2O_3 system, it shows that increasing the amount of Al_2O_3 up to about 40 mass% decreases the melting point of the solid solution to about 1866 °C. It can be expected that the melting point of YSZ–15 wt% Alumina is lower than YSZ–5 and 10 wt% Alumina coatings so choosing the same spray parameters for these coatings results in more splat formation in bimodal structure for YSZ–15 wt% Al_2O_3.

It is believed that Al_2O_3 material is effective in suppressing the oxidation of TBC system. And hence, it increases the lifetime of the coated component and improves its reliability. Another conclusion that can be extracted from Fig. 2.46 is that the oxidation resistance of YSZ with 5 and 15 wt% Alumina coatings is higher than YSZ with 10 wt% Alumina. This group [161] was also show that tensile

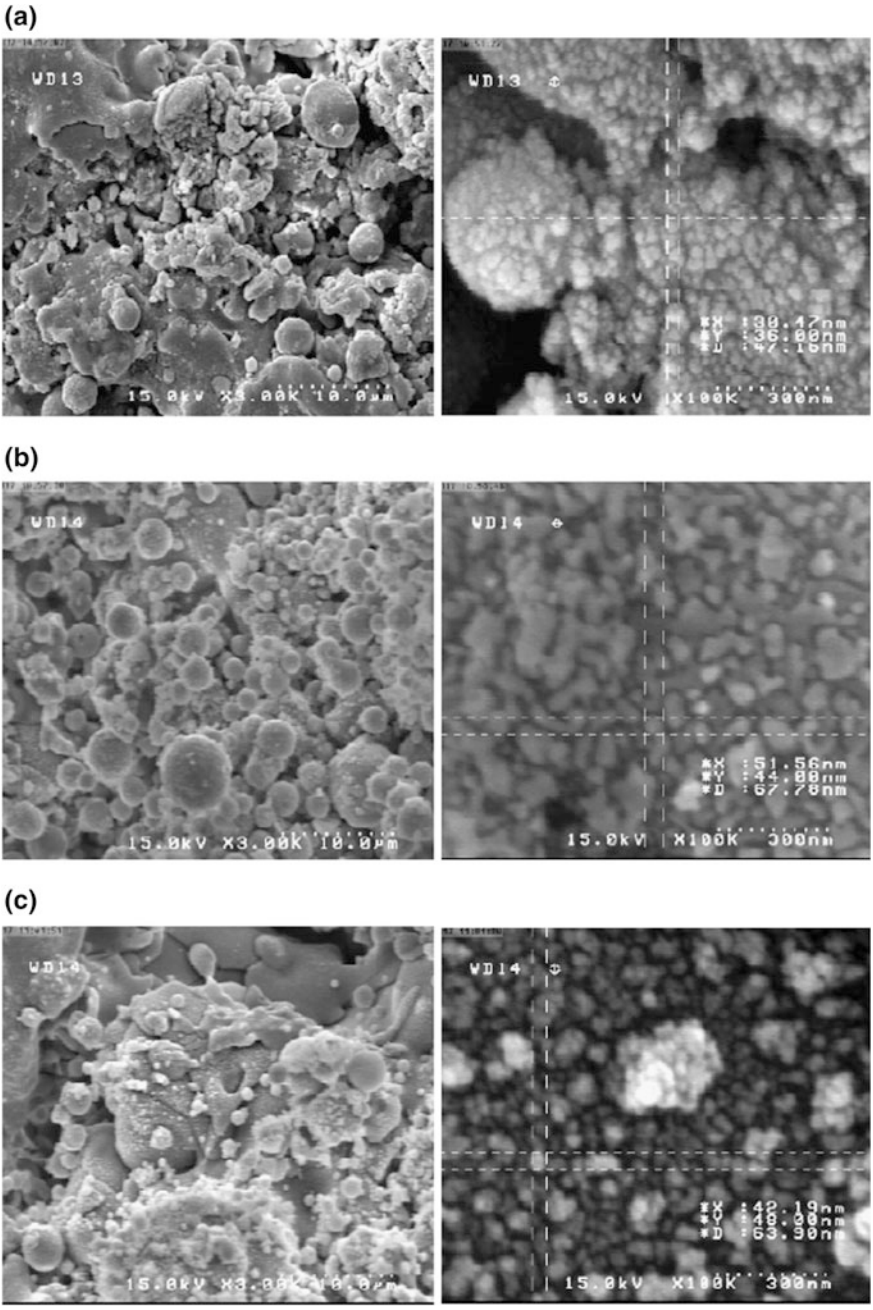

Fig. 2.45 SEM images from the surface YSZ–Alumina composite coatings produced by nanoagglomerated powders. **a** YSZ–5 wt% Al_2O_3 **b** YSZ–10 wt% Al_2O_3 **c** YSZ–15 wt% Al_2O_3 (Reprinted with permission from Saremi et al. [161], Copyright © 2013, Elsevier)

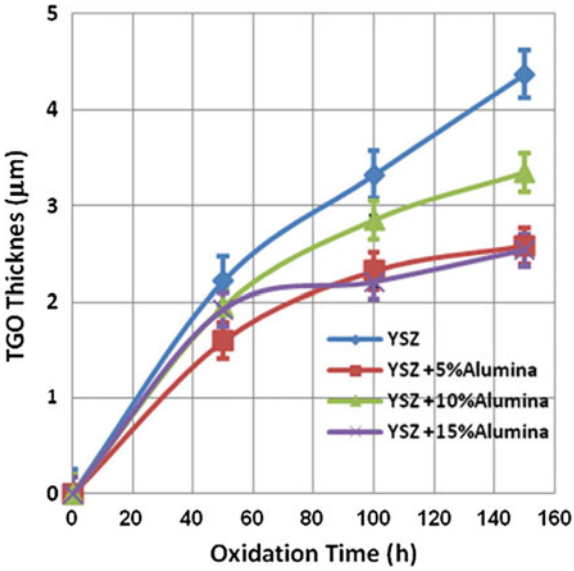

Fig. 2.46 Evolution of TGO layer thickness with oxidation time for YSZ and YSZ–Alumina coatings (Reprinted with permission from Saremi et al. [161], Copyright © 2013, Elsevier)

strength and Thermal shock and corrosion resistance of nanostructured YSZ–15 wt % alumina coatings was higher than related to YSZ coatings.

2.3 Summary

The review of various synthesis methods for the preparation of zirconia-based nanostructure for thermal barrier coatings (TBCs) show that wet chemical method especially modified sol–gel-based route, such as Pechini method have a scale-up potential for preparation of large-scale synthesis of variety of zirconia-based nanostructure for TBCs. Literature review show that in the case of hot corrosion resistance of TBCs, the ScYSZ coating is the best one but this coating have lower thermal conductivity than conventional YSZ TBCs. Thus, for having thermal shock, corrosion resistance and low thermal conductivity nanostructured YSZ is the best option for TBCs. However, effort for the synthesis of nanostructured codoped zirconia, and zirconia nanocomposite, were ongoing to improve life time of TBCs.

References

1. Stevens R (1986) An introduction to zirconia, Magnesium Elektron. Deutsche Übersetzung in: Handbuch der Keramik, Deutscher Wirtschaftsdienst
2. Hannink RH, Kelly PM, Muddle BC (2000) Transformation toughening in zirconia-containing ceramics. J Am Ceram Soc 83(3):461–487

3. Brog J-P, Chanez C-L, Crochet A, Fromm KM (2013) Polymorphism, what it is and how to identify it: a systematic review. Rsc Advances 3(38):16905–16931
4. Ikeno H, Krause M, Thomas H, Patzig C, Hu Y, Gawronski A, Tanaka I, Christian R (2013) Variation of Zr-L2, 3 XANES in tetravalent zirconium oxides. J Phys: Condens Matter 25 (16):165505
5. Patil KC, Hegde M, Rattan T, Aruna S (2008) Chemistry of nanocrystalline oxide materials-combustion synthesis, properties and applications. World Scientific, New Jersey
6. Davar F, Hassankhani A, Loghman-Estarki MR (2013) Controllable synthesis of metastable tetragonal zirconia nanocrystals using citric acid assisted sol–gel method. Ceram Int 39(3):2933–2941
7. Viazzi C, Bonino J-P, Ansart F, Barnabé A (2008) Structural study of metastable tetragonal YSZ powders produced via a sol–gel route. J Alloy Compd 452(2):377–383
8. Shane M, Mecartney M (1990) Sol-gel synthesis of zirconia barrier coatings. J Mater Sci 25 (3):1537–1544
9. Cao X, Vassen R, Stoever D (2004) Ceramic materials for thermal barrier coatings. J Eur Ceram Soc 24(1):1–10
10. Clarke DR, Phillpot SR (2005) Thermal barrier coating materials. Mater Today 8(6):22–29
11. Maloney MJ (2001) Thermal barrier coating systems and materials. US Patent 6 117 560
12. Lima R, Marple B (2008) Nanostructured YSZ thermal barrier coatings engineered to counteract sintering effects. Mater Sci Eng, A 485(1):182–193
13. Racek O, Berndt CC, Guru D, Heberlein J (2006) Nanostructured and conventional YSZ coatings deposited using APS and TTPR techniques. Surf Coat Technol 201(1):338–346
14. Lima R, Kucuk A, Berndt C (2002) Bimodal distribution of mechanical properties on plasma sprayed nanostructured partially stabilized zirconia. Mater Sci Eng, A 327(2):224–232
15. Loghman-Estarki MR, Edris H, Jamali H, Ghasemi R, Pourbafrany M, Erfanmanesh M, Ramezani M (2013) Spray drying of nanometric SYSZ powders to obtain plasma sprayable nanostructured granules. Ceram Int 39(8):9447–9457
16. Loghman-Estarki MR, Pourbafrany M, Razavi RS, Edris H, Bakhshi SR, Erfanmanesh M, Jamali H, Hosseini SN, Hajizadeh-Oghaz M (2014) Preparation of nanostructured YSZ granules by the spray drying method. Ceram Int 40(2):3721–3729
17. Brandon J, Taylor R (1989) Thermal properties of ceria and yttria partially stabilized zirconia thermal barrier coatings. Surf Coat Technol 39:143–151
18. Khan AN, Khan S, Ali F, Iqbal M (2009) Evaluation of ZrO2–24MgO ceramic coating by eddy current method. Comput Mater Sci 44(3):1007–1012
19. Kvernes I (1979) Ceramic coatings on diesel engine components. In: Kvernes I et al (eds) Central Institute for Industrial Research, Oslo, Norway, Dec 1979. From conference on advanced materials for alternate fuel capable directly fired heat engines, pp 233–257
20. Schulz U, Fritscher K, Peters M (1996) EB-PVD Y 2 O 3-and $CeO_2Y_2O_3$-stabilized zirconia thermal barrier coatings—crystal habit and phase composition. Surf Coat Technol 82(3):259–269
21. Chatterjee M, Chatterjee A, Ganguli D (1992) Preparation of ZrO_2–CaO and ZrO_2–MgOfibres by alkoxide Sol–Gel processing. Ceram Int 18(1):43–49
22. Wang S et al (2006) Coprecipitation synthesis of MgO-doped ZrO_2 nano powder. J Am Ceram Soc 89(11):3577–3581
23. Muccillo R, Saito N, Muccillo E (1995) Properties of zirconia-magnesia solid electrolytes prepared by the citrate method. Mater Lett 25(3):165–169
24. Yuan L, Xiang D, J-k Yu (2013) Effect of solvents on the properties of co-precipitated MgO-ZrO_2 nano powders. J Ceram Process Res 14(4):517–520
25. Kim N, Hsieh C-H, Huang H, Prinz FB, Stebbins JF (2007) High temperature 17 O MAS NMR study of calcia, magnesia, scandia and yttria stabilized zirconia. Solid State Ionics 178(27):1499–1506
26. Balmer ML, Lange FF, Levi CG (1992) Metastable phase selection and partitioning in ZrO2—MgO processed from liquid precursors. J Am Ceram Soc 75(4):946–952

27. Settu T (2000) Characterisation of MgO–ZrO_2 precursor powders prepared by in-situ peptisation of coprecipitated oxalate gel. Ceram Int 26(5):517–521
28. Gocmez H, Fujimori H (2008) Synthesis and characterization of ZrO_2–MgO solid solutions by citrate gel process. Mater Sci Eng, B 148(1):226–229
29. Angeles-Rosas M, Camacho-López MA, Ruiz-Trejo E (2010) Structure, conductivity and luminescence of 8 mol% scandia-doped zirconia prepared by sol–gel. Solid State Ionics 181(29):1349–1354
30. Ishigame M, Sakurai T (1977) Temperature dependence of the Raman spectra of ZrO_2. J Am Ceram Soc 60(7–8):367–369
31. Garvie RC, Nicholson PS (1972) Phase analysis in zirconia systems. J Am Ceram Soc 55(6):303–305
32. Stubican V, Hink RC, Ray SP (1978) Phase equilibria and ordering in the system ZrO_2–Y_2O_3. J Am Ceram Soc 61(1–2):17–21
33. Liu DW, Perry CH, Wang W, Ingel RP (1987) Low frequency Raman spectra in disordered cubic zirconia at elevated temperatures. J Appl Phys 62:250
34. Phillippi C, Mazdiyasni K (1971) Infrared and Raman spectra of zirconia polymorphs. J Am Ceram Soc 54(5):254–258
35. Rashad M, Baioumy H (2008) Effect of thermal treatment on the crystal structure and morphology of zirconia nanopowders produced by three different routes. J Mater Process Technol 195(1):178–185
36. Fujimori H, Yashima M, Sasaki S, Kakihana M, Mori T, Tanaka M, Yoshimura M (2001) Cubic–tetragonal phase change of yttria-doped hafnia solid solution: high-resolution X-ray diffraction and Raman scattering. Chem Phys Lett 346(3):217–223
37. Arul Dhas N, Patil KC (1993) Properties of magnesia-stabilized zirconia powders prepared by a combustion route. J Mater Sci Lett 12(23):1844–1847
38. Sakka S (2005) Handbook of sol-gel science and technology. 1. Sol-gel processing, vol 1. Springer Science & Business Media
39. Hajizadeh-Oghaz M, Razavi RS, Khajelakzay M (2015) Optimizing sol–gel synthesis of magnesia-stabilized zirconia (MSZ) nanoparticles using Taguchi robust design for thermal barrier coatings (TBCs) applications. J Sol-Gel Sci Technol 73(1):227–241
40. Rauf A, Yu Q, Jin L, Zhou C (2012) Microstructure and thermal properties of nanostructured lanthana-doped yttria-stabilized zirconia thermal barrier coatings by air plasma spraying. Scripta Materialia 66(2):109–112
41. Guo X (1997) Space-charge conduction in yttria and alumina codoped-zirconia 1. Solid State Ionics 96(3):247–254
42. Ramaswamy P, Seetharamu S, Varma K, Rao K (1999) Evaluation of CaO–CeO_2–partially stabilized zirconia thermal barrier coatings. Ceram Int 25(4):317–324
43. Esparza-Ponce H, Reyes-Rojas A, Antunez-Flores W, Miki-Yoshida M (2003) Synthesis and characterization of spherical calcia stabilized zirconia nano-powders obtained by spray pyrolysis. Mater Sci Eng, A 343(1):82–88
44. Miller RA (1997) Thermal barrier coatings for aircraft engines: history and directions. J Therm Spray Technol 6(1):35–42
45. Shukla A, Sharma V, Dhas NA, Patil K (1996) Oxide-ion conductivity of calcia-and yttria-stabilized zirconias prepared by a rapid-combustion route. Mater Sci Eng, B 40(2): 153–157
46. Arul Dhas N, Patil K (1992) Combustion synthesis and properties of tetragonal, monoclinic, and partially and fully stabilized zirconia powders. Int J Self-Propag High-Temp Synth 1:576–589
47. Viazzi C, Deboni A, Ferreira JZ, Bonino J-P, Ansart F (2006) Synthesis of yttria stabilized zirconia by sol–gel route: influence of experimental parameters and large scale production. Solid State Sci 8(9):1023–1028
48. Viazzi C, Bonino J-P, Ansart F (2006) Synthesis by sol-gel route and characterization of yttria stabilized zirconia coatings for thermal barrier applications. Surf Coat Technol 201(7):3889–3893

49. Pin L, Ansart F, Bonino J-P, Le Maoult Y, Vidal V, Lours P (2011) Processing, repairing and cyclic oxidation behaviour of sol–gel thermal barrier coatings. Surf Coat Technol 206(7):1609–1614
50. Pin L, Ansart F, Bonino J-P, Le Maoult Y, Vidal V, Lours P (2013) Reinforced sol–gel thermal barrier coatings and their cyclic oxidation life. J Eur Ceram Soc 33(2):269–276
51. Pin L, Vidal V, Blas F, Ansart F, Duluard S, Bonino J-P, Le Maoult Y, Lours P (2014) Optimized sol–gel thermal barrier coatings for long-term cyclic oxidation life. J Eur Ceram Soc 34(4):961–974
52. Laberty-Robert C, Ansart F, Deloget C, Gaudon M, Rousset A (2001) Powder synthesis of nanocrystallineZrO 2–8% Y 2 O 3 via a polymerization route. Mater Res Bull 36(12): 2083–2101
53. Laberty-Robert C, Ansart F, Castillo S, Richard G (2002) Synthesis of YSZ powders by the sol-gel method: surfactant effects on the morphology. Solid State Sci 4(8):1053–1059
54. Farhikhteh S, Maghsoudipour A, Raissi B (2010) Synthesis of nanocrystalline YSZ (ZrO 2–8Y 2 O 3) powder by polymerized complex method. J Alloy Compd 491(1):402–405
55. Petrova N, Todorovsky D (2006) Thermal decomposition of zirconium–yttrium citric complexes prepared in ethylene glycol and water media. Mater Res Bull 41(3):576–589
56. Hajizadeh-Oghaz M, Razavi RS, Loghman-Estarki MR (2014) Synthesis and characterization of non-transformable tetragonal YSZ nanopowder by means of Pechini method for thermal barrier coatings (TBCs) applications. J Sol-Gel Sci Technol 70(1):6–13
57. Hajizadeh-Oghaz M, Razavi RS, Loghman Estarki MR (2014) Large-scale synthesis of YSZ nanopowder by Pechini method. Bull Mater Sci 37(5):969–973
58. Oghaz MH, Razavi RS, Loghman-Estark MR, Ghasemi R (2012) Optimization of morphology and particle size of modified sol gel synthesized YSZ nanopowder using Taguchi method. J Nano Res (Trans Tech Publ), 65–70
59. Majedi A, Davar F, Abbasi A (2014) Sucrose-mediated sol–gel synthesis of nanosized pure and S-doped zirconia and its catalytic activity for the synthesis of acetyl salicylic acid. J Ind Eng Chem 20(6):4215–4223
60. Prabhakaran K, Melkeri A, Gokhale N, Sharma S (2007) Synthesis of nanocrystalline 8 mol% yttria stabilized zirconia powder from sucrose derived organic precursors. Ceram Int 33(8):1551–1555
61. Finar IL (1973) Organic Chemistry, vol I: the fundamental principles, Longman, London, pp. 503–530
62. Gong W, Sha C, Sun D, Wang W (2006) Microstructures and thermal insulation capability of plasma-sprayed nanostructured ceria stabilized zirconia coatings. Surf Coat Technol 201(6):3109–3115
63. Park S, Kim J, Kim M, Song H, Park C (2005) Microscopic observation of degradation behavior in yttria and ceria stabilized zirconia thermal barrier coatings under hot corrosion. Surf Coat Technol 190(2):357–365
64. Yuan Q, Duan H-H, Li L-L, Sun L-D, Zhang Y-W, Yan C-H (2009) Controlled synthesis and assembly of ceria-based nanomaterials. J Colloid Interface Sci 335(2):151–167
65. Rezaei M, Alavi S, Sahebdelfar S, Yan Z-F (2009) Synthesis of ceria doped nanozirconia powder by a polymerized complex method. J Porous Mater 16(5):497–505
66. Reddy BM, Reddy GK, Reddy LH, Ganesh I (2009) Synthesis of nanosized ceria-zirconia solid solutions by a rapid microwave-assisted combustion method. Open Phys Chem J 3(1):24–29
67. Reddy BM, Khan A, Yamada Y, Kobayashi T, Loridant S, Volta J-C (2003) Raman and X-ray photoelectron spectroscopy study of CeO_2–ZrO_2 and V_2O5/CeO_2–ZrO_2 catalysts. Langmuir 19(7):3025–3030
68. Martínez-Arias A, Fernández-García M, Ballesteros V, Salamanca L, Conesa J, Otero C, Soria J (1999) Characterization of high surface area Zr–Ce (1: 1) mixed oxide prepared by a microemulsion method. Langmuir 15(14):4796–4802
69. McBride J, Hass K, Poindexter B, Weber W (1994) Raman and X-ray studies of $Ce_{1-x}RE_xO_{2-y}$, where RE = La, Pr, Nd, Eu, Gd, and Tb. J Appl Phys 76(4):2435–2441

70. Quinelato A et al (2001) Synthesis and sintering of ZrO_2–CeO_2 powder by use of polymeric precursor based on Pechini process. J Mater Sci 36(15):3825–3830
71. Tu H, Liu X, Yu Q (2011) Synthesis and characterization of scandia ceria stabilized zirconia powders prepared by polymeric precursor method for integration into anode-supported solid oxide fuel cells. J Power Sources 196(6):3109–3113
72. Turner C (1991) Sol-gel process-principles and applications. Am Ceram Soc Bull 70(9):1487–1490
73. Livage J, Henry M, Sanchez C (1988) Sol-gel chemistry of transition metal oxides. Prog Solid State Chem 18(4):259–341
74. Johnson DW Jr (1985) Sol-gel processing of ceramics and glass. Am Ceram Soc Bull 64(12):1597–1602
75. Hajizadeh-Oghaz M, Razavi RS, Ghasemi A (2015) The effect of solution pH value on the morphology of ceria–yttria co stabilized zirconia particles prepared using the polymerizable complex method. J Cluster Sci, 1–15
76. Hajizadeh-Oghaz M, Razavi RS, Ghasemi A (2015) Synthesis and characterization of ceria–yttria co-stabilized zirconia (CYSZ) nanoparticles by sol–gel process for thermal barrier coatings (TBCs) applications. J Sol-Gel Sci Technol 74(3):603–612
77. Mazaki H, Yasuoka H, Kakihana M, Fujimori H, Yashima M, Yoshimura M (1995) Complex susceptibilities of co-substituted $YBa_2Cu_3O_7^-$ synthesized by the polymerized complex method. Physica C 246(1):37–45
78. Clarke DR (2003) Materials selection guidelines for low thermal conductivity thermal barrier coatings. Surf Coat Technol 163:67–74
79. Davar F, Loghman-Estarki MR (2014) Synthesis and optical properties of pure monoclinic zirconia nanosheets by a new precursor. Ceram Int 40(6):8427–8433
80. Clarke DR (2003) Materials selection guidelines for low thermal conductivity thermal barrier coatings. Surf Coat Technol 163:67–74
81. Ahmaniemi S, Vuoristo P, Mäntylä T, Cernuschi F, Lorenzoni L (2004) Modified thick thermal barrier coatings: thermophysical characterization. J Eur Ceram Soc 24(9): 2669–2679
82. Soyez G, Eastman JA, Thompson LJ, Bai G-R, Baldo PM, McCormick AW, DiMelfi RJ, Elmustafa AA, Tambwe MF, Stone DS (2000) Grain-size-dependent thermal conductivity of nanocrystallineyttria-stabilized zirconia films grown by metal-organic chemical vapor deposition. Appl Phys Lett 77(8):1155–1157
83. Braginsky L, Shklover V, Hofmann H, Bowen P (2004) High-temperature thermal conductivity of porous Al_2O_3 nanostructures. Physical review B 70:134201
84. Klemens PG, Gell M (1998) Thermal conductivity of thermal barrier coatings. Mater Sci Eng, A 245:143–149
85. Gitzen W (1970) Alumina as a ceramic material, (American Ceramic Society. Westerville, Ohio
86. Jamali H, Mozafarinia R, Shoja-Razavi R, Ahmadi-Pidani R (2014) Comparison of hot corrosion behaviors of plasma-sprayed nanostructured and conventional YSZ thermal barrier coatings exposure to molten vanadium pentoxide and sodium sulfate. J Eur Ceram Soc 34(2):485–492
87. Ghasemi R, Shoja-Razavi R, Mozafarinia R, Jamali H (2013) Comparison of microstructure and mechanical properties of plasma-sprayed nanostructured and conventional yttria stabilized zirconia thermal barrier coatings. Ceram Int 39(8):8805–8813
88. Pourbafrani M, Razavi RS, Bakhshi S, Loghman-Estarki M, Jamali H (2015) Effect of microstructure and phase of nanostructured YSZ thermal barrier coatings on its thermal shock behaviour. Surf Eng 31(1):64–73
89. Hajizadeh-Oghaz M, Razavi RS, Ghasemi A, Valefi Z (2016) Na_2SO_4 and V_2O_5 molten salts corrosion resistance of plasma-sprayed nanostructured ceria and yttria co-stabilized zirconia thermal barrier coatings. Ceram Int 42(4):5433–5446
90. Jones RL (1998) Scandia, yttria-stabilized zirconia for ultra-high temperature thermal barrier coatings. US patent no. 5,780,178

91. Jones RL, Reidy RF, Mess D (1996) Scandia, yttria-stabilized zirconia for thermal barrier coatings. Surf Coat Technol 82(1):70–76
92. Jones R (1989) Scandia-stabilized zirconia for resistance to molten vanadate-sulfate corrosion. Surf Coat Technol 39:89–96
93. Leoni M, Jones R, Scardi P (1998) Phase stability of scandia–yttria-stabilized zirconia TBCs. Surf Coat Technol 108:107–113
94. Jones RL, Mess D (1996) Improved tetragonal phase stability at 1400 C with scandia, yttria-stabilized zirconia. Surf Coat Technol 86:94–101
95. Jones RL, Williams C (1987) Hot corrosion of CoCrAlY by molten sulfate-vanadate deposits. Mater Sci Eng 87:353–360
96. Hajizadeh-Oghaz M (2016) PhD thesis, Synthesis and characterization of nanostructured ceria-yttria stabilized zirconia for thermal barrier coating
97. Politova T, Irvine J (2004) Investigation of scandia–yttria–zirconia system as an electrolyte material for intermediate temperature fuel cells—influence of yttria content in system $(Y_2O_3)x(Sc_2O_3)(11-x)(ZrO_2)89$. Solid State Ionics 168(1):153–165
98. Jones RL (1997) Some aspects of the hot corrosion of thermal barrier coatings. J Therm Spray Technol 6(1):77–84
99. Jang J, Dae-Joon K, Lee D (2001) Unusual calcination temperature dependent tetragonalal monoclinic transitions in rare earth-doped zirconia nanocrystals. J Mater Sci 36:5391
100. Tiwari S, Adhikary J, Singh T, Singh R (2009) Preparation and characterization of sol–gel derived yttria doped zirconia coatings on AISI 316L. Thin Solid Films 517(16):4502–4508
101. Narayanawamy B, Karaikudi R (2010) Process for the production of plasma sprayable yttria stabilized zirconia (ysz) and plasma sprayable ysz powder produced thereby, US patent no. 0048379 A1
102. Kanade K, Baeg J, Apte S, Prakash T, Kale B (2008) Synthesis and characterization of nanocrystallined zirconia by hydrothermal method. Mater Res Bull 43(3):723–729
103. Lei Z, Zhu Q, Zhang S (2006) Nanocrystallinescandia-doped zirconia (ScSZ) powders prepared by a glycine–nitrate solution combustion route. J Eur Ceram Soc 26(4):397–401
104. Singh K, Pathak L, Roy S (2007) Effect of citric acid on the synthesis of nano-crystalline yttria stabilized zirconia powders by nitrate–citrate process. Ceram Int 33(8):1463–1468
105. Yang J, Lian J, Dong Q, Guan Q, Chen J, Guo Z (2003) Synthesis of YSZ nanocrystalline particles via the nitrate–citrate combustion route using diester phosphate (PE) as dispersant. Mater Lett 57(19):2792–2797
106. Courtin E, Boy P, Rouhet C, Bianchi L, Bruneton E, Poirot N, Laberty-Robert C, Sanchez C (2012) Optimized sol-gel routes to synthesize yttria-stabilized zirconia thin films as solid electrolytes for solid oxide fuel cells. Chem Mater 24(23):4540–4548
107. Zhang Y, Li A, Yan Z, Xu G, Liao C, Yan C (2003) $(ZrO_2)_{0.85}(REO_{1.5})_{0.15}$(RE = Sc, Y) solid solutions prepared via three Pechini-type gel routes: 1—gel formation and calcination behaviors. J Solid State Chem 171(1):434–438
108. Zhang Y-W, Yan Z-G, Liao F-H, Liao C-S, Yan C-H (2004) Citrate gel synthesis and characterization of $(ZrO_2)_{0.85}(REO_{1.5})_{0.15}$(RE = Y, Sc) solid solutions. Mater Res Bull 39 (11):1763–1777
109. Zyryanov V, Uvarov N, Sadykov V, Ulihin A, Kostrovskii V, Ivanov V, Titov A, Paichadze K (2009) Mechanochemical synthesis and conducting properties of nanostructured rhombohedralscandia stabilized zirconia ceramics. J Alloy Compd 483(1):535–539
110. Fontaine O, Laberty-Robert C, Sanchez C (2012) Sol-gel route to zirconia–pt-nanoelectrode arrays 8 nm in radius: their geometrical impact in mass transport. Langmuir 28(7): 3650–3657
111. ShojaRazavi R, Loghman-Estarki MR, Farhadi-Khouzani M (2012) Synthesis and characterization of ZnO nano-structures by polymeric precursor route. Acta Physica Polonica-Ser A Gen Phys 121(1):98–101
112. Gaudon M, Laberty-Robert C, Ansart F, Stevens P (2006) Thick YSZ films prepared via a modified sol–gel route: thickness control (8–80 μm). J Eur Ceram Soc 26(15):3153–3160

113. Loghman-Estark MR, Razavi RS, Edris H (2013) Synthesis and thermal stability of nontransformable tetragonal $(ZrO_2)0.96(REO_{1.5})_{0.04}$(Re = Sc^{3+}, Y^{3+}) Nanocrystals. Defect and Diffusion Forum. Trans Tech Publ, pp 60–64
114. Jamali H, Mozafarinia R, ShojaRazavi R, Ahmadi-Pidani R, Reza Loghman-Estarki M (2012) Fabrication and evaluation of plasma-sprayed nanostructured and conventional YSZ thermal barrier coatings. Curr Nanosci 8(3):402–409
115. Loghman-Estarki MR, Edris H, Razavi RS (2013) Large scale synthesis of non-transformable tetragonal Sc_2O_3, Y_2O_3 doped ZrO_2 nanopowders via the citric acid based gel method to obtain plasma sprayed coating. Ceram Int 39(7):7817–7829
116. Loghman-Estarki MR, ShojaRazavi R, Edris H (2013) Large scale synthesis of non-transformable tetragonal Sc_2O_3, Y_2O_3 doped ZrO_2 nanopowders via the citric acid based gel method to obtain plasma sprayed coating. Ceram Int 39:7817–7829
117. Loghman-Estarki MR, Hajizadeh-Oghaz M, Edris H, Razavi RS (2013) Comparative studies on synthesis of nanocrystalline Sc_2O_3–Y_2O_3 doped zirconia (SYDZ) and YSZ solid solution via modified and classic Pechini method. Cryst Eng Commun 15:5898–5909
118. Srinivasan R, De Angelis RJ, Ice G, Davis BH (1991) Identification of tetragonal and cubic structures of zirconia using synchrotron x-radiation source. J Mater Res 6(06):1287–1292
119. Srivastava KK, Patil RN, Choudhary CB, Gokhale KVGK, Subba Rao EC (1974) Martensitic transformation in zirconia. Trans Brit Ceram Soc 73:85–91
120. Barberis P, Merle-Méjean T, Quintard P (1997) On Raman spectroscopy of zirconium oxide films, J Nucl Mater 246(2–3):232–243
121. Li M, Feng Z, Xiong G, Ying P, Xin Q, Li C (2001) Phase transformation in the surface region of zirconia detected by UV Raman spectroscopy. J Phys Chem B 105(34):8107–8111
122. Phillippi CM, Mazdyasni KS (1971) Infrared and Raman spectra of zirconia polymorphs. J Am Ceram Soc 54(5):254–258
123. Iwamoto N, Umesaki N, Endo S (1985) Characterization of plasma-sprayed zirconia coatings by X-ray diffraction and Raman spectroscopy. Thin Sol Films 127:129–138
124. Phillippi CM, Mazdiyasni KS (1971) Infrared and Raman spectra of zirconia polymorphs. J Am Ceram Soc 54:254–258
125. Costa G, Muccillo R (2010) Comparative studies on properties of scandia-stabilized zirconia synthesized by the polymeric precursor and the polyacrylamide techniques. J Alloy Compd 503(2):474–479
126. Sánchez C, Doria J, Paucar C, Hernandez M, Mósquera A, Rodríguez J, Gómez A, Baca E, Morán O (2010) Nanocystalline ZnO films prepared via polymeric precursor method (Pechini). Physica B 405(17):3679–3684
127. ShojaRazavi R, Loghman-Estarki MR, Farhadi-Khouzani M, Barekat M, Jamali H (2011) Large scale synthesis of zinc oxide nano- and submicro-structure by Pechini's method: effect of ethylene glycol/citric acid mole ratio on structural and optical properties. Curr Nanosci 7:807–812
128. Yu H-F, Huang K-C (2003) Effects of pH and citric acid contents on characteristics of ester-derived $BaFe_{12}O_{19}$ powder. J Magn Magn Mater 260(3):455–461
129. Thangaraju D, Samuel P, Babu SM (2010) Growth of two-dimensional $KGd(WO_4)_2$ nanorods by modified sol–gel Pechini method. Opt Mater 32(10):1321–1324
130. Kazemi F, Saberi A, Malek-Ahmadi S, Sohrabi S, Rezaie H, Tahriri M (2011) novel method for synthesis of metastable tetragonal zirconia nanopowders at low temperatures. Ceram Silik 55(1):26–30
131. Loghman-Estarki M, Razavi RS, Edris H, Bakhshi S, Nejati M, Jamali H (2016) Comparison of hot corrosion behavior of nanostructured ScYSZ and YSZ thermal barrier coatings in the presence of molten sulfate and vanadate salt. Ceram Int. doi:10.1016/j.ceramint.2016.01.147
132. Zhou CH, Zhang ZY, Zhang QM, Li Y (2014) Comparison of the hot corrosion of nanostructured and microstructured thermal barrier coatings. Mater Corros 65(6):613–619
133. Eastman J, Choi U, Li S, Soyez G, Thompson L, DiMelfi R IV (1984) Properties-4. Other-novel thermal properties of nanostructured materials. materials science forum, 1999. Aedermannsdorf, Trans Tech Publications, Switzerland, pp 629–634

134. Yang H-S, Bai G-R, Thompson L, Eastman J (2002) Interfacial thermal resistance in nanocrystallineyttria-stabilized zirconia. Acta Mater 50(9):2309–2317
135. Jamali H, Mozafarinia R, Razavi RS, Ahmadi-Pidani R (2012) Comparison of thermal shock resistances of plasma-sprayed nanostructured and conventional yttria stabilized zirconia thermal barrier coatings. Ceram Int 38(8):6705–6712
136. Ahmadi-Pidani R, Shoja-Razavi R, Mozafarinia R, Jamali H (2012) Evaluation of hot corrosion behavior of plasma sprayed ceria and yttria stabilized zirconia thermal barrier coatings in the presence of $Na_2SO_4 + V_2O_5$ molten salt. Ceram Int 38(8):6613–6620
137. Ahmadi-Pidani R, Shoja-Razavi R, Mozafarinia R, Jamali H (2012) Improving the thermal shock resistance of plasma sprayed CYSZ thermal barrier coatings by laser surface modification. Opt Lasers Eng 50(5):780–786
138. Narimani N, Saremi M, (2015) A study on the oxidation resistance of electrodeposited and nanostructured YSZ thermal barrier ceramic coatings. Ceram Int Part A 41(10): 13810–13816
139. Loghman-Estarki MR, Razavi RS, Edris H, Jamali H (2014) Life time of new SYSZ thermal barrier coatings produced by plasma spraying method under thermal shock test and high temperature treatment. Ceram Int 40(1):1405–1414t
140. Bernard B, Bianchi L, Malié A, Joulia A, Rémy B (2016) Columnar suspension plasma sprayed coating microstructural control for thermal barrier coating application. J Eur Ceram Soc 36(4):1081–1089
141. Ahmadi-Pidani R, Shoja-Razavi R, Mozafarinia R, Jamali H (2013) Laser surface modification of plasma sprayed CYSZ thermal barrier coatings. Ceram Int 39(3):2473–2480
142. Ahmadi-Pidani R, Shoja-Razavi R, Mozafarinia R, Jamali H (2014) Improving the hot corrosion resistance of plasma sprayed ceria–yttria stabilized zirconia thermal barrier coatings by laser surface treatment. Mater Des 57:336–341
143. Ghasemi R, Shoja-Razavi R, Mozafarinia R, Jamali H (2013) Laser glazing of plasma-sprayed nanostructured yttria stabilized zirconia thermal barrier coatings. Ceram Int 39(8):9483–9490
144. Loghman-Estarki MR, Nejati M, Edris H, Razavi RS, Jamali H, Pakseresht AH (2015) Evaluation of hot corrosion behavior of plasma sprayed scandia and yttria co-stabilized nanostructured thermal barrier coatings in the presence of molten sulfate and vanadate salt. J Eur Ceram Soc 35(2):693–702
145. Ghasemi R, Shoja-Razavi R, Mozafarinia R, Jamali H (2014) The influence of laser treatment on thermal shock resistance of plasma-sprayed nanostructured yttria stabilized zirconia thermal barrier coatings. Ceram Int 40(1):347–355
146. Ghasemi R, ShojaRazavi R, Mozafarinia R, Jamali H, Hajizadeh-Oghaz M, Ahmadi-Pidani R (2014) The influence of laser treatment on hot corrosion behavior of plasma-sprayed nanostructured yttria stabilized zirconia thermal barrier coatings. J Eur Ceram Soc 34 (8):2013–2021
147. Jamali H, Mozafarinia R, ShojaRazavi R, AhmadiPidani R (2012) Investigation of thermal shock behavior of plasma-sprayed NiCoCrAlY/YSZ thermal barrier coatings. Adv Mater Res (Trans Tech Publ) 246–250
148. Ahmadi PR, Razavi R, Mozafarinia R, Jamali H (2012) characterization of ceria and yttria stabilized zirconia thermal barrier coatings on in 738 superalloy, Iran J Surf Sci Eng 16:33–34
149. Wu J, Wei X, Padture NP, Klemens PG, Gell M, García E, Miranzo P, Osendi MI (2002) Low-thermal-conductivity rare-earth zirconates for potential thermal-barrier-coating applications. J Am Ceram Soc 85(12):3031–3035
150. AruláDhas N (1993) Combustion synthesis and properties of fine-particle rare-earth-metal zirconates, $Ln_2Zr_2O_7$. J Mater Chem 3(12):1289–1294
151. Jinet L et al (2015) Adhesion strength and thermal shock properties of nanostructured $5La_3TiYSZ$, 8LaYSZ and 8CeYSZ coatings prepared by atmospheric plasma spraying. Ceram Int Part B 41(9):12099–12106

152. Wang X, Zhu Y, Zhang W (2010) Preparation of lanthanum zirconate nano-powders by Molten salts method. J Non-Cryst Solids 356(20):1049–1051
153. Mao Y, Guo X, Huang JY, Wang KL, Chang JP (2009) Luminescent nanocrystals with $A_2B_2O_7$ composition synthesized by a kinetically modified molten salt method. J Phys Chem C 113(4):1204–1208
154. Subramanian M, Aravamudan G, Rao GS (1983) Oxide pyrochlores—a review. Prog Solid State Chem 15(2):55–143
155. Afrasiabi A, Saremi M, Kobayashi A (2008) A comparative study on hot corrosion resistance of three types of thermal barrier coatings: YSZ, YSZ + Al_2O_3 and YSZ/Al_2O_3. Mater Sci Eng, A 478(1):264–269
156. Djurado E, Bouvier P, Lucazeau G (1952) J Am Ceram Soc 35:107
157. Garvie RC (1965) The occurrence of metastable tetragonal zirconia as a crystallite size effect. J Phys Chem 69(4):1238–1243
158. Gocmez H (2006) The interaction of organic dispersant with alumina: A molecular modelling approach. Ceram Int 32(5):521–525
159. Deb A, Chatterjee P, Gupta SS (2007) Synthesis and microstructural characterization of α-Al_2O_3–t-ZrO_2 composite powders prepared by combustion technique. Mater Sci Eng, A 459(1):124–131
160. Gocmez H, Fujimori H, Tuncer M, Gokyer Z, Duran C (2010) The preparation and characterization of Al_2O_3/ZrO_2 nanocrystalline composite by a simple gel method. Mater Sci Eng, B 173(1):80–83
161. Saremi M, Valefi Z, Abaeian N (2013) Hot corrosion, high temperature oxidation and thermal shock behavior of nanoagglomerated YSZ–Alumina composite coatings produced by plasma spray method. Surf Coat Technol 221:133–141